Highly Sensitive Photodetectors Based on Dimensionally and Compositionally Modulated Perovskites

LOI HOK LEUNG

MPhil

The Hong Kong Polytechnic University

2021

The Hong Kong Polytechnic University

Department of Applied Physics

Highly Sensitive Photodetectors Based on Dimensionally and Compositionally Modulated Perovskites

LOI Hok Leung

A thesis submitted in partial fulfilment of the requirements for the degree of Master of Philosophy

August 2020

CERTIFICATE OF ORIGINALITY

I hereby declare that this thesis is my own work and that, to the best of my knowledge and belief, it reproduces no material previously published or written, nor material that has been accepted for the award of any other degree or diploma, except where due acknowledgement has been made in the text.

_____ (Signed)

LOI Hok Leung (Name of student)

Abstract

Photodetector, which harvests light and converts it into electrical signals, is one kind of essential optoelectronic device extensively used in fields of environmental monitoring, imaging, optical communication, and biomedical sensing. Organic-inorganic halide perovskites (e.g., $MAPbI_3$) have been regarded as revolutionary candidate materials for photodetectors because of their outstanding optoelectronic property and low-temperature solution processability, which require simple manufacturing technologies and low-cost facilities to attain sizeable photoresponse. Likewise, the optimal performance of perovskite photodetectors (PPDs) has grown to a level comparable to those of main inorganic semiconductor materials (e.g., MoS_2, WSe_2, Graphene, and Si) in commercial market. Notably, various types of halide perovskite materials have recently developed based on their outstanding structural and compositional tunability.

In this thesis, the dimensional and compositional modulations on perovskite materials were reviewed briefly. Then, the working mechanisms, performance parameters and sensing applications of PPDs were systematically investigated. My works were mainly divided into two parts. The first one was a series of $(PEA)_2(MA)_{n-1}Pb_nI_{3n+1}$ perovskite thin films designed and fabricated by a convenient hot-casting method to obtain gradient n-number in the films, which can lead to the formation of vertical two- /three-dimensional (2D/3D) heterojunctions that can enhance charge separation in the films under light illumination. Based on a single gradient perovskite film, the optimal photodetector exhibited the high responsivity of 149 AW^{-1} and specific detectivity of 2×10^{12} Jones. This work opens up the possibility of

constructing a type of dimensionally graded perovskite heterojunction in high-performance optoelectronic devices.

Another work was to apply the Sn-containing perovskite alloy $MA_{0.5}FA_{0.5}(Pb_{1-x}Sn_x)I_3$ with a bandgap lower than those of both end compounds as a photoactive layer in the near-infrared (NIR) photodetectors. Here, a high-performance phototransistor based on a single layer of Sn/Pb-based perovskite alloy has been demonstrated with ultrahigh responsivity of ~ 10^6 AW^{-1} and specific detectivity of ~ 10^{14} Jones in NIR-II region. Although Sn/Pb-based perovskite alloys are successful introduced in solar cells and even in photoconductors and photodiodes, they have never been used in phototransistors until now. This work provides a promising composition control technique for future exploration of ultrasensitive broadband perovskite phototransistors.

List of Publications

H.-L. Loi, J. P. Cao, X. Y. Guo, C.-K. Liu, N. X. Wang, J. J. Song, G. Q. Tang, Y. Zhu, F. Yan, "Gradient 2D/3D Perovskite Films Prepared by Hot-Casting for Sensitive Photodetectors", Advanced Science, 2000776, 2020. doi: 10.1002/advs.202000776

C.-K. Liu, **H.-L. Loi** (Co-First Author), J. P. Cao, G. Q. Tang, F. Liu, Q. Huang, X. L. Liang, F. Yan, "High-Performance Quasi-2D Perovskite/SWCNT Phototransistors for Low-Cost and Sensitive Broadband Photodetection", Small Structures, 2020. doi: 10.1002/sstr.202000084

C. Xie, C.-K. Liu, **H.-L. Loi** (Co-First Author), F. Yan, "Perovskite-Based Phototransistors and Hybrid Photodetectors", Advanced Functional Materials, 1903907, 2019. doi: 10.1002/adfm.201903907

C.-K. Liu, Q. D. Tai, N. X. Wang, G. Q. Tang, **H.-L. Loi**, F. Yan, "Sn-Based Perovskite for Highly Sensitive Photodetectors", Advanced Science, 1900751, 2019. doi: 10.1002/advs.201900751

Acknowledgements

First of all, I would like to express my sincere appreciation to my chief supervisor, Prof. YAN Feng, who gave me an opportunity to start my M.Phil study at the Hong Kong Polytechnic University. He will always be there to provide academic resources and insightful advices. It is impossible for me to conduct experiments smoothly and complete my research paper without Prof. Yan's strong support.

Furthermore, many thanks to Prof. ZHU Ye and Dr. GUO Xuyun for their help and resource provided within the collaborative project. I am grateful to Prof. ZHAO Jiong, who encouraged me to pursue my M.Phil study and gave me many invaluable suggestions. I would also like to thank Prof. XIE Chao for his support in writing the review paper.

I would like to thank the technicians in the Department of Applied Physics and Materials Research Centre: Mr. LAM Kwan Ho for information technology supporting; Dr. CHAN Ngai Yui for laboratory training; Mr. CHAN Tsz Lam, Ms. HO Wing Man, and Dr. WONG Hon Fai for the management of laboratory safety; Dr. LIU Hardy for the use of facilities.

I would like to express my gratitude to my colleagues in my host department, who helped me to realize my works on perovskite-based photodetectors in different aspects: Mr. TANG Kai Chi, who led me to research activities in optoelectronics; Mr. LIU Chun Ki and Mr. CAO Jiupeng, who shared me the knowledge to handle instruments for the characterizations; Dr. MAK Chun Hin, Dr. WANG Naixiang, Dr. YANG Anneng, and Mr. SONG Jiajun; who shared their experiences with me on the technique of photolithography; Dr. Tang Guanqi, Dr. YOU Peng, Dr. TAI Qidong, Mr.

LI Fangjie, Ms. LI Sihua, Miss LIU Hong, and Miss WANG Tianyue, who gave me many productive inspirations; Dr. FU Ying, Dr. LIU Shenghua, Dr. LING Hai Feng, Dr. TANG Wei, Dr. HU Zhao, and Dr. ZHENG Jianzhong, who impressed me by their enthusiasm for research works.

Additionally, I wish to thank my old friends and schoolmates for their company. They include Mr. KAM Tsz Yau, Mr. LAM Pui Yiu, Miss LI Yuen Ling, Miss CHAN Wing Yee, Mr. LAM Chun Hei, Mr. WU Cho Ming, Mr. KUANG Huanhua, and Miss LI Jiawen. The friendships with them greatly brightened my study in PolyU.

Finally, I must express thank to my parents for encouraging me to choose what I desired. It was their love that always raised me up when I got tired.

Table of Contents

Abstract ..... **I**

List of Publications ..... **III**

Acknowledgements ..... **IV**

Table of Contents ..... **VI**

List of Figures ..... **VIII**

List of Tables ..... **XIII**

List of Abbreviations ..... **XIV**

Chapter 1 Introduction **1**

1.1 Background *1*

1.2 Objectives of Research *3*

1.3 Structure of Thesis *4*

Chapter 2 Review of Novel Photodetectors Based on Dimensionally and Compositionally Modulated Perovskites **6**

2.1 Introduction *6*

2.2 Overview of Dimensional and Compositional Modulations for Perovskite Materials *8*

2.2.1 Layered Ruddlesden-Popper Perovskites 9

2.2.2 Mixed Sn/Pb-based Perovskite Alloys 11

2.3 Working Mechanisms of Photodetectors *15*

2.3.1 Photoconductive Effect 16

2.3.2 Photovoltaic Effect 17

2.3.3 Photogating Effect 17

2.3.4 Photo-Thermoelectric Effect 19

2.3.5 Bolometric Effect 19

2.3.6 Plasma-Wave-assisted (Dyakonov-Shur) Terahertz Detection 20

2.4 Performance Parameters of PPDs *20*

2.5 Typical Device Configurations for Photodetectors *22*

2.5.1 Photodetectors Based on 2D/3D Perovskite-based Heterojunction 23

2.5.2 3D Perovskite-based Phototransistors 25

2.5.3 2D Perovskite-based Phototransistors 30

Chapter 3 Gradient 2D/3D Perovskite Films Prepared by Hot-Casting for Sensitive Photodetectors 34

3.1 Introduction 34

3.2 Experimental Section 36

3.2.1 Materials Synthesis 36

3.2.2 Device Fabrication 37

3.2.3 Materials Characterization 38

3.2.4 Electrical, Optoelectronic Measurements for the Devices 39

3.3 Results and Discussion 39

3.3.1 Surface Morphology 39

3.3.2 Gradient 2D/3D Perovskite Photodetectors 46

3.4 Summary 53

Chapter 4 Highly Sensitive Near-Infrared Phototransistors Based on Low Bandgap Mixed Tin-Lead Iodide Perovskites 54

4.1 Introduction 54

4.2 Experimental Section 56

4.2.1 Materials Synthesis 56

4.2.2 Device Fabrication 57

4.2.3 Materials Characterization 57

4.2.4 Electrical, Optoelectronic Measurements for the Devices 58

4.3 Results and Discussion 58

4.3.1 Surface Morphology 58

4.3.2 Mixed Sn/Pb-based Perovskite Phototransistors 62

4.4 Summary 69

Chapter 5 Conclusions and Future Prospect 70

5.1 Conclusions 70

5.2 Future Prospect 71

References 73

List of Figures

Figure 1.1 Comparison of the optimal parameters (specific detectivity (D*), photoresponsivity (R), and response time) of photodetectors fabricated by the semiconductors including conventional silicon (Si), two-dimensional (2D) materials, and perovskite. [11] 1

Figure 2.1 Schematic diagram of various perovskite materials and their reported applications. [41] 6

Figure 2.2 Schematic diagram of thin film fabrication based on perovskite martials. **(a)** Drop casting. **(b)** Spin coating. **(c)** Centrifugal casting. **(d)** Vapor-assisted solution process **(e)** Vapor deposition. **(f)** Freeze-drying recrystallization. [11] 7

Figure 2.3 Diagraphs for the number of **(a)** publications and **(b)** citations of articles with the topic "2D halide perovskite materials" in the past decade. [47] .9

Figure 2.4 (a) XRD patterns of the 2D $(PEA)_2(MA)_2Pb_3I_{10}$ and 3D $(MA)PbI_3$ films exposed to 52% relative humidity, where asterisks represent reflections from PbI_2. **(b)** Crystal structure of the 2D $(PEA)_2(MA)_2Pb_3I_{10}$ and 3D $(MA)PbI_3$, where the inset is the PEA cation and the different colors represent various kinds of atoms: Pb (turquoise), I (purple), C (gray). [49, 50] 10

Figure 2.5 Schematic diagram of potential lead-free perovskites with summarized properties. [71] 12

Figure 2.6 (a) Schematic diagram of bandgaps for $MA(Pb_{1-x}Sn_x)I_3$. Valence and conduction bands: shaded regions; molecular orbitals: thick lines. **(b)** Atomic structures of $MA(Pb_{1-x}Sn_x)I_3$ alloys, where the colors of Pb, Sn, and I are gray, red, and purple spheres, respectively. [74] 14

Figure 2.7 Typical photon detectors for PPDs. **(a)** Photoconductors, **(b)** photodiodes, and **(c)** phototransistors. [11] 15

Figure 2.8 (a) Schematic image of sequential vapor deposition method for fabricating lateral structure with BA_2PbI_4–$BA_2MAPb_2I_7$). Atom colors: Pb = yellow; I = bright sky-blue; C = black; N = navy; $CH_3NH_3^+$ = red). [100] **(b)** Band energy diagram of PEA-based perovskite photodiodes. **(c)** Absorption of $(PEA)_2MA_3Pb_4I_{13}$ thin films with/without additions of DMSO and NH_4Cl. [67] **(d)** Comparative PL spectra illuminated from the front and back sides and **(e)** bandgap energy alignment of $(BA)_2(MA)_{n-1}Pb_nI_{3n+1}$ perovskites prepared by hot-casting. [101] **(f)** Comparative PL spectra illuminated from the front and back sides and **(g)** bandgap energy alignment of the

quasi-2D/3D perovskite film prepared with BAI/MAI ratio of 3:1. [102] 24

Figure 2.9 (a) Schematic illustration of the BGTC phototransistor with a channel of hybrid perovskite $MAPbI_3$. **(b)** Transfer characteristics of BGTC $MAPbI_3$ phototransistor in the dark (black and red symbols) and under light illumination. [59] **(c)** Schematic illustration of the device arrangement of photodetector arrays with a U-shaped transparent mask under blue LED illumination (power density: 600 $mWcm^{-2}$). Red dots, devices with photocurrent; grey dots, devices without photocurrent. **(d)** UV–vis absorption and PL spectra of PbI_2 and $MAPbI_3$ microplates. [103] Illustrations of transistor structure showing the geometry of source and drain electrodes deposited in the direction of the **(e)** backbone ($I_{DS//}$) and **(f)** branch ($I_{DS\perp}$). Transfer characteristics of aligned OPC films measured in the direction of the **(g)** backbone ($I_{DS//}$) and **(h)** branch ($I_{DS\perp}$) at 78 K. [61] 26

Figure 2.10 (a) Schematic illustration of the phototransistor with a channel of $MAPbI_3$ film. **(b)** Transfer characteristics of photodetector by two annealing methods. [60] The I_{DS}–V_{DS} curves of BGTC $MAPbI_3$ phototransistors **(c)** at incident illumination and **(d)** in the dark, respectively. The inset presents the diagram of the $MAPbI_3$ phototransistor protected through SiO_2 layer. [107] 28

Figure 2.11 (a) Schematic illustration of a $(PEA)_2SnI_4$ perovskite phototransistor. **(b)** Transfer (V_{DS}=−40 V) characteristics. *R* and *P* versus V_g for the device under 3 μW cm^{-2} green light irradiation. **(c)** Two-stage modulation of I_{ds} by negative V_g: ① light-on, ② light-off, and ③ V_g = −40. [117] **(d)** Schematic illustration of a $(PEA)_2SnI_4$ transistor. Ferroelectric polarization related light response properties of the devices based on P(VDF-TrFE)/$(PEA)_2SnI_4$ hybrid structure: The I_{DS}–V_{DS} curves in **(e)** pristine, **(f)** up, and **(g)** down states, respectively. The insets present the schematics images of the devices in different polarized directions. The corresponding band diagram of the devices in **(h)** pristine, **(i)** up and **(j)** down states, respectively. All the photoresponse tests were carried out under light illumination with 470 nm wavelength. [118].....31

Figure 3.1 Schematic illustration of the crystal structure of layered perovskite materials (along [110] zone axis) with chemical formula $(PEA)_2(MA)_{n-1}Pb_nI_{3n+1}$ (*n* = 1, 2, 3, 4 and ∞). 36

Figure 3.2 Schematic illustration of a newly enhanced hot-casting method presented with facile one-step spin-coating process for vertical 2D/3D perovskite heterojunction fabrication. 37

Figure 3.3 The infrared thermal images of **a)** modified and **b)** traditional hot-casting methods with the one-step spin-coating fabrication process for 30 s, which follows all four steps as shown in Figure 3.2. 38

Figure 3.4 Characterization of the surface morphology of five samples by a newly enhanced hot-casting method, which were fabricated by varying stoichiometric ratios (predefined *n*-values = 1, 2, 3, 4 and ∞) in $(PEA)_2(MA)_{n-1}Pb_nI_{3n+1}$ precursor solution. **a)** X-ray diffraction (XRD) patterns. The inset: The corresponding optical images of the films. **b)** Absorption spectra of above samples. **c)** Photoluminescence (PL) spectra of perovskite thin films with Si/SiO_2 substrates. Comparative PL spectra of the samples fabricated by predefined *n*-values of **d)** 3 and **e)** 4. The perovskite thin films were illuminated from the front and back sides (as illustrated in the insets) under 488 nm laser. 40

Figure 3.5 The comparative PL spectra of the samples fabricated by predefined n-values of **a)** 3 and **b)** 4 through preheat temperatures of 100 °C and 150 °C (without the aluminum holder). The elevated preheat temperature of 200 °C was found to significantly influence plasma treatment and then invalidate the following thin film crystallization. The perovskite thin films were illuminated from the front and back sides under 488 nm laser. 41

Figure 3.6 Cross-sectional FIB-TEM investigations of the sample fabricated by predefined *n*-value of 3. **a)** The cross-sectional FIB-STEM image. **b)** The HRTEM image from *middle* region of the perovskite layer with the scale bar for 5 nm. The planes with lattice distances of 6.6 and 3.0 Å demonstrate the existence of 2D (blue, close to the *back* region) and 3D (yellow, close to the *front* region) perovskites, respectively. The HRTEM images from **c)** *back* and **d)** *front* regions of the perovskite layer with the scale bars for 5 nm. Two below insets show their SAED patterns, respectively. 44

Figure 3.7 The Electron Energy Loss Spectroscopy (EELS) elemental maps of Si (101.1- 109.5eV; purple), O (529.5-545.6eV; yellow), I (634.5-690.5eV; green), and C (281.7- 302.0eV; blue) atoms from cross-sectional FIB-TEM investigations. 45

Figure 3.8 a) Band energy diagram of $(PEA)_2(MA)_{n-1}Pb_nI_{3n+1}$ perovskite component with different *n* numbers. **b)** Charge transfer diagram of a photodetector based on a gradient perovskite thin film. 46

Figure 3.9 Design and performance of the devices based on varying stoichiometric ratio (predefined $n = 2, 3, 4$ and ∞) in $(PEA)_2(MA)_{n-1}Pb_nI_{3n+1}$ precursor solution. **a)** Drain-source current vs. time ($I_{DS} - t$) curves at varying light intensity. The inset: The schematic illustration of perovskite photodetectors. **b)** Responsivity vs. light intensity ($R - E_e$) curves under different incident illumination power of light with 685 nm wavelength. Drain-source voltage

(V_{DS}) is 4 V and the dotted lines in $R - E_e$ curves are fitting curves with a formula of $R \propto Ee\beta - 1$.....47

Figure 3.10 The temporal I_{DS} *vs. t* curve of *n* = 3 device in the dark and under light illumination (900 nW cm^{-2}) with 598 nm wavelength. 47

Figure 3.11 The I_{DS} *vs.* V_{DS} curves of *n* = 3 device illuminated by 598 nm light (89 μW cm^{-2}) measured under different gate voltage (V_G). Inset: device structure of the phototransistor.....49

Figure 3.12 a) The noise of the dark current of n = 3 device. The operating voltage is 4 V. **b)** Analysis of noise spectral density of this 2D/3D perovskite photodetector by the Fast Fourier Transform (FFT) from corresponding dark current noise. 50

Figure 3.13 Photoresponse properties of device based on the special stoichiometric ratio (predefined *n* = 3). Plot of **a)** drain-source current and **b)** responsivity of the device as functions of V_{DS} under different illumination power of light with 598 nm wavelength. Plot of responsivity as functions of **c)** the light intensity under different visible wavelengths and **d)** the wavelength under illumination intensity of 10^{-2} mW cm^{-2}. The dotted lines in $R - E_e$ curves are fitting curves with a formula of $R \propto Ee\beta - 1$.....51

Figure 4.1 a) Relative bandgaps of organic, inorganic, and mixed perovskite alloys. **b)** Energy band diagram and c) anti-solvent crystallization strategy of $MA_{0.5}FA_{0.5}(Pb_{0.5}Sn_{0.5})I_3$ perovskite. 58

Figure 4.2 Characterization of the surface morphology based on varying stoichiometric ratios for $MA_{0.5}FA_{0.5}(Pb_{1-x}Sn_x)I_3$ perovskites, where *x* = 0.4, 0.5, 0.6, and 0.7. **a)** XRD spectra and **b)** the diagrams extracted from previous results. 59

Figure 4.3 Characterization of the surface morphology based on varying stoichiometric ratios for $MA_{0.5}FA_{0.5}(Pb_{1-x}Sn_x)I_3$ perovskites, where *x* = 0, 0.4, 0.5, 0.6, 0.7 and 1. **a)** Normalized photoluminescence (PL) and **b)** absorption spectra.....60

Figure 4.4. X-ray photoelectron spectroscopy (XPS) depth profile of $MA_{0.5}FA_{0.5}(Pb_{0.5}Sn_{0.5})I_3$ film. **a)** Atomic percent and **b)** Pb/Sn ratio from the XPS spectra as a function of depth from the top surface of Sn/Pb-based perovskite film. **c)** Band bending positions of Sn *3d* XPS peaks measured at the initial four XPS acquisitions.....61

Figure 4.5 Design and performance of the devices based on varying stoichiometric ratios for $MA_{0.5}FA_{0.5}(Pb_{1-x}Sn_x)I_3$ perovskites, where *x* = 0.4, 0.5, and 0.6. **a)** The schematic illustration of perovskite photodetectors. **b)** Drain–source current versus time (I_{DS}–t) curves at the near-infrared wavelength

of 980 nm (16.6 μW cm^{-2}). d) Temporal photocurrent responses highlighting for decay times. 62

Figure 4.6 a) Drain–source current versus time (I_{DS}–t) curves at the near-infrared wavelength of 980 nm (16.6 μW cm^{-2}) for $MA_{0.5}FA_{0.5}(Pb_{1-x}Sn_x)I_3$ perovskites, where x = 0.7. Temporal photocurrent responses highlighting for **b)** rise and **c)** decay times for $MA_{0.5}FA_{0.5}(Pb_{1-x}Sn_x)I_3$ perovskites, where x = 0.4, 0.5, and 0.6. 63

Figure 4.7 Photoresponse properties of the perovskite phototransistors based on $MA_{0.5}FA_{0.5}(Pb_{0.5}Sn_{0.5})I_3$. **a)** Plots of drain and gate currents through the perovskite film with thickness (t_r) of ~400 nm against gate bias at drain voltage of 1 V and at the near-infrared wavelength of 980 nm (16.6 μW cm^{-2}). Plots of **b)** photocurrent and **c)** responsivity of above device as functions of drain voltage under different illumination power of light with 980 nm wavelength. 64

Figure 4.8 Plots of **a-c)** photocurrent and **d-f)** responsivity of above device as functions of drain voltage under different illumination power of light with 370, 530, and 850 nm wavelengths, respectively. 65

Figure 4.9 Plot of the responsivity as function of the light intensity with different wavelengths at V_{DG} of **a)** –80 and **b)** 0 V, respectively. **c)** Plot of responsivity as function of the wavelength under illumination. 66

Figure 4.10 a) The noise of the dark current of the device. The operating voltage is 1 V. **b)** Analysis of noise spectral density of this perovskite phototransistor by the Fast Fourier Transform (FFT) from corresponding dark current noise. 67

Figure 4.11 a) The device configuration of the perovskite phototransistors. The SEM images of the perovskite films with thickness of i) 250, ii) 400, and iii) 550 nm, where the scale bars are 500 nm. **b)** Plot of the responsivity as function of the light intensity under different wavelengths. The dotted lines in R-E_e curves are fitting curves with a formula of $R \propto E_e^{\beta-1}$. 68

List of Tables

Table 3.1 Detailed comparison of performance parameters for 2D perovskite -based photodetectors. 52

List of Abbreviations

Short forms	Meanings
∞	Infinity
τ_d	Decay time
$\tau_{lifetime}$	Lifetime of carriers
τ_r	Rise time
$\tau_{transit}$	Lifetime about transit time
2D	Two-dimensional
3D	Three-dimensional
Ar	Argon
BA	Butylamine
BGTC	Bottom-gate top-contact
Br	Bromine
CBM	Conduction band minimum
Cs	Cesium
CVD	Chemical vapor deposition
D*	Specific detectivity
DMF	Dimethylformamide
DMSO	Dimethyl sulfoxide
E_e	Light intensity
EELS	Electron energy loss spectroscopy
EQE	External quantum efficiency
I	Iodine
I_{DS}	Drain-source current
I_{ph}	Photocurrent
I_{SC}	Short-circuit current
ITO	Indium tin oxide
LEDs	Light emitting diodes
FA^+	$(NH_2)_2CH^+$
FFT	Fast fourier transform
FIB	Focused ion beam
G	Gain

HBA	4-hydrazinobenzoic acid
HRTEM	High-resolution transmission electron microscopy
IPA	Isopropyl alcohol
L	Length
MA^+	$CH_3NH_3^+$
MOS	Metal-oxide-semiconductor
MS	Multistep
NIR	Near-infrared
OS	One-step
Pb	Lead
PEA^+	$C_6H_5(CH_2)_2NH_3^+$
PDs	Photodetectors
PL	Photoluminescence
PPDs	Perovskite photodetectors
P(VDF-TrFE)	Polymer poly(vinylidene fluoride-rifluoroethylene)
R	Photoresponsivity
SAED	Selected-area electron diffraction
SBR	Signal-to-background ratio
Sn	Tin
SnF_2	Tin fluorine
TEM	Transmission electron microscope
THz	Terahertz
VBM	Valence band maximum
V_{DS}	Drain-source bias
V_G	Gate voltage
V_{OC}	Open-circuit voltage
V_{PTE}	Voltage difference in photo-thermoelectric effect
W	Width
XPS	X-ray photoelectron spectroscopy
XRD	X-ray diffraction

Chapter 1 **Introduction**

1.1 Background

Since the invention of the first perovskite-based optoelectronic device by Kojima *et al.* in 2009, [1] perovskite has drawn great attention as a new category of semiconducting materials on account of remarkable optoelectronic properties. Benefiting from desirable features in the large light absorption coefficient, long carrier diffusion length, high carrier mobility, and direct bandgap, [2-10] a variety of perovskite materials with a typical formula of ABX_3 (A and B are cations, and X is anion) have been developed to be integrated into plentiful optoelectronic devices, such as solar cells, light emitting diodes (LEDs), and photodetectors(PDs), opening a new door to the next-generation optoelectronic applications.

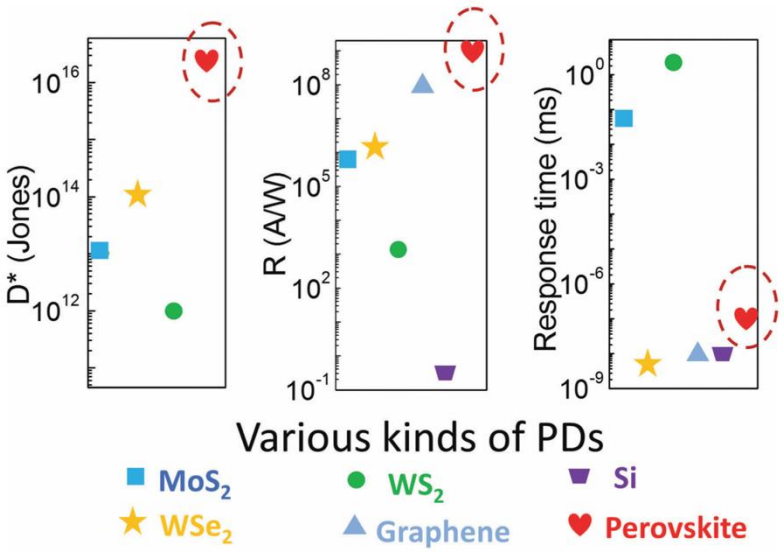

Figure 1.1 Comparison of the optimal parameters (specific detectivity (D*), photoresponsivity (R), and response time) of photodetectors fabricated by the semiconductors including conventional silicon (Si), two-dimensional (2D) materials, and perovskite. [11]

As the power conversion efficiency (PCE) of perovskite solar cells (PSCs) has skyrocketed from 3.81% [1] to 25.2% [12] within the past decade for development, perovskite photodetector (PPD) has also become a hot spot for research. Photodetector is an essential optoelectronic device that can harvest light and convert it into electrical signals. By using different structures and detection mechanics, the devices have been broadly applied in environmental monitoring, imaging, optical communication, and biomedical sensing. [13-19] Photodetections are recently dominated by the devices made from traditional inorganic semiconductors (e.g., Si, GaN and InGaAs) [20, 21] Nevertheless, their fabrication processes generally require complicated manufacture technologies and expensive facilities for a thick semiconducting layer to attain sizeable photoresponse, adding an increase in cost and precluding the possibility for use in flexible photodetector. To circumvent above drawbacks, PPD has emerged as a new class of revolutionary candidate devices in recent years due to their low-temperature solution processability and tunable optical properties, which is witnessed by the optimal performances comparable to or even better than those of the popular inorganic semiconductor materials (e.g., MoS_2, WSe_2, Si, and Graphene) as depicted in **Figure 1.1**. [11]

In recent years, various types of halide perovskite materials have been widely investigated in photoelectrical applications due to their outstanding compositional and structural tunability. A wide range of compounds can be chosen by using different A-site monovalent cations (e.g., inorganic Cs^+; organic $CH_3NH_3^+$(MA) and $CH(NH_2)_2^+$(FA)), B-site divalent metal cations (e.g., Pb^{2+}, Sn^{2+}, and Ge^{2+}), and X-site halide anions (e.g., Cl^-, Br^-, and I^-), offering preferable photodetections of UV, visible, and near-infrared (NIR) light signals. Moreover, the metal halide octahedra $[BX_6]^{4-}$ as

a basic building block of the perovskites can be connected in different dimensions. In contrast to the high-performance three-dimensional (3D) PPDs generally suffering from the poor phase stability in ambient air, two-dimensional (2D) PPDs enable the protective layers consisting of large organic spacer cations (e.g., $C_6H_5(CH_2)_2NH_3^+$(PEA)) to block moisture and oxygen from surrounding environment.

1.2 Objectives of Research

Highly sensitive PDs have broad potential applications in the world. It is important for the photodetectors to possess repeatable transduction operations over long periods, but the relatively poor stability and reliability of conventional 3D perovskite materials seriously hamper their practical utilizations. [22-25] Various 2D perovskite-based PDs have been reported in recent years, yet the sensitivity of the devices is rather low mainly due to the strong quantum confinement. [26-28] Motivated by tunable optoelectronic property of the perovskite materials, the gradient perovskite heterojunction is considered as a promising photoactive layer in the state-of-the-art devices with the enhanced charge separation.

Furthermore, near-infrared (NIR) PDs are highly desirable for a multitude of industrial and scientific applications, such as optical tomography, [29] process monitoring, [30] night vision, [31] and real-time medical diagnosis. [32-37] However, the response of typical Pb-based perovskite devices is generally below than 800 nm. When Sn-based perovskites present the low-energy absorption edge because of their small bandgaps (e.g., 1.4 eV for $FASnI_3$), Sn/Pb-based perovskite alloys with a bandgap (e.g., $MA(Pb_{0.5}Sn_{0.5})I_3$ (1.17 eV)) lower than those of both end compounds (e.g.,

$MAPbI_3$ and $MASnI_3$ (1.55 and 1.3 eV)) are potentially superior candidates for the use in NIR PDs.

Considering the low sensitivity of most quasi-2D PPDs reported in recent years, the first objective in this thesis is to apply dimensional modulation throughout an accomplished 2D/3D perovskite heterostructure for reconciling the gap between satisfactory performance in 3D perovskite devices and excellent stability in 2D perovskite materials, which realizes heterostructure-assisted charge separation in the photoactive layer of high-performance PPDs. The second objective is to employ novel Pb-Sn-alloyed composition engineering to the perovskite films for ultrasensitive broadband phototransistors, as environmentally friendly Sn-based PPDs always exhibit the relatively high responsivity but low response speed compared with typical Pb-based PPDs. Through the in-depth investigation of these novel perovskite materials, the results would encourage development in the foundational concept and even reveal further great potential for optoelectronic applications.

1.3 Structure of Thesis

The chapters of this thesis are organized as follows:

Chapter 1: Introduction. In this chapter, the background and significance of the research are introduced. Also, the structure of this thesis is presented.

Chapter 2: Review of Novel Photodetectors Based on Dimensionally and Compositionally Modulated Perovskites. In this chapter, the dimensional and compositional modulations on perovskite materials are reviewed briefly. Then, the

working mechanisms, performance parameters and sensing applications of PPDs are systematically investigated.

Chapter 3: Gradient 2D/3D Perovskite Films Prepared by Hot-Casting for Sensitive Photodetectors. In this chapter, experimental methods including fabrication and characterization of 2D/3D PPDs will been shown in detail. Then, enhancement of charge separation by the cascade band structure in the vertical heterojunctions are demonstrated and the resultant high-performance photodetectors based on this kind of hybrid films are presented.

Chapter 4: Highly Sensitive Near-Infrared Phototransistors Based on Low-Bandgap Mixed Tin-Lead Iodide Perovskites. In this chapter, the ultrasensitive near-infrared phototransistors based on Sn-containing perovskite alloy $MA_{0.5}FA_{0.5}(Pb_{1-x}Sn_x)I_3$ with a bandgap lower than those of both end compounds are reported.

Chapter 5: Conclusion and Future Prospect. In this chapter, two experimental results in this thesis are concluded and the further prospect of research for the perovskite-based devices is described.

Chapter 2 **Review of Novel Photodetectors Based on Dimensionally and Compositionally Modulated Perovskites**

2.1 Introduction

In recent years, most research reports have worked on perovskite materials mainly due to their success in solar cells with skyrocketed PCE from 3.81 [1] to 25.2 % [12] within the past decade. Besides the progress of PSCs, the external quantum efficiency (EQE) of perovskite LEDs also develops rapidly from 0.76 [38] to 11.7 % [39] within 3 years. Since the invention of the first PPD by Hu in 2014, [13] the optimal performance of PPDs has also grown to a level comparable to those of popular inorganic semiconductor materials in commercial market. For instance, owing to a synergetic effect of perovskite and graphene, the responsivity of PPDs has been dramatically enhanced from 3.49 [13] to 10^9 AW^{-1} [40].

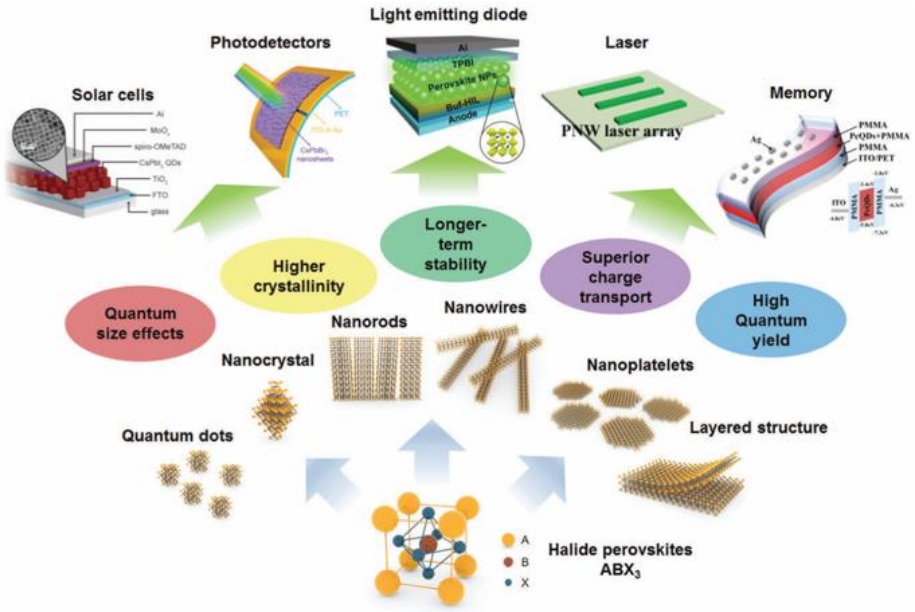

Figure 2.1 Schematic diagram of various perovskite materials and their reported applications. [41]

As a hot spot in research, perovskite has been regarded as a promising candidate material for high-performance photodetectors mainly because of its large light absorption coefficient, long carrier diffusion length, high carrier mobility, direct bandgap, and low exciton binding. [2-10] In the case of typical 3D perovskites with general formula ABX_3 (e.g., $MAPbI_3$), the Goldschmidt tolerance factor (t) and a octahedral factor (μ) generally govern their formation by the formulas of $t = \frac{R_A+R_B}{\sqrt{2}(R_B+R_X)}$ and $\mu = \frac{R_B}{R_X}$, where R_A, R_B, and R_X are the radii for the corresponding ions. It is found that the optimal of perovskite was within the range of $0.80 \leq t \leq 1.00$ and $0.44 \leq \mu \leq 0.90$ to form the preferred photo-absorber phase. After filling with a certain set of A, B, and X -site ions, A-site cations will occupy 12-fold coordinated voids in a corner-sharing network of the extended anions $[BX_6]^{4-}$ with balanced charge. [42] Notably, besides traditional 3D perovskite materials, the low-dimensional perovskite nanostructures have recent been applied in numerous photoelectronic devices as shown in **Figure 2.1**. [41]

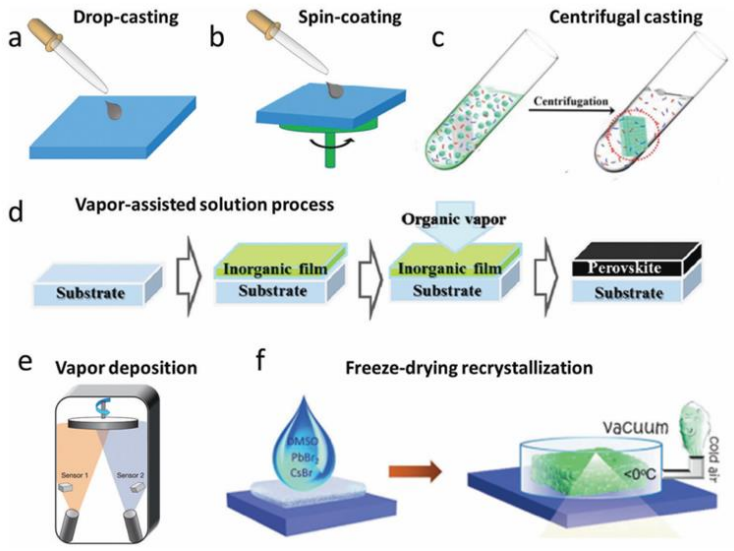

Figure 2.2 Schematic diagram of thin film fabrication based on perovskite martials. **(a)** Drop casting. **(b)** Spin coating. **(c)** Centrifugal casting. **(d)** Vapor-assisted solution process **(e)** Vapor deposition. **(f)** Freeze-drying recrystallization. [11]

The perovskite thin film, as a kind of photo-absorber layer in the photodetectors with outstanding light absorption coefficient, could adequately harvest light energy with only 300 nm thickness. [43] Notably, the photo-electric conversion generally processes in the perovskite layer for suitable light with the energy higher than their bandgaps, converting photon into electron-hole pairs. The photoexcited pairs will be separated and then collected by opposite electrodes with either external or internal electric field. In recent years, numerous studies have been conducted on high-quality perovskite thin films in order to obtain next-generation perovskite-based devices (**Figure 2.2**). [11] Owing to the facile low-temperature solution-processed fabrication techniques, an optimized polycrystalline perovskite thin film is crucial to realize low-cost, flexible and ultrasensitive PPDs.

In this chapter, I will first review the dimensional and compositional modulations on polycrystalline perovskite thin films. Then, the working mechanisms, performance parameters and sensing applications of PPDs will be discussed in detail.

2.2 Overview of Dimensional and Compositional Modulations for Perovskite Materials

Nowadays, commercial PPDs are still in the starting stage. There are the challenges for conventional 3D perovskites to realize the satisfactory stability in ambient air. Moreover, the photoresponse of typical PPDs is generally below than 800 nm. In order to obtain next-generation PPDs, the investigation of perovskite-based

dimensional and compositional modulations is timely important in photodetection applications.

2.2.1 Layered Ruddlesden-Popper Perovskites

The past several years have witnessed rapid developments of various low-dimensional halide perovskite nanostructures for obtaining fruitful progress in PPDs. Low-dimensional perovskites have attracted wide attention recently because of their unique quantum confinement effect, large surface-to-volume ratio, and anisotropic geometry and have been used as alternatives to their 3D counterparts in various optoelectronic devices. [41] By connecting or isolating the $[BX_6]^{4-}$ octahedra into different ways, the crystal growth could be adjusted to form peculiar nanostructures including zero-dimensional (0D) quantum dots, one-dimensional (1D) nanowires and 2D platelets. [44-46]

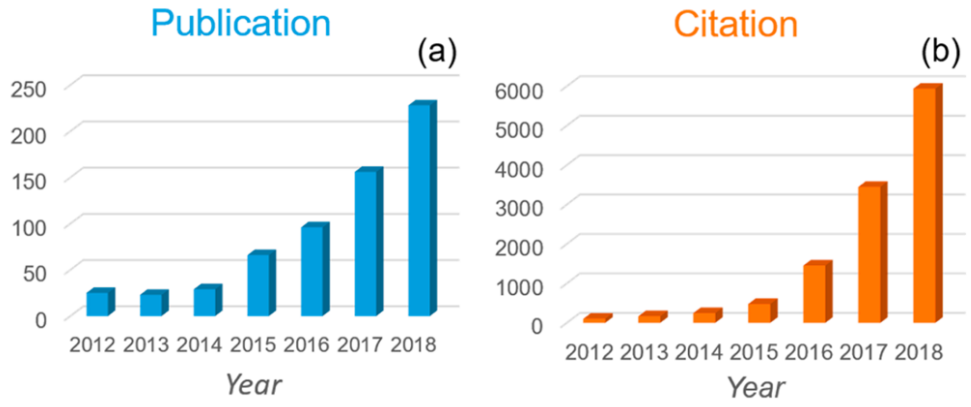

Figure 2.3 Diagraphs for the number of **(a)** publications and **(b)** citations of articles with the topic "2D halide perovskite materials" in the past decade. [47]

The number of publications and citations for 2D perovskite materials is exponentially increasing in the past decade (**Figure 2.3**). The initial preparation

methods of 2D perovskites are similar with other 2D materials (e.g., MoS_2, WSe_2, and Graphene), including mechanical exfoliation, liquid exfoliation, and chemical vapor deposition (CVD). [48] However, these manufacturing technologies are complicated, costly, and even lack of appropriate produces with large-area perovskite films. Besides these 2D perovskite nanoplates, the novel 2D layered Ruddlesden-Popper perovskite materials have been widely investigated in photoelectrical devices due to their facile structural modulation.

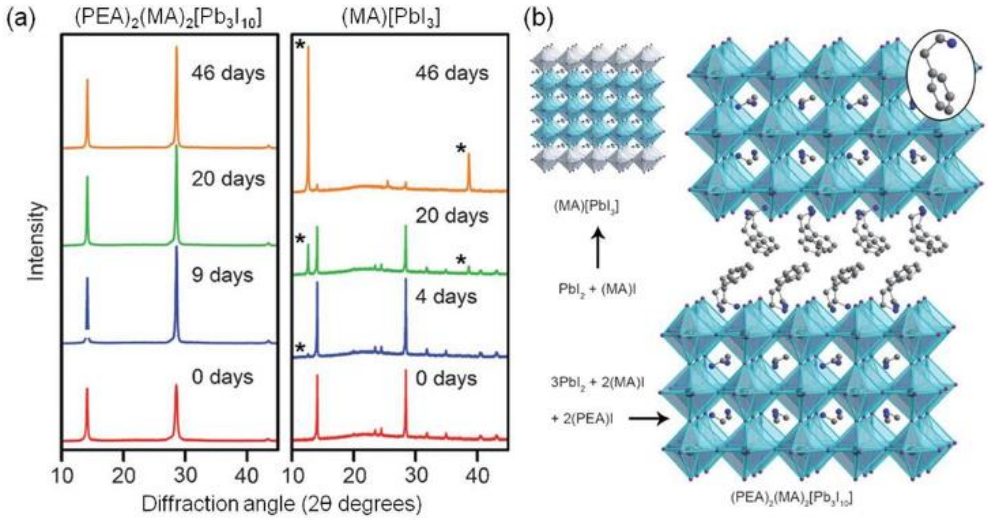

Figure 2.4 (a) XRD patterns of the 2D $(PEA)_2(MA)_2Pb_3I_{10}$ and 3D $(MA)PbI_3$ films exposed to 52% relative humidity, where asterisks represent reflections from PbI_2. **(b)** Crystal structure of the 2D $(PEA)_2(MA)_2Pb_3I_{10}$ and 3D $(MA)PbI_3$, where the inset is the PEA cation and the different colors represent various kinds of atoms: Pb (turquoise), I (purple), C (gray). [49, 50]

Ruddlesden-Popper phases have been first proposed by Ruddlesden and Popper for three compounds with K_2NiF_4- type structure in 1957. [51] In particular, 2D layered Ruddlesden-Popper perovskite materials have the general formula of $(RNH_3)_2 A_{n-1}B_nX_{3n+1}$ (n = 1, 2, 3, 4……), where RNH_3 is a large aliphatic or aromatic

alkylammonium spacer cation (e.g. PEA, phenethylamine; BA, butylamine; and iBA, n-butylamine) and n represents the number of $[BX_6]^{4-}$ octahedral layers within each quantum well. [52, 53] In contrast to conventional 3D perovskites, the large spacer cations of the 2D Ruddlesden-Popper perovskites (e.g., $(PEA)_2(MA)_{n-1}Pb_nI_{3n+1}$) enable the growth of protective layers to block moisture and oxygen from surrounding environment, as shown in **Figure 2.4**. [54-58] Smith *et al.* have employed 2D $(PEA)_2(MA)_2Pb_3I_{10}$ (n = 3) as absorbers in PSCs, which presents more resistant to moisture than that of 3D $(MA)PbI_3$. More importantly, while 3D counterparts (e.g., MAPbI3) show a fixed band with conventional ambipolar characteristics, [59-63] the 2D perovskite films consisting of alternating layers of inorganic $[BX_6]^{4-}$ sheets (well) and large organic spacers (barrier) offer possibilities for tuning their optoelectronic properties. [64-67] Shao *et al.* have further designed a phototransistor consisting of the multiphase perovskite heterostructure with high responsivity of 10^5 AW^{-1}. [68] However, such graphene/perovskite hybrid photodetectors usually suffer from high dark current because of the zero energy bandgap of graphene. [55] Moreover, both the dry transfer method of transferring exfoliated monolayer graphene on hBN and two-cycles spin-coating process of controlling BA^+ concentration in perovskite channel are comparably complicated. It is noteworthy that effective and facile methods should be further investigated for layered Ruddlesden-Popper perovskite materials.

2.2.2 Mixed Sn/Pb-based Perovskite Alloys

For hybrid lead halide perovskites, the $MAPbCl_3$ (3.1 eV) shows the larger bandgap than those of $MAPbBr_3$ (2.2 eV) and $MAPbI_3$ (1.5 eV). Besides the tunable spectral response with varying halide component, the composition modulation can further lead to the different device performances. Li *et al.* showed that the value of

photoresponsivity for the $MAPbI_{3-x}Cl_x$ ($0 \leq x \leq 3$) device (47 AW^{-1}) measured at room temperature was lower than $MAPbI_3$ device (320 AW^{-1}) due to higher dark current induced in $MAPbI_{3-x}Cl_x$ perovskite film. [59] A perovskite organic-semiconductor hybrid heterojunction photodetector was reported by Xie *et al.*, which presented a longer hole lifetime of a device based on $MAPbI_{3-x}Cl_x$/PEDOT:PSS than that of $MAPbI_3$/PEDOT:PSS. [69] As a result, the $MAPbI_{3-x}Cl_x$/PEDOT:PSS phototransistor showed a much higher responsivity of ~ 10^6 AW^{-1}. Liang *et al.* have further investigated the influence of I/Br contents in $CsPb_{0.9}Sn_{0.1}(I_{3-x}Br_x)$ perovskite films, which suggested that the phase stability of $CsPb_{0.9}Sn_{0.1}(IBr_2)$ is superior to $CsPb_{0.9}Sn_{0.1}(I_2Br)$. [70]

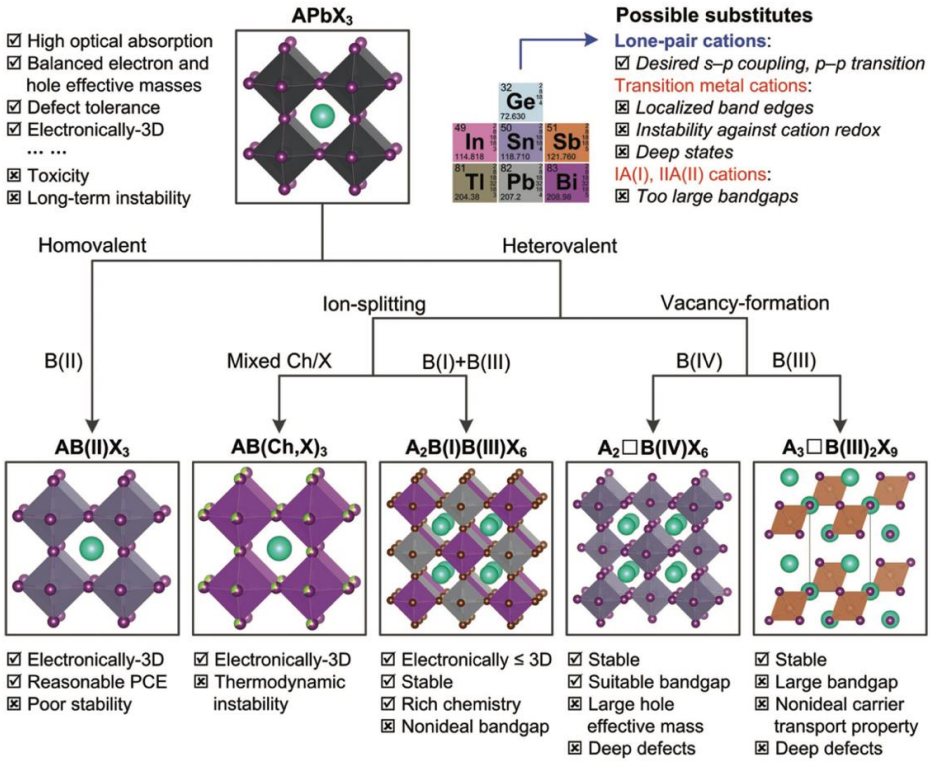

Figure 2.5 Schematic diagram of potential lead-free perovskites with summarized properties. [71]

Besides the halide content modulation, the Pb-replacement method is recently another significant research direction. As schematically depicted in **Figure 2.5**, the homovalent elements (e.g., Sn and Ge) can be applied for the Pb-replacement. [71] However, the homovalent replacement category generally causes the instability. In the case of heterovalent (e.g., Bi and Sb) replacement category, the formulae of $AB(Ch,X)_3$ and $A_2B(I)B(III)X_6$ present an ion-splitting subcategory, where Ch is the chalcogen element. Meanwhile, the formulae of $A_2{\bullet}B(III)X_9$ and $A{\bullet}B(IV)X_6$ present an ordered-vacancy subcategory, where • is the vacancy. The reduction of electronic dimensionality from both these two subcategories for heterovalent replacement generally degrades the photoelectronic properties, which causes the inferior performances of lead-free PSCs and PPDs.

Because of the same possess lone-pair s orbitals, Sn is the most promising candidate for Pb-replacement. In contrast to Pb-based perovskites, the Sn-based perovskites show the lower bandgap and higher high absorption for visible light. However, the instability of high-energy-lying Sn $5s^2$ states can easily break the Sn-I bonds into high-density Sn vacancies and thus be oxidized to quadrivalent s^2. [72] As solutions for the stability issues to prevent the formation of Sn vacancies and antioxidant, Sn^{2+}-rich precursor solutions with $SnCl_2$ or SnI_2 additives are generally used for the fabrication of Sn-based perovskites. Moreover, to solve this obstacle, an antioxidant additive of ascorbic acid was first introduced in $FA_{0.5}MA_{0.5}Sn_{0.5}Pb_{0.5}I_3$ PPDs by Jen *et al.*, which can efficaciously suppress oxidation of Sn^{2+} to Sn^{4+} states. [73]

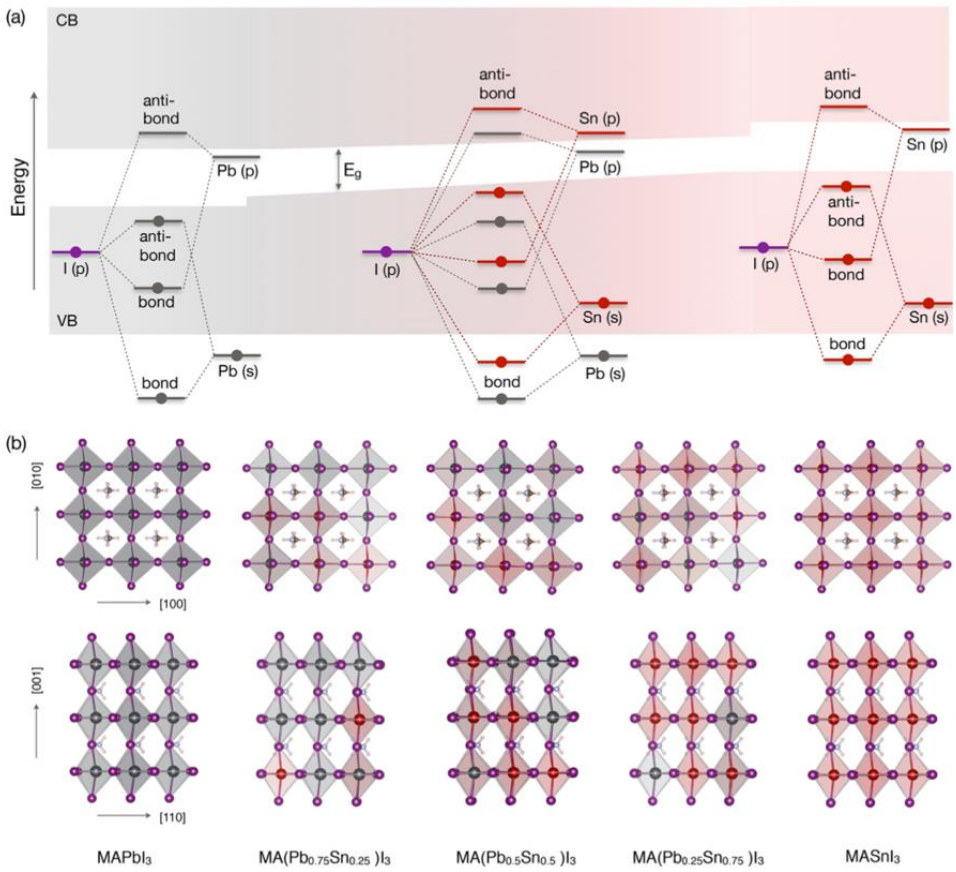

Figure 2.6 (a) Schematic diagram of bandgaps for $MA(Pb_{1-x}Sn_x)I_3$. Valence and conduction bands: shaded regions; molecular orbitals: thick lines. **(b)** Atomic structures of $MA(Pb_{1-x}Sn_x)I_3$ alloys, where the colors of Pb, Sn, and I are gray, red, and purple spheres, respectively. [74]

By assisting with proper antioxidant additives in precursor solutions, stable Sn/Pb-based perovskite alloys with a bandgap (e.g., $MA(Pb_{0.5}Sn_{0.5})I_3$ (1.17 eV)) lower than those of both end compounds could be further fabricated for NIR-PPDs. As shown in **Figure 2.6**, the valence band maximum (VBM) and the conduction band minimum (CBM) in the Sn/Pb-based perovskite alloys are formed from interactions between I-*p* and Sn-*s* orbitals and I-*p* and Pb-*p*, respectively, which could reduce their resultant bandgaps. [74] When the ratio of Sn/Pb contents is further changing, the bandgaps could be also changed with the varying lattice constants. Apart from the broadband

photodetection, environmentally friendly Sn-based PPDs always exhibit the relatively high responsivity but inferior response speed compared with typical Pb-based PPDs. By employing novel Pb-Sn-alloyed composition engineering to perovskite active layers, the high-performance broadband PPDs might be possibly achieved with fast response speed.

2.3 Working Mechanisms of Photodetectors

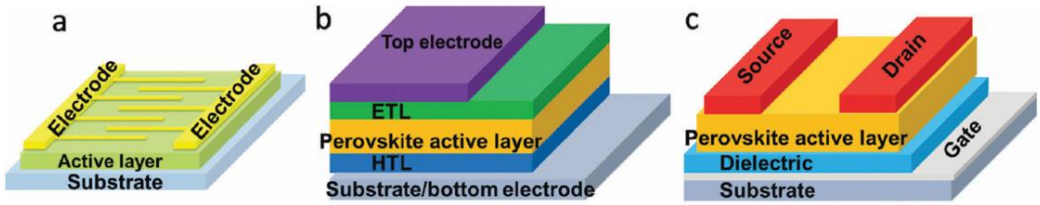

Figure 2.7 Typical photon detectors for PPDs. **(a)** Photoconductors, **(b)** photodiodes, and **(c)** phototransistors. [11]

Photodetector is one kind of essential optoelectronic devices, which can operate via several physical mechanisms, including the photoconductive effect, the photovoltaic effect, the photogating effect, the photo-thermoelectric effect, the bolometric effect, and the plasma-wave-assisted (also called Dyakonov-Shur) mechanism. Based on those sensing mechanisms, photodetectors can be simply divided into two categories: photon detectors (e.g., photoconductors, photodiodes and phototransistors, as shown in **Figure 2.7**) and thermal detectors. [11] The following section has presented these working mechanisms for photodetectors.

2.3.1 Photoconductive Effect

The photoconductive effect is a photoelectric phenomenon in which some semiconductors exhibit the increase in the electrical conductivity by the photon absorption. Semiconductor materials are often used as the channel of the photoconductors due to the ordinarily poor conductivity. In darkness, they advertise only a small drain-source current (I_{DS}) under a bias applied between the drain and source electrodes (V_{DS}). Under illumination, the semiconductors become distinctly conducting when the photons with energy larger than the bandgap are absorbed to excite electrons into the conduction band. After the additional charge carriers are separated by the V_{DS}, the free electrons and holes drift oppositely towards the drain and source electrodes that leads to a net increase of the current (photocurrent, I_{ph}).

Under a moderate V_{DS}, the majority of carriers have a much higher mobility and consequently a much shorter transit time than that of the minority of carriers. As the drift speed of the majority carriers (assumed to be electrons) is much quicker than that of the minority carriers (electrons), more electrons are supplied from the opposite electrode and circulate many times in the channel to maintain charge neutrality. The gain (G) is defined by the ratio of the lifetime of minority carriers ($\tau_{lifetime}$) to the transit time of majority carriers ($\tau_{transit}$), and it can be expressed as the following equation: [63]

$$G = \frac{\tau_{lifetime}}{\tau_{transit}} \tag{2.1}$$

It is noteworthy that there is a trade-off between gain and response speed for a reasonable overall performance. In order to obtain a high gain, the $\tau_{transit}$ should to be short, while the $\tau_{lifetime}$ should be long. However, the response time is determined by the

$\tau_{lifetime}$. As a result, the high gain generally induces the relatively long response time of the photoconductors.

2.3.2 Photovoltaic Effect

Photodetectors that function via the photovoltaic effect are also known as photodiodes. Based on the different work functions between materials, the built-in electric field could be conducted at the depleted region (also called junction region) of the photodiodes. As a result, the effective spatial separation of photogenerated electron-hole pairs is obtained, and the electrons and holes are propelling towards opposite directions and collected at opposite electrodes. [75] While an asymmetric current-voltage characteristic (rectifying behavior) is often presented at the photodiode in the dark, two modes (the photovoltaic mode and the photoconductive mode) can be operated under illumination. [76, 77] At zero bias (photovoltaic mode), the junction of the device separates electron-hole pairs by the built-in electric field and conducts a photocurrent (short-circuit current, I_{SC}) or a photovoltage (open-circuit voltage, V_{OC}). A photodiode functioning in this mode has the lowest dark current, thus leading to an enhanced detectivity that is basically suited to precision applications. Under reverse bias (photoconductive mode), as the direction of the external electric field is same as the built-in one, the improved separation efficiency of the electron-hole pairs is achieved. Meanwhile, because of the reduced carrier transit time and lowered diode capacitance, the high response speed can be achieved in this mode.

2.3.3 Photogating Effect

The photogating effect can be considered as a special case of photoconductive effect. [55] Depending on the material properties and device design, sometimes one

type of carriers (electron or hole) is intentionally immobilized in the phototransistors, while another type is free to move and contribute to photocurrent. [55, 78] A metal-oxide-semiconductor (MOS) structure is adopted for the typical architecture of phototransistors. The channel material generally simultaneously exhibit both superior mobility for carrier transport, high photoelectric conversion efficiency for efficient charge generation, suitable and direct bandgap for optical absorption. [79] Moreover, it should have a thin profile to enable full depletion of the channel by applied gate voltage (V_G), so that ultralow dark current can be realized. [21] Both gate bias and light can modulate the carrier density in the channel. As light incidents on the device channel area and is absorbed by the perovskite, electron-hole pairs are generated by photoelectric effect and will be extracted to respective electrodes by the V_{DS}. The applied V_G can effectively separate the carriers by capacitive coupling, increasing their recombination time. Sometimes, charge traps in the bulk of the channel or at the interfaces around the channel selectively trap the photogenerated carriers, realizing a photogating effect. [69, 78] Quantitatively, the photoconductive gain (G_p), which is number of carriers contributable to photocurrent per photoinduced carrier, can be expressed as [21]

$$G_P = \frac{t_r}{t_t} = \frac{tr}{L/v} \tag{2.2}$$

where t_r, t_t, L, and v are carrier recombination time, carrier transit time in transporting layer, channel length, and velocity of carrier in transporting layer, respectively. During the lifetime of the trapped carriers, the carriers in the channel can recirculate many times, which leads to a high gain. However, the trapped charges usually cause the slow response speed in the phototransistors.

2.3.4 Photo-Thermoelectric Effect

The photo-thermoelectric effect, which is also called Seebeck effect, occurs when non-uniform light-induced heating on two dissimilar conductors or semiconductors leads to a temperature gradient. A temperature difference (ΔT) can be obtained between the two substances, which are able to produce a significant photoresponse. [80] The resultant voltage difference (V_{PTE}) can be expressed as: [81, 82]

$$V_{PTE} = (S_1 - S_2)\,\Delta T \tag{2.3}$$

where S_1, S_2 are the Seebeck coefficients of the two substances. Basically, a uniform semiconductor cannot conduct the photo-thermoelectric effect due to the negligible temperature gradients.

2.3.5 Bolometric Effect

The bolometric effect relies on a differential change in the conductivity of the channel induced by uniform heating under illumination. As all the carrier mobility and density will change by light heating, the magnitude of bolometric effect can be determined by the bolometric coefficient (β), which is sensitive to the electrical conductivity (G) to the temperature (T) and expressed as:

$$\beta = \frac{\Delta G}{\Delta T} \tag{2.4}$$

Instead of generating I_{ph} at zero applied bias by V_{PTE} in photo-thermoelectric effect, this effect only modifies G of channels in high bias cases. [83, 84] In contrast to photon

detectors, the I_{ph} produced by photo-thermoelectric effect and bolometric effect is opposite to the conduction current.

2.3.6 Plasma-Wave-assisted (Dyakonov-Shur) Terahertz Detection

The plasma-wave-assisted effect in a channel of the field-effect-transistor (FET) is able to generate a d.c voltage from the optical frequency oscillation, which was first proposed by Dyakonov and Shur. [85] After rectifying high frequency signals up to terahertz (THz) applied between the gate and source, a plasma wave is launched at the source by driving longitudinal electric field in the channel. As a result, it efficiently converts the incident light into plasmonic oscillations and thus enhances the optical-frequency electric field, benefiting the responsivity, external quantum efficiency (EQE) and spectral selectivity in photodetectors. [86]

2.4 Performance Parameters of PPDs

As mentioned in the above section, there are many kinds of photodetectors available, which all present their respective advantages and disadvantages. For instance, photogating effect in phototransistors can lead to high photoresponse, but can significantly lower the operation speed due to the trapped charges. To quantitatively measure and compare the overall performance of a photodetector, a series of figure-of-merits is therefore developed and used to characterize performance, including photoresponsivity, gain, specific detectivity, and response time.

Responsivity (R): The photoresponsivity *R* of a photodetector is an indication of the sensitivity in devices against incident optical power. It is defined by the ratio of the photocurrent to the incident optical power on the active channel of the photodetectors, and can be expressed by [75]

$$R\ (AW^{-1}) = \frac{I_{Photo}}{P_{in}} = \frac{I_{Photo}}{E_e WL} \tag{2.5}$$

where I_{Photo} is the photocurrent given by $I_{Photo} = I_{Light} - I_{Dark}$. I_{Light} and I_{Dark} are the channel currents measured under light illumination and in the dark, respectively. P_{in} is the input optical power. Furthermore, E_e is the light intensity; *W* and *L* are the channel width and length of the device, respectively.

Specific detectivity (D):* The specific detectivity *D** is a key parameter to describe the sensitivity of the photodetector and given by: [75, 87-89]

$$D^* = \frac{\sqrt{AB}}{NEP} \tag{2.6}$$

$$NEP = \frac{\overline{i_n^2}^{1/2}}{R} \tag{2.7}$$

where *A* is the effective area of the photodetector, *B* is the bandwidth, *NEP* is the noise equivalent power, and $\overline{i_n^2}^{1/2}$ is the root mean square value of the noise current.

Notably, if one assumes that the dark current is mainly originated from shot noise, the specific detectivity can be expressed as: [90]

$$D^* = \frac{R}{\sqrt{2e(\frac{I_{Dark}}{A})}} \tag{2.8}$$

where *e* is elementary charge.

Gain (G): The gain *G* is a parameter that is closely related to responsivity, and is defined by the ratio of the amount of photogenerated carrier to the amount of incident photon on the active area. It can be expressed as the following equation: [63, 87]

$$G = \frac{Rhc}{e\lambda} \tag{2.9}$$

where *h* is the Planck's constant, *c* is the speed of light, and λ is the wavelength of the incident light.

Response time (τ)*:* The response time τ of a photodetector is a critical issue for its practical application. Notably, the rise (τ_r) and decay (τ_d) time of the device are usually defined as the time taken for the current increase from 10 to 90% of steady-state photocurrent and vice versa, accordingly.

2.5 Typical Device Configurations for Photodetectors

Hitherto, the high-performance commercialized photodetectors are predominantly made by semiconductors, including PbTe, GaN, HgCdTe and InGaAs. [91-94] However, the fabrication processes of those photodetectors are generally costly,

complicated and time-consuming. The outstanding photoelectronic properties such as direct band gap, large absorption coefficient, and high carrier mobility of perovskite materials, together with their successful application in solution-processed solar cells, [95-99] have led in-depth investigations into photodetectors.

2.5.1 Photodetectors Based on 2D/3D Perovskite-based Heterojunction

It is well known that heterojunction plays critical role in the performance of PPDs. In contrast to the flat band of either pure 3D or 2D perovskite, the band bending of 2D/3D perovskite-based heterojunction generally presents a unique photoelectronic properties. As band bending is achieved by varying *n*-numbers in $(RNH_3)_2 A_{n-1}B_nX_{3n+1}$ perovskite film, the heterojunction-assisted separation of photogenerated electron and hole pairs can be induced with a built-in electric field. Finally, the charge density and lifetime can be enhanced with suppressed electron-hole recombination.

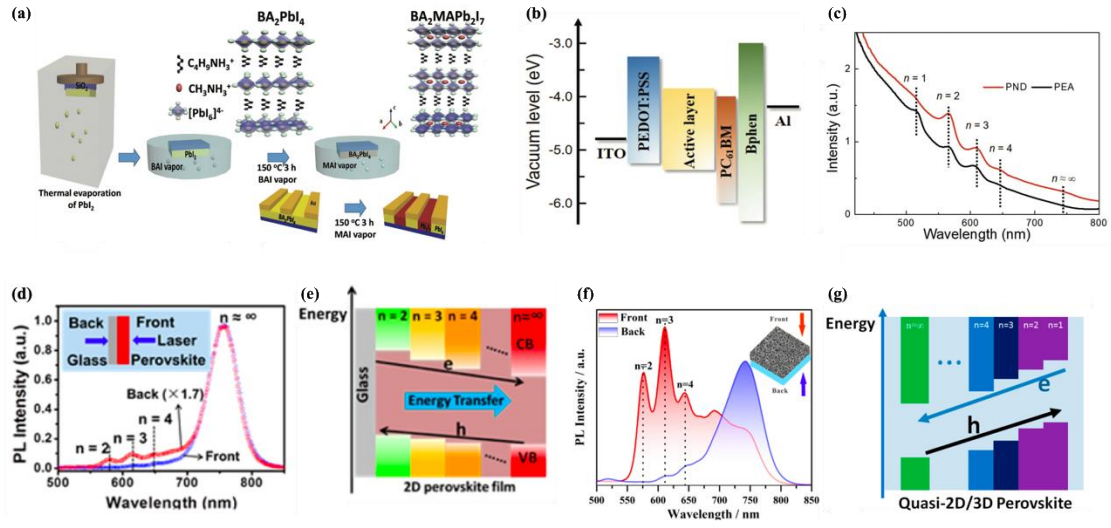

Figure 2.8 (a) Schematic image of sequential vapor deposition method for fabricating lateral structure with BA_2PbI_4–$BA_2MAPb_2I_7$). Atom colors: Pb = yellow; I = bright sky-blue; C = black; N = navy; $CH_3NH_3^+$ = red). [100] **(b)** Band energy diagram of PEA-based perovskite photodiodes. **(c)** Absorption of $(PEA)_2MA_3Pb_4I_{13}$ thin films with/without additions of DMSO and NH_4Cl. [67] **(d)** Comparative PL spectra illuminated from the front and back sides and **(e)** bandgap energy alignment of $(BA)_2(MA)_{n-1}Pb_nI_{3n+1}$ perovskites prepared by hot-casting. [101] **(f)** Comparative PL spectra illuminated from the front and back sides and **(g)** bandgap energy alignment of the quasi-2D/3D perovskite film prepared with BAI/MAI ratio of 3:1. [102]

As shown in **Figure 2.8a**, Hwang *et al.* prepared a lateral heterostructure of 2D-layered perovskites ($(BA)_2MAPb_2I_7$ - $(BA)_2PbI_4$) by vapor deposition. [100] The $(BA)_2PbI_4$ perovskite film was synthesized by depositing BAI on the PbI_2 layer. Then, patterned gold electrodes were deposited on the film by thermal evaporation in a vacuum chamber. To prepare a higher-dimensional perovskite, the sample was further exposed to MAI vapor. $(BA)_2MAPb_2I_7$ was only formed on the region for the as-fabricated $(BA)_2PbI_4$ perovskite film uncovered with gold electrodes. Resultantly, the device with a lateral heterostructure layer exhibited the responsivity of 8.12 AW^{-1}. Yan *et al.* developed the intermixed coexistence of 2D/3D perovskite phases in the active layer of the photodetector (**Figure 2.8b**). [67] The perovskite film using $NHCl_4$ additive

and dimethyl sulfoxide (DMSO) solvent (PND sample) presented the enhanced crystallinity, red-shifted photoluminescence (PL) peak, and more sensitive photoresponse due to the preferred in-plane charge transportation induced by intermixed 2D/3D phases (**Figure 2.8c**).

Liu and co-workers prepared a hierarchical quasi-2D/3D perovskite heterojunction by a facile one-step spin-coating method via a hot-casting process. [101] By illuminating on the front and back sides of the perovskite film with glass substrate, the comparison of PL spectra demonstrated three emission peaks (n = 2, 3, and 4) with back-excitation and one dominant emission peak (3D) with both excitations, suggesting that the 3D perovskites formed at the top and the quasi-2D perovskites deposited at the bottom of the active channel (**Figure 2.8d**). The sequentially distributed perovskite phases finally formed a unique built-in band alignment driving self-charge-separation as depicted in **Figure 2.8e**. Li and co-workers reported a two-step continuous deposition method dealing with the growth of BA-based quasi-2D superstructure perovskite on 3D perovskites, whereas the responsivity of 0.184 AW^{-1} was achieved. [102] **Figure 2.8f** presents the PL spectra of the hierarchical quasi-2D/3D perovskite structure consisting of multiple perovskite phases with n = 2, 3, 4 and 3D perovskite, which can be prepared by dipping isopropanol solutions with 3:1 ratio of BAI/MAI on as-fabricated PbI_2 films. As a result, the hole carriers would transfer from 3D to quasi-2D perovskites and electron carriers would transfer from quasi-2D to 3D perovskites inducted by a gradient bandgap energy alignment (**Figure 2.8g**).

2.5.2 3D Perovskite-based Phototransistors

While perovskites have aroused interests of scholars in recent years, including photoconductors and photodiodes,[59–69] $MAPbX_3$-based phototransistors have

drawn relatively less research efforts, in spite of intrinsic large charge carrier mobilities and ambipolar properties of hybrid perovskite.[41,75–77] Several investigations from different groups have even drawn similar conclusion by generally summarizing that obvious photo field-effect transistor (photo-FET) characteristics from $MAPbI_3$-based devices can only be attained at low temperature.[78–80] Though optimization of perovskite-film microstructures, modification of source–drain contact, and introduction of less-volatile inorganic cation into perovskites have been proposed and applied to eliminate negative effects,[76,81] the pure 3D $MAPbX_3$-based phototransistors attained at room temperature still require further development because of gate-field screening effect induced by the ion migration and accumulation at the perovskite/dielectric interface.[82–84]

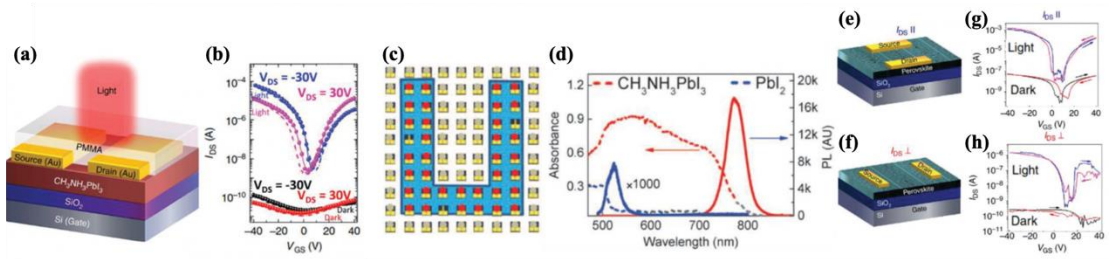

Figure 2.9 (a) Schematic illustration of the BGTC phototransistor with a channel of hybrid perovskite $MAPbI_3$. **(b)** Transfer characteristics of BGTC $MAPbI_3$ phototransistor in the dark (black and red symbols) and under light illumination. [59] **(c)** Schematic illustration of the device arrangement of photodetector arrays with a U-shaped transparent mask under blue LED illumination (power density: 600 $mWcm^{-2}$). Red dots, devices with photocurrent; grey dots, devices without photocurrent. **(d)** UV–vis absorption and PL spectra of PbI_2 and $MAPbI_3$ microplates. [103] Illustrations of transistor structure showing the geometry of source and drain electrodes deposited in the direction of the **(e)** backbone ($I_{DS//}$) and **(f)** branch ($I_{DS\perp}$). Transfer characteristics of aligned OPC films measured in the direction of the **(g)** backbone ($I_{DS//}$) and **(h)** branch ($I_{DS\perp}$) at 78 K. [61]

Li *et al.* reported fabrication and characterization of bottom-gate top-contact (BGTC) phototransistors on the basis of ambipolar solution-processed $MAPbI_3$ (**Figure 2.9a**) and $MAPbI_{3-x}Cl_x$ thin films in 2015.[59] External light source was applied as the fourth terminal electrode to further modulate channel current controlled by gate electrode, and then ambipolar $MAPbI_3$-based phototransistors were successfully obtained at room temperature as shown in the drain current versus gate voltage (I_{DS}−V_{GS}) curves (**Figure 2.9b**). The value of photoresponsivity for the $MAPbI_{3-x}Cl_x$ device (47 AW^{-1}) measured at room temperature was lower than $MAPbI_3$ device (320 AW^{-1}) due to higher dark current applied in the $MAPbI_{3-x}Cl_x$ thin film. Moreover, the response time of $MAPbI_3$ phototransistors was less than 10 μs, which demonstrated that photoresponsivity could be enhanced without sacrificing response speed by biasing gate terminal of transistor architecture.

As polycrystalline thin films made from perovskite materials are soluble in various solvents, the essential lithography process has limited most studies for integrated perovskite arrays. Fortunately, specific locations of prepatterned electrodes have offered alternative strategy for developing highly integrated systems, [104-106] and Wang *et al.* demonstrated the first patterned growth of regular arrays of $MAPbI_3$ microplate crystals (**Figure 2.9c**) with low temperature solution-processing method in 2015, including seeded growth process with PbI in hydrophilic regions and further intercalation with MAI vapor in a tube furnace system. [103] The properties of converted products were investigated in both UV–vis absorption and photoluminescence (PL) spectra as shown in **Figure 2.9d**, which demonstrated that good crystalline quality of $MAPbI_3$ microplate crystals can be attained through a gas–solid intercalation. Influences of controlling crystal orientation and morphology of

$MAPbI_3$ film on BGTC phototransistors were investigated by Cho *et al.*, [61] as solution-processed polycrystalline perovskite films always suffer from crystal defects to reduce carrier mobility in the channel by carrier capture, trapping, and scattering. By applying thermal-gradient-assisted directional crystallization method, it is illustrated that periodic microarrays could be formed spontaneously within large-area $MAPbI_3$ perovskite film parallel to the substrate ($I_{DS//}$, **Figure 2.9e**), differing from general polycrystalline $MAPbI_3$ materials. Maximum photoresponsivity at 78 K in the $I_{DS//}$ direction as 6.1 AW^{-1} was two orders of magnitude higher than that of the device measured in the $I_{DS\perp}$ (**Figure 2.9f**) direction (0.047 AW^{-1}), which was consistent with their photoinduced μ and I_{on}/I_{off} ratio (**Figure 2.9g-h**). All above results indicated that controllability of thin film directional crystal growth and preservation of high crystallinity could narrow down wide disparity in materials properties between single and polycrystalline perovskites, breaking the bottleneck of higher device performance.

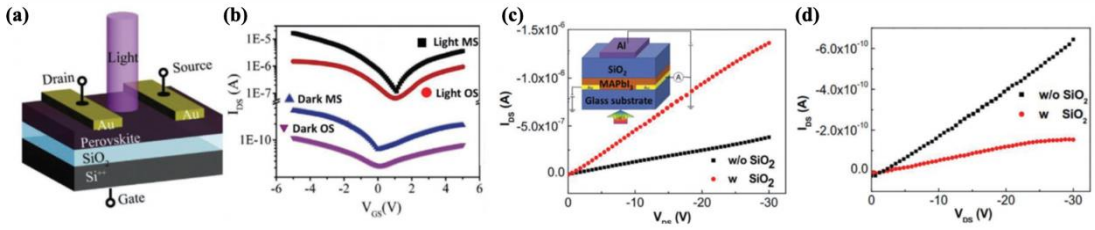

Figure 2.10 (a) Schematic illustration of the phototransistor with a channel of $MAPbI_3$ film. **(b)** Transfer characteristics of photodetector by two annealing methods. [60] The I_{DS}–V_{DS} curves of BGTC $MAPbI_3$ phototransistors **(c)** at incident illumination and **(d)** in the dark, respectively. The inset presents the diagram of the $MAPbI_3$ phototransistor protected through SiO_2 layer. [107]

The quality of fabricated polycrystalline perovskite films could be optimized by adjusting annealing temperature and duration, organic/inorganic precursor ratio, additives, and solvent. [108-113] Multistep (MS) annealing strategy in $MAPbI_3$ phototransistors was raised up by Cao *et al.*, leading to strongly improved coverage, smoothness, uniformity, and crystallinity of hybrid perovskite by restraining defects of pinhole formation. [60] When the devices were treated by one-step (OS) direct annealing method at room temperature, photoinduced μ of 0.256 (0.129) $cm^2\ V^{-1}\ s^{-1}$ for holes (electrons) of $MAPbI_3$ hybrid perovskite photo transistor (**Figure 2.10a**) were measured. Rising value of μ to 2.32 (1.18) $cm^2\ V^{-1}\ s^{-1}$, specific detectivity of 8.94×10^{11} Jones, and photoresponsivity of 32 AW^{-1} were obtained by applying MS annealing method. While the rise and decay time of MS annealed device were achieved as 42 μs and 76 μs, respectively, the relatively slow response time of OS annealed device were measured as 335 and 298 μs. Notably, both OS and MS annealed devices showed typically ambipolar behaviors in transfer characteristics (**Figure 2.10b**) with high I_{light}/I_{dark} ratio of 10^4. While inflexible Si/SiO_2 substrates as gate electrode and dielectric layer in traditional phototransistors have been investigated, [59, 61, 103] He *et al.* substituted expensive Si wafer with low-cost Al electrode as gate electrode, and then isolated active perovskite layer of the devices from moisture and oxygen by additional sol-gel SiO_2 layer. [107] This novel architecture showed that light current (I_{Light}) of all-solution-processed BGTC $MAPbI_3$ phototransistor with the sol-gel SiO_2 protecting layer was much higher than that without the protecting layer (**Figure 2.10c**). It is noticed that dark current (I_{Dark}) of the device was further reduced by adding SiO_2 layer (**Figure 2.10d**). With the rising and recovery time of 10 and 25 ms, the phototransistor with sol-gel SiO_2 protecting layer released high photoresponsivity of 10.72 AW^{-1} and

large specific detectivity of 6.2×10^{13} Jones at V_{GS} of −40 V and V_{DS} of −40 V due to the much higher photocurrent (I_{Photo}), where $I_{Photo} = I_{Light} - I_{Dark}$.

2.5.3 2D Perovskite-based Phototransistors

2D Ruddlesden-Popper $(PEA)_2SnI_4$ could be synthesized using low temperature solution-processing method, which fulfill requirements of large area, low cost, or mechanical flexibility for optoelectronic applications.[54, 57, 114] The first hybrid perovskite utilized in FET is $(PEA)_2SnI_4$ with 2D layered structure, which showed low field-effect mobility of 0.62 $cm^2V^{-1}s^{-1}$ in 1999.[54] It is most possibly because the aromatic ammonium cations in $(PEA)_2SnI_4$ could severely hinder the mobility of photo-carriers by strong quantum confinement. In spite of the substantial screening effect, [115] Mitzi *et al.* has achieved saturation and linear mobilities of 2.6 and 1.7 $cm^2V^{-1}s^{-1}$ by applying melt processed deposition technique in 2002. [116] In additional, mobility could be further optimized to 15 $cm^2V^{-1}s^{-1}$ by buffer layer modification in 2017. [117]

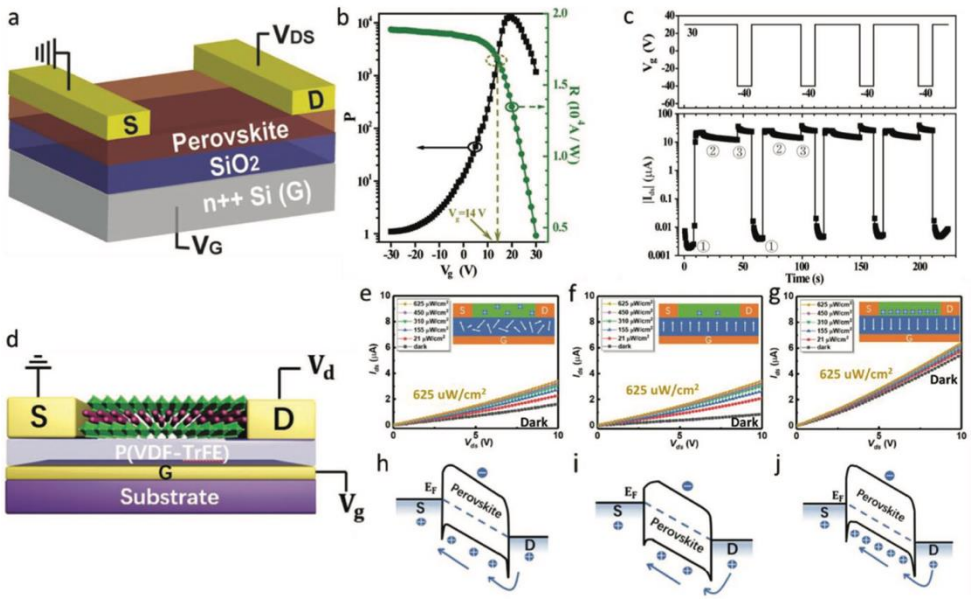

Figure 2.11 (a) Schematic illustration of a $(PEA)_2SnI_4$ perovskite phototransistor. **(b)** Transfer (V_{DS}=−40 V) characteristics. *R* and *P* versus V_g for the device under 3 μW cm^{-2} green light irradiation. **(c)** Two-stage modulation of I_{ds} by negative V_g: ① light-on, ② light-off, and ③ V_g = −40. [117] **(d)** Schematic illustration of a $(PEA)_2SnI_4$ transistor. Ferroelectric polarization related light response properties of the devices based on P(VDF-TrFE)/$(PEA)_2SnI_4$ hybrid structure: The I_{DS}–V_{DS} curves in **(e)** pristine, **(f)** up, and **(g)** down states, respectively. The insets present the schematics images of the devices in different polarized directions. The corresponding band diagram of the devices in **(h)** pristine, **(i)** up and **(j)** down states, respectively. All the photoresponse tests were carried out under light illumination with 470 nm wavelength. [118]

Chen *et al.* reported the visible light sensitive BGTC phototransistor (**Figure 2.11a**) with 2D lead-free perovskite $(PEA)_2SnI_4$ thin film fabricated by one-step spin-coating in 2017.[117] Inorganic charge-carrying sheets of 2D $(PEA)_2SnI_4$ might extend in the direction of carrier transport from electrodes under bias voltage, leading efficient charge injection under light illumination. Due to the encouraging gate modulation, ultrahigh photoresponsivity of 1.9×10^4 AW^{-1} (**Figure 2.11b)** was attained by visible light signals at V_{GS}=16 V and V_{DS}=-40 V. Saturation regime μ_h of 0.76-1.2 $cm^2V^{-1}s^{-1}$,

I_{light}/I_{dark} ratio of 100, and ultrahigh *EQE* value of 4.9×10^6 % were also achieved, showing the light-state charge transport was dominated by visible light triggered charges injection. However, due to the slow release of trapped electrons and the resulting slow recombination of holes and trapped electrons, I_{DS} could keep at high illumination state level without irradiation, indicating the relatively long relaxation time (step 2) in comparison with the rise time (step 1, 0.45 s) as shown in **Figure 2.11c**. As the metastable state could be accelerated by applying negative gate bias, [119-121] V_{GS} was switched from +30 V to −40 V (step 3) for acceleration of recombination process, and then I_{DS} could be reduced to dark state level after V_{GS} returned back into +30 V (step 4). This phenomenon has offered further potential development of fabricating ultrasensitive 2D perovskite phototransistors or light-triggered memory devices. [122]

Wang *et al.* investigated ferroelectric-effect on performance of BGBC phototransistor (**Figure 2.11d**) with same 2D layered $(PEA)_2SnI_4$ as channel layer in 2018.[118] Ferroelectric polymer poly(vinylidene fluoride-trifluoroethylene) (P(VDF-TrFE)) served as a dielectric insulator layer in the devices, forming three different polarization states including pristine, polarization "up", and polarization "down", respectively, as shown in **Figure 2.11e-g**. Compared with pristine band diagram (**Figure 2.11h**), hole carriers in phototransistors were either suppressed at "up" state (**Figure 2.11i**) or accumulated at "down" state (**Figure 2.11j**) in channel layer. Fast response speed of 50 ms and high I_{light}/I_{dark} ratio of 100 were achieved under both polarization states. It is because that molecules in ferroelectric materials were arranged conventionally after being polarized, creating a built-in potential throughout whole structure to separate electron-hole pairs. Band diagram at ferroelectric and semiconductor interface was manipulated due to different polarized directions under ferroelectric effect, [123, 124] suppressing dark current and enhancing response time.

[125] Smaller threshold swing (440.5 $mVdec^{-1}$) explicated weaker hysteresis from smoothness of transfer curve comparing SiO_2 dielectric device (6250 $mVdec^{-1}$), implying that localized traps could be strongly suppressed by P(VDF-TrFE) film with a high performance. Under "up" state during modulation of the polarization, photoresponsivity of 14.57 AW^{-1} and specific detectivity of 1.74×10^{12} Jones were further attained.

Chapter 3 **Gradient 2D/3D Perovskite Films Prepared by Hot-Casting for Sensitive Photodetectors**

In this chapter, a convenient approach for fabrication of highly sensitive and stable photodetectors through novel hot-casting technique is presented. Then, the sensitive photodetectors using vertical perovskite heterojunctions as light harvesting materials are demonstrated. After systematically characterizing the surface morphology of the perovskite channels, dramatically enhanced sensitivity of photodetection via gradient 2D/3D perovskite films has been presented. This work paves a way to realizing highly reliable and sensitive optoelectronic devices with enhanced charge separation by introducing compositional gradient in the perovskite films.

3.1 Introduction

The commercialized photodetectors are predominantly made by semiconductors, including PbTe, GaN, HgCdTe and InGaAs. [91-94] However, there are still challenges for III-V compound or Si -based photodetectors to realize the fast response, broadband sensitivity, and low-cost fabrication.[126, 127] Thus, it is necessary to product the next generation photodetectors against those problems. Recently, organic-inorganic metal halide perovskites have been regarded as promising candidate materials for high-performance photodetectors because of their unique properties and remarkable device performances. [2-10] Indeed, two-dimensional (2D) Ruddlesden-Popper perovskites have attracted wide attention because of tunable

optoelectronic properties and have been used as alternatives to their three-dimensional (3D) counterparts in various optoelectronic devices. [22-25]

Various 2D perovskite -based photodetectors have been reported while the sensitivity of the devices is rather low. [26-28] Due to the strong quantum confinement of Ruddlesden-Popper phases,[128] the undermined performances with responsivity of 0.013 A W^{-1} through $(BA)_2(MA)_{n-1}Pb_nI_{3n+1}$ (BA = butylamine) materials[129] and the relatively enhanced responsivity of 0.117 A W^{-1} through $(i\text{BA})_2(MA)_{n-1}Pb_nI_{3n+1}$ (*i*BA = n-butylamine) materials[130] were reported. Meanwhile, Li *et al.* reported the traditional two-step continuous deposition method dealing with the growth of BA-based 2D superstructure perovskite on 3D perovskites, whereas the low responsivity of 0.184 A W^{-1} was achieved.[102] Hwang and co-workers have further developed a lateral heterostructure of 2D-layered perovskites ($(BA)_2MAPb_2I_7$ - $(BA)_2PbI_4$) by vapor deposition.[100] Resultantly, the device exhibited the relatively high responsivity of 8.12 A W^{-1}.

In order to enhance the device performances of the 2D perovskite-based photodetectors, the preparation of gradient 2D/3D perovskite films have been conducted by a hot-casting method, which leads to a continuously change of the 2D perovskite compositions from n = 1 to ∞ along the vertical bottom-to-top direction of the films and forms vertical heterojunctions inside them. Photodetectors based on the gradient 2D/3D perovskite films with a simple device structure were prepared, which shows a high responsivity of 149 AW^{-1}, a gain of 270 and a specific detectivity of ~ 2 × 10^{12} Jones. A series of perovskite thin films has been fabricated with varying predefined n-values of $(PEA)_2(MA)_{n-1}Pb_nI_{3n+1}$ precursor solution. At the optimum conditions, suitable 2D/3D perovskite vertical heterojunctions are created and the

resultant photodetector exhibits the best performance, which could be attributed to the enhanced charge separation by 2D/3D perovskite vertical heterojunctions. The work opens a window on developing high-performance optoelectronic devices based on 2D/3D perovskite heterojunctions by the convenient hot-casting method.

3.2 Experimental Section

3.2.1 Materials Synthesis

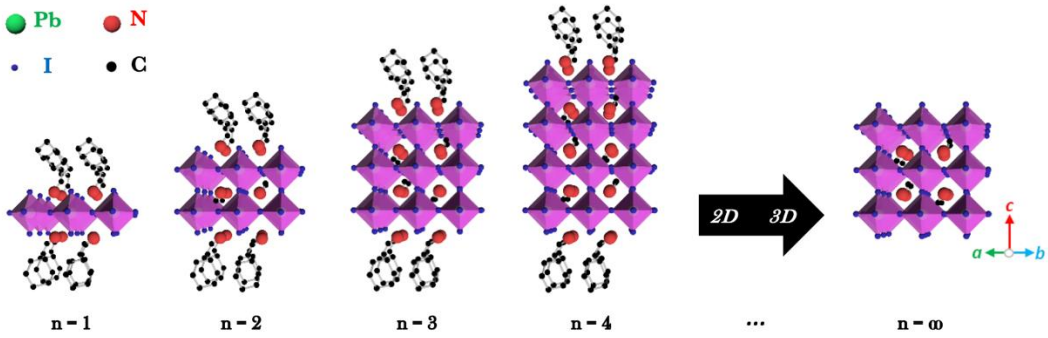

Figure 3.1 Schematic illustration of the crystal structure of layered perovskite materials (along [110] zone axis) with chemical formula $(PEA)_2(MA)_{n-1}Pb_nI_{3n+1}$ (n = 1, 2, 3, 4 and ∞).

Different $(PEA)_2(MA)_{n-1}Pb_nI_{3n+1}$ precursor solutions were prepared by dissolving phenethylammonium iodide (PEAI, Greatcell Solar Ltd), methylammonium iodide (MAI, Greatcell Solar Ltd) and lead iodide (PbI_2, Sigma-Aldrich) at a specific stoichiometric ratio of 2 : n -1 : n (n = 1, 2, 3, 4 and ∞) in a dimethyl sulfoxide (DMSO, Sigma-Aldrich)/N,N-Dimethylformamide (DMF, Alfa Aesar) (1 : 14 volume ratio) mixture, where the total Pb^{2+} molar concentration is 1.5 M. [131] The precursor solutions were then magnetically stirred at 70 ℃ in the nitrogen-filled glovebox

overnight. The crystal structures of $(PEA)_2(MA)_{n-1}Pb_nI_{3n+1}$ perovskite along [110] zone axis are shown in **Figure 3.1**, where integer n represents the number of $[PbI_6]^{4-}$ octahedral layers between organic spacer PEA^+.[45] The material with very large n-value (n = ∞) is plainly 3D tetragonal methylammonium lead iodide ($MAPbI_3$).

3.2.2 Device Fabrication

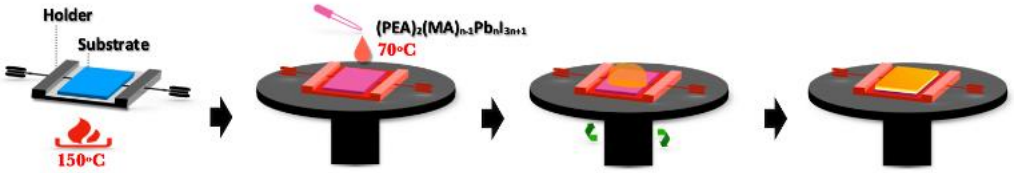

Figure 3.2 Schematic illustration of a newly enhanced hot-casting method presented with facile one-step spin-coating process for vertical 2D/3D perovskite heterojunction fabrication.

The n^+Si/SiO_2 (300 nm) and glass substrate was ultrasonically cleaned sequentially in deionized water, acetone, and isopropyl alcohol (IPA) and dried under a stream of nitrogen gas. Cr (10 nm)/Au (100 nm) electrodes with the channel width (W) and length (L) of 800 and 4 μm, respectively, were patterned via photolithography and magnetron sputtering on the n^+Si/SiO_2 substrate. The solution-based hot-casting process of gradient 2D/3D perovskite films is shown in **Figure 3.2**. Before the spin-coating, the substrate was exposed to O_2 plasma for 5 min and preheated at 150 ℃ for 9 min together with an aluminum holder. After that, 60 μL of precursor solution (70 °C preheating for 30 min before use) was dropped on to the preheated substrate followed by one-step spin-coating process at 4000 r.p.m. for 30 s.

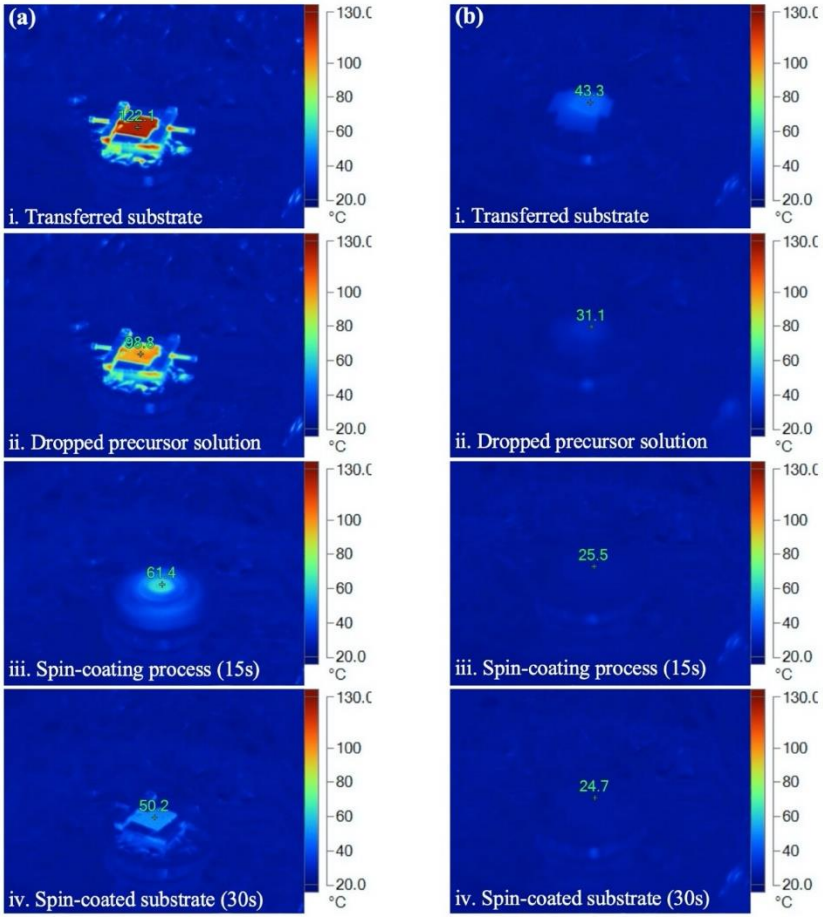

Figure 3.3 The infrared thermal images of **a)** modified and **b)** traditional hot-casting methods with the one-step spin-coating fabrication process for 30 s, which follows all four steps as shown in Figure 3.2.

As demonstrated in **Figure 3.3**, the temperature of the substrate can be maintained for a certain period of time due to the large specific heat capacity of aluminum (i.e. 0.9 kJ $kg^{-1}K^{-1}$). The gradient distribution of perovskites can be realized immediately after the hot-casting, which is more convenient than other techniques that may need additional post annealing or ligand exchange by spin-coating. [132]

3.2.3 Materials Characterization

The composition and orientation of $(PEA)_2(MA)_{n-1}Pb_nI_{3n+1}$ perovskite layer was confirmed by X-ray Diffractometer (XRD) (Rigaku SmartLab). The

Photoluminescence (PL) spectra of perovskite films were acquired by photoluminescence spectrometer (Edinburgh: FLS920) with excitation wavelength of 488 nm. The absorption spectra of perovskite films were recorded by Perkin Elmer UV-vis-NIR spectrometer. The focused ion beam (FIB) milling process and the cross-sectional FIB-TEM images were conducted using JEOL JIB-4501F and JEOL JEM-2100F TEM/STEM, respectively.

3.2.4 Electrical, Optoelectronic Measurements for the Devices

The photoresponse performance was reported using a semiconductor parameter analyzer (Keithley 4200-SCS, Solon, Ohio, USA) under light illumination at various intensity in the nitrogen-filled glovebox. The temporal response measurements were recorded by means of a digital oscilloscope (Tektronix TBS 2000) under a 4 V bias. The light sources were light-emitting diodes with wavelengths of 420, 530, 598, 685, 760 and 860 nm.

3.3 Results and Discussion

3.3.1 Surface Morphology

In order to investigate the effect of the hot-casting technique on perovskite films, the precursor solutions consisting of PEAI, MAI and PbI_2 at a specific stoichiometric ratio of 2 : n -1 : n (n = 1, 2, 3, 4 and ∞) in DMSO/DMF (1 : 14 volume ratio) mixture are prepared for following surface morphology.

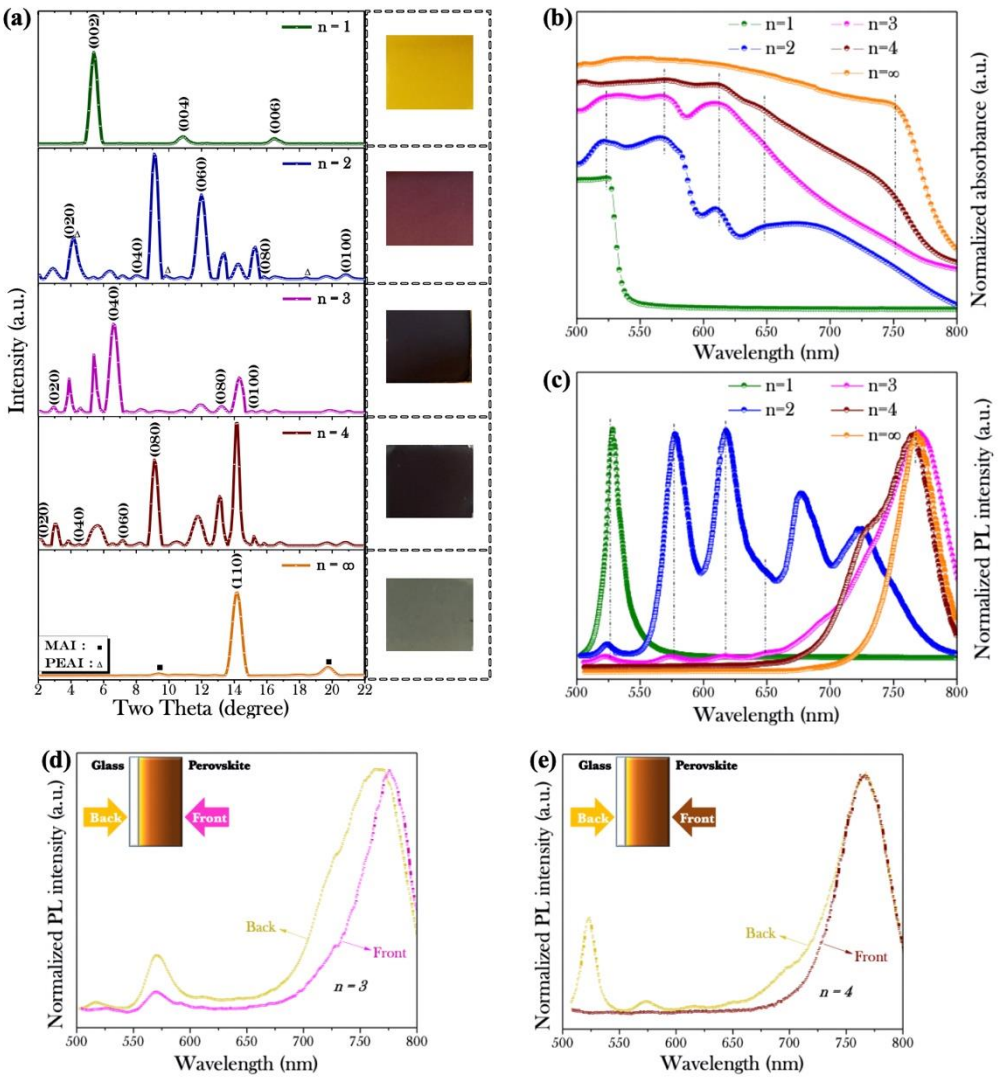

Figure 3.4 Characterization of the surface morphology of five samples by a newly enhanced hot-casting method, which were fabricated by varying stoichiometric ratios (predefined *n*-values = 1, 2, 3, 4 and ∞) in $(PEA)_2(MA)_{n-1}Pb_nI_{3n+1}$ precursor solution. **a)** X-ray diffraction (XRD) patterns. The inset: The corresponding optical images of the films. **b)** Absorption spectra of above samples. **c)** Photoluminescence (PL) spectra of perovskite thin films with Si/SiO_2 substrates. Comparative PL spectra of the samples fabricated by predefined *n*-values of **d)** 3 and **e)** 4. The perovskite thin films were illuminated from the front and back sides (as illustrated in the insets) under 488 nm laser.

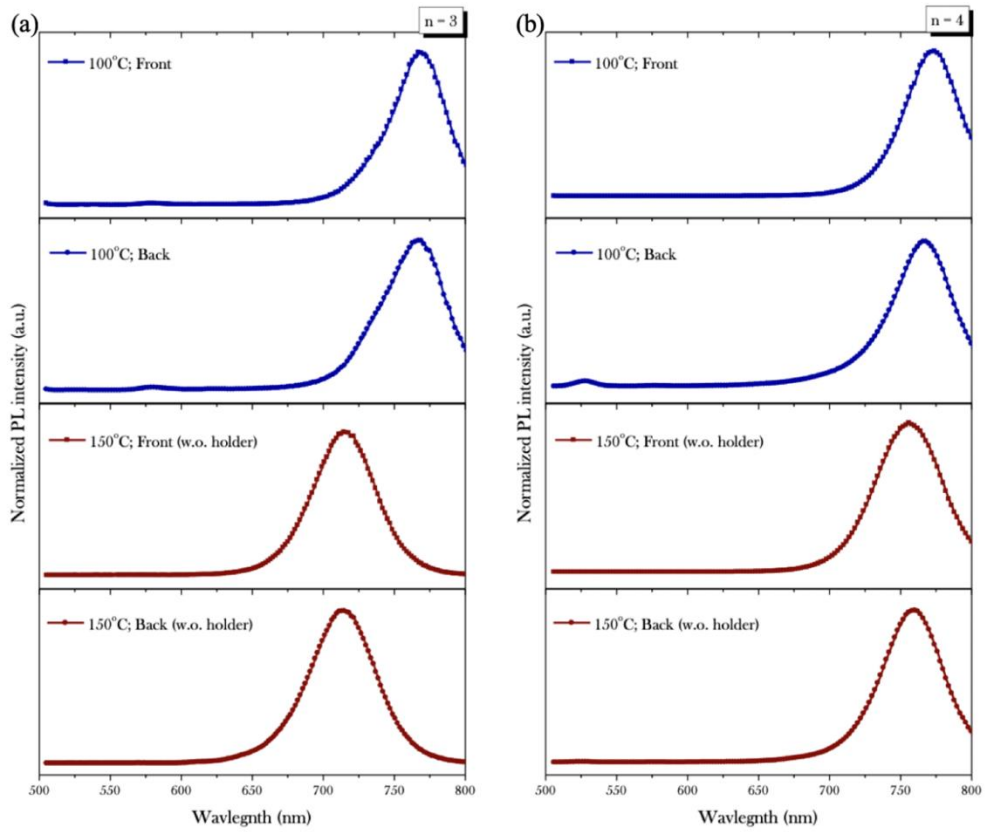

Figure 3.5 The comparative PL spectra of the samples fabricated by predefined n-values of **a)** 3 and **b)** 4 through preheat temperatures of 100 °C and 150 °C (without the aluminum holder). The elevated preheat temperature of 200 °C was found to significantly influence plasma treatment and then invalidate the following thin film crystallization. The perovskite thin films were illuminated from the front and back sides under 488 nm laser.

As-grown perovskite thin films on the glass substrates present significant change in color by different predefined n-values, as shown in the **inset of Figure 3.4a**. When *n*-value number is increased from 1 to 4, the color of $(PEA)_2(MA)_{n-1}Pb_nI_{3n+1}$ thin films changes from yellow to black. However, when n-value number is increased from 4 to ∞, the color of resulted film turned into light gray.

To evaluate the crystal structural of the perovskite films, X-ray diffraction (XRD) measurements on the samples were carried out as shown in **Figure 3.4a**. For *n*

= 1, the perovskite film only shows (002), (004) and (006) peaks of $(PEA)_2PbI_4$ perovskite phase,[133-135] indicating the $[PbI_6]^{4-}$ sheets parallel with the glass substrates.[135, 136] For $n = \infty$, the film only shows the (110) peak of the $MAPbI_3$ perovskite and two peaks for MAI. So the perovskite film has a preferred orientation along (110) direction.[137] For predefined *n*-values of 2, 3 and 4, the films present multiphase diffraction patterns of n = 1- ∞ perovskite phases, indicating rather complicated crystal structures inside them.[64] Notably, some peaks for different perovskite phases are very close and cannot be differentiated clearly. [135, 136] In addition, the diffraction peaks from both PEAI and MAI residues can be hardly observed, suggesting the high quality of the perovskite films.

The light absorption of the perovskite films are characterized and shown in **Figure 3.4b**. Similar to the XRD spectra, the absorption spectra of the perovskite films indicate that the films with predefined *n*-values of 1 and ∞ have the single phases of PEA_2PbI_4 and $MAPbI_3$ perovskites,[137, 138] respectively. For the perovskite film with predefined *n*-value of 2, four obvious absorption peaks centered at 525, 573, 610 and 675 nm corresponding to n = 1, 2, 3 and other quasi-2D perovskite phases can be observed.[137, 138] For predefined *n*-value of 3 and 4, several absorption peaks can be observed as well. Thus, these two samples have the wider absorption range of visible light compared with $MAPbI_3$ perovskite, which is consistent with their dark colors.

Figure 3.4c shows the photoluminescence (PL) spectra of the perovskite films characterized from their top surfaces. For predefined *n*-value of 2, six PL peaks located at 527, 576, 616, 650 ,678 and 724 nm for n = 1, 2, 3, 4, 5 and 6 perovskite phases, [135, 137] respectively, are obtained. When *n*-value number is increased from 2 to 4, the PL peaks from 2D perovskite phases are weakened and a relatively strong peak from 3D perovskite phase is obtained, which is consistent with the strengthened XRD peak

from (110) facet of the $MAPbI_3$ perovskite. However, by using predefined *n*-value of 4, the disappeared PL peaks from 2D perovskite phases suggest that the low-dimensional components could majorly locate at the bottom.

To further investigate the phase distribution in the films, the PL spectrum of the perovskite film with predefined *n*-value of 3 was characterized from the bottom surface through the glass substrate, as illustrated in the inset of **Figure 3.4d**. The PL peaks from n = 1, 2, 3 and other quasi-2D perovskite phases are strengthened, while the PL peak from the 3D perovskite phase shows a slightly blue shift. In comparison, a control sample for predefined *n*-values of 3 prepared by the normal thermal annealing method without the aluminum holder did not show the obvious difference in the PL spectra characterized from the top and bottom of the film (**Figure 3.5a**), indicating the phase separation is not obvious in the control sample. Similar result can be observed for predefined *n*-values of 4 (**Figure 3.4e**). In this case, several emission peaks from n = 1, 2, 3, and ∞ phases are clearly observed from the back of the film, which is completely different from the spectrum measured from the front-excitation. Meanwhile, only a single PL peak is obtained from the front- and back- excitations of the control sample for predefined *n*-values of 4 (**Figure 3.5b**). Therefore, for predefined *n*-values of 3 and 4, 2D perovskite phases accumulate at the bottom layer while 3D perovskite phase is close to the upper surface, indicating the formation of 2D/3D vertical heterojunctions in the perovskite films.

When the preheat temperature was elevated from 150 to 200 ^{o}C, the plasma treatment was significantly damaged before spin-coating process, invalidating the crystallization of PEA-based perovskite thin film. However, the eventual reproducibility of hot-casting method could be close to that of normal spin-coating method with proper preheat temperature below 150 ^{o}C. Moreover, the strong phase

separation of the 2D/3D perovskite film cannot be achieved by the conventional thermal annealing approach. Considering the solubility of PEAI in the polar organic solvent being lower than that of MAI, the fast evaporation of organic solvent can lead to the deposition of 2D perovskites earlier than 3D counterpart. Hence, the resultant 2D/3D gradient composition can be attributed to the high temperature (~150 °C) during the spin-coating process, which can quickly evaporate DMSO/DMF mixture and crystallize PEA-based 2-dimensional perovskites at the bottom surface.

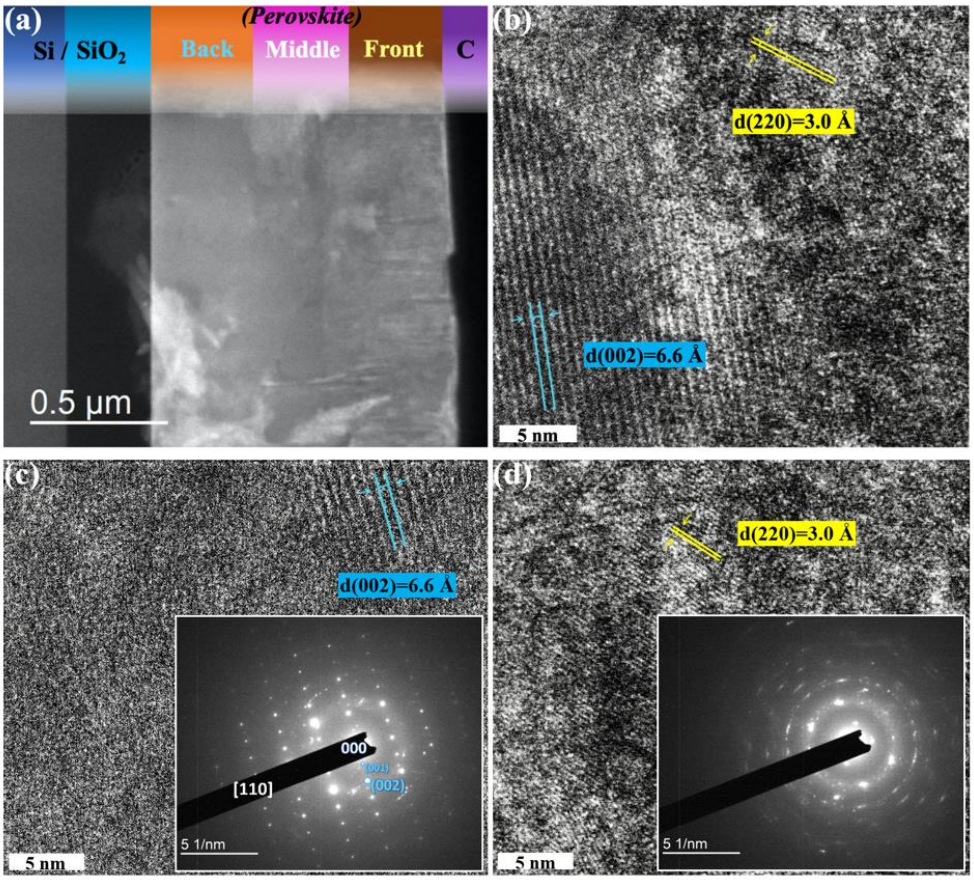

Figure 3.6 Cross-sectional FIB-TEM investigations of the sample fabricated by predefined *n*-value of 3. **a)** The cross-sectional FIB-STEM image. **b)** The HRTEM image from *middle* region of the perovskite layer with the scale bar for 5 nm. The planes with lattice distances of 6.6 and 3.0 Å demonstrate the existence of 2D (blue, close to the *back* region) and 3D (yellow, close to the *front* region) perovskites, respectively. The HRTEM images from **c)** *back* and **d)** *front* regions of the perovskite layer with the scale bars for 5 nm. Two below insets show their SAED patterns, respectively.

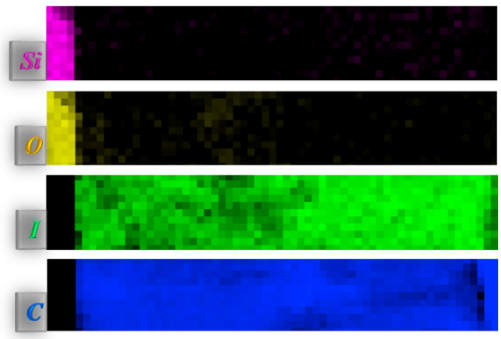

Figure 3.7 The Electron Energy Loss Spectroscopy (EELS) elemental maps of Si (101.1- 109.5eV; purple), O (529.5-545.6eV; yellow), I (634.5-690.5eV; green), and C (281.7- 302.0eV; blue) atoms from cross-sectional FIB-TEM investigations.

Next, the cross-sectional view of a perovskite film was observed under Transmission Electron Microscope (TEM), as shown in **Figure 3.6a**. It suggests that 2D and 3D perovskite phases mainly locate in the back and front regions of the film, respectively. On the basis of brightness variation, the Electron Energy Loss Spectroscopy (EELS) images (**Figure 3.7**) further demonstrate that more $[PbI_6]^{4-}$ (green for iodine) /less PEA^+ (blue for carbon) ions locate at the front layer, indicating that more 3D /less 2D perovskite component exists at the top. [138] Notably, the contrast of C map has diminished as a result of the basal carbon film on copper TEM grids. The middle region of the HRTEM image (**Figure 3.6b**) indicates the clear phase separation of 2D and 3D perovskites. The typical periodic PEA_2PbI_4 (close to the back region) and $MAPbI_3$ (close to the front region) perovskite phases with plane distances of 6.6 and 3.0 Å are observed in the left and right parts of the figure, respectively. [139] The back and front regions (Figures 3.6c and 3.6d) further present the single phase of 2D (PEA_2PbI_4) and 3D ($MAPbI_3$) perovskites**,** respectively. Their Selected-Area Electron Diffraction (SAED) patterns are also shown in the insets of the figures.[140,

141] However, 2D perovskites with $n \geq 2$ cannot be observed in the TEM image presumably due to the damage or disorder induced by inevitable local heating in the specimens with FIB milling.[142-144]

3.3.2 Gradient 2D/3D Perovskite Photodetectors

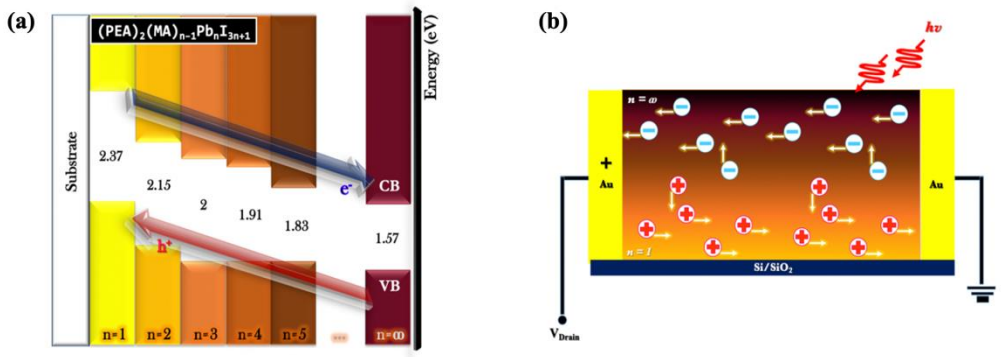

Figure 3.8 a) Band energy diagram of $(PEA)_2(MA)_{n-1}Pb_nI_{3n+1}$ perovskite component with different *n* numbers. **b)** Charge transfer diagram of a photodetector based on a gradient perovskite thin film.

The vertical 2D/3D perovskite heterostructure could lead to a cascade band structure in the film, as presented in **Figure 3.8a**. The valence band maximum (VBM) and conduction band minimum (CBM) both increase with the decrease of *n*-value,[68, 134, 136, 145, 146] which causes the charge separation with hole injection from large-*n* to small-*n* layers and the electron injection from small-*n* to large-*n*. As illustrated by the carrier transfer processes (**Figure 3.8b**) in a photodetector, holes and electrons transfer and recirculate many times in the bottom 2D and upper 3D perovskite layer, respectively, before recombining with opposite charges. Thus, long carrier lifetimes and large charge densities could be induced in the transport channel of the gradient 2D/3D perovskite film, which is favorable for the performance of photodetector.

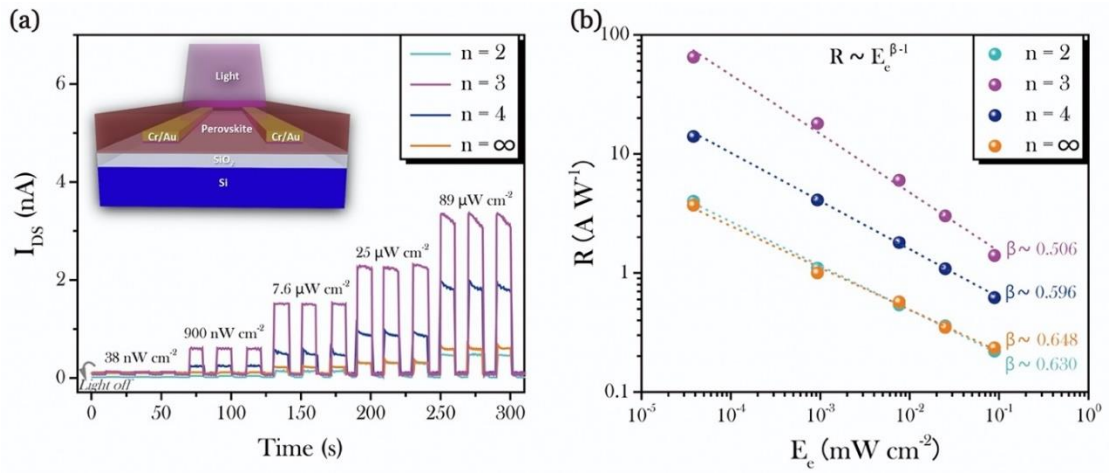

Figure 3.9 Design and performance of the devices based on varying stoichiometric ratio (predefined n = 2, 3, 4 and ∞) in $(PEA)_2(MA)_{n-1}Pb_nI_{3n+1}$ precursor solution. **a)** Drain-source current vs. time ($I_{DS} - t$) curves at varying light intensity. The inset: The schematic illustration of perovskite photodetectors. **b)** Responsivity vs. light intensity ($R - E_e$) curves under different incident illumination power of light with 685 nm wavelength. Drain-source voltage (V_{DS}) is 4 V and the dotted lines in $R - E_e$ curves are fitting curves with a formula of $R \propto E_e^{\beta-1}$.

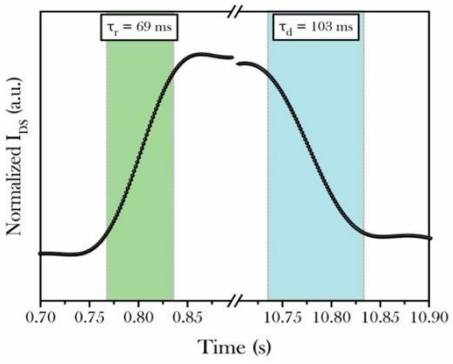

Figure 3.10 The temporal I_{DS} *vs.* t curve of n = 3 device in the dark and under light illumination (900 nW cm^{-2}) with 598 nm wavelength.

Perovskite photodetectors based on $(PEA)_2(MA)_{n-1}Pb_nI_{3n+1}$ films (**Figure 3.9a inset**) were then prepared by the hot-casting method. Cr/Au electrodes were deposited

by magnetron sputtering on a n^+Si/SiO_2 substrate and patterned by photolithography, followed by the hot-casting of a perovskite film.

The drain current vs. time (I_{DS} – t) curves between the two Au electrodes of fabricated photodetectors were measured at the drain voltage (V_{DS}) of 4 V in the dark. Then, the perovskite photodetectors were characterized under incident illumination with different intensity, as shown in **Figure 3.9a**. The device based on pure 2D PEA_2PbI_4 shows no response to the light illumination. For the devices based on perovskites with predefined *n*-values from 2 to ∞, repeatable on-off switching can be observed in three-cycle tests for each light intensity. The photocurrent increases with increasing *n*-value from 2 to 3, and then decreases with increasing *n*-value from 3 to ∞. So the 2D/3D heterojunctions formed in the perovskite layer plays an important role on the device response. The response time of a photodetector is a critical issue for its practical application. Notably, the rise (τ_r) and decay (τ_d) time of the device are usually defined as the time taken for the current increase from 10 to 90% of steady-state photocurrent and vice versa, accordingly. The rise/decay time of the device with predefined *n*=3 is determined to be 69/103 ms (**Figure 3.10**).

The responsivity (*R*) of a photodetector is given by[66]

$$R(AW^{-1}) = \frac{I_{Photo}}{E_e WL} \tag{3.1}$$

where I_{Photo} is the photocurrent given by $I_{Photo} = I_{Light} - I_{Dark}$. I_{Light} and I_{Dark} are the channel currents measured under light illumination and in the dark, respectively. Furthermore, E_e is the light intensity; *W* and *L* are the channel width and length of the device, respectively. **Figure 3.9b** shows the responsivity of all perovskite photodetectors as a function of illumination power with the maximum value of ~100 AW^{-1}. The responsivity of all the devices increases with the decrease of light intensity,

following a relationship given by $R \propto E_e^{\beta-1}$ reported before. [69, 77, 147, 148] The photocurrent and responsivity of the device with predefined *n*-value of 3 show the highest values among the devices at the same measurement condition. For the control *n* = 3 device prepared with the normal hot-casting method, the responsivity is one order of magnitude lower because of the lack of heterojunction-assisted charge separation formed in the perovskite film. Notably, the device fabricated by only spin-coating has also shown the much lower responsivity with the lack of vertical 2D/3D perovskite heterojunction.

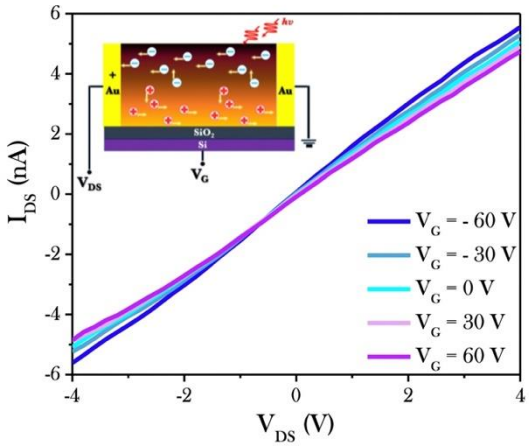

Figure 3.11 The I_{DS} *vs.* V_{DS} curves of *n* = 3 device illuminated by 598 nm light (89 μW cm^{-2}) measured under different gate voltage (V_G). Inset: device structure of the phototransistor.

The high responsivity can be attributed to the effective spatial separation of photoexcited electron-hole pairs in the vertical heterojunction as mentioned above. To directly observe the separation of electrons and holes in perovskite films, we prepared a phototransistor with predefined *n* = 3 perovskite layer on a n^+Si/SiO_2 substrate and measured the channel current under light illumination. Notably, the modulation of the channel current in a field effect transistor under a gate voltage is mainly due to the

change of carrier concentration close to the gate dielectric (i.e. SiO_2). As demonstrated in **Figure 3.11**, the channel current decreases with the increase of gate voltage (V_G), indicating that the perovskite layer close to the substrate is p channel under light illumination. Therefore, it is reasonable to conclude that holes tend to accumulate in the bottom 2D perovskite while electrons diffuse to the top 3D perovskite with spatial charge separation. While the performance of the device would be continuously damaged by applying V_{DS} of above 15 V, it has kept the stable performance under the V_{DS} range of -4 to 4 V for a long time.

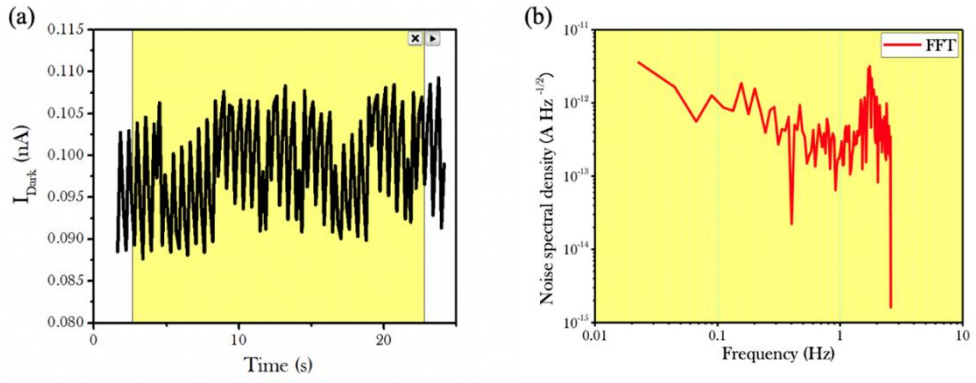

Figure 3.12 a) The noise of the dark current of n = 3 device. The operating voltage is 4 V. **b)** Analysis of noise spectral density of this 2D/3D perovskite photodetector by the Fast Fourier Transform (FFT) from corresponding dark current noise.

In addition, the specific detectivity (D^*) is the key parameter of a photodetector and given by [75, 87-89]

$$D^* = \frac{(AB)^{1/2}}{NEP} \tag{3.2}$$

$$NEP = \frac{\bar{i_n^2}^{1/2}}{R} \tag{3.3}$$

where *A* is the effective area of the photodetector, *B* is the bandwidth, *NEP* is the noise equivalent power, $\overline{i_m^2}^{1/2}$ is the root mean square value of the noise current and *R* is the responsivity of the device. The noise level per unit bandwidth (1 Hz) of the best performance device (predefined n = 3), which exhibited both the largest I_{Photo} and *R* among all the devices, was measured to be ~ 0.2 pA $Hz^{-1/2}$ (**Figure 3.12**). Therefore, *D** of the device at the wavelengths of 598 nm is calculated to be above 2×10^{12} Jones (cm $Hz^{1/2}$ W^{-1}).

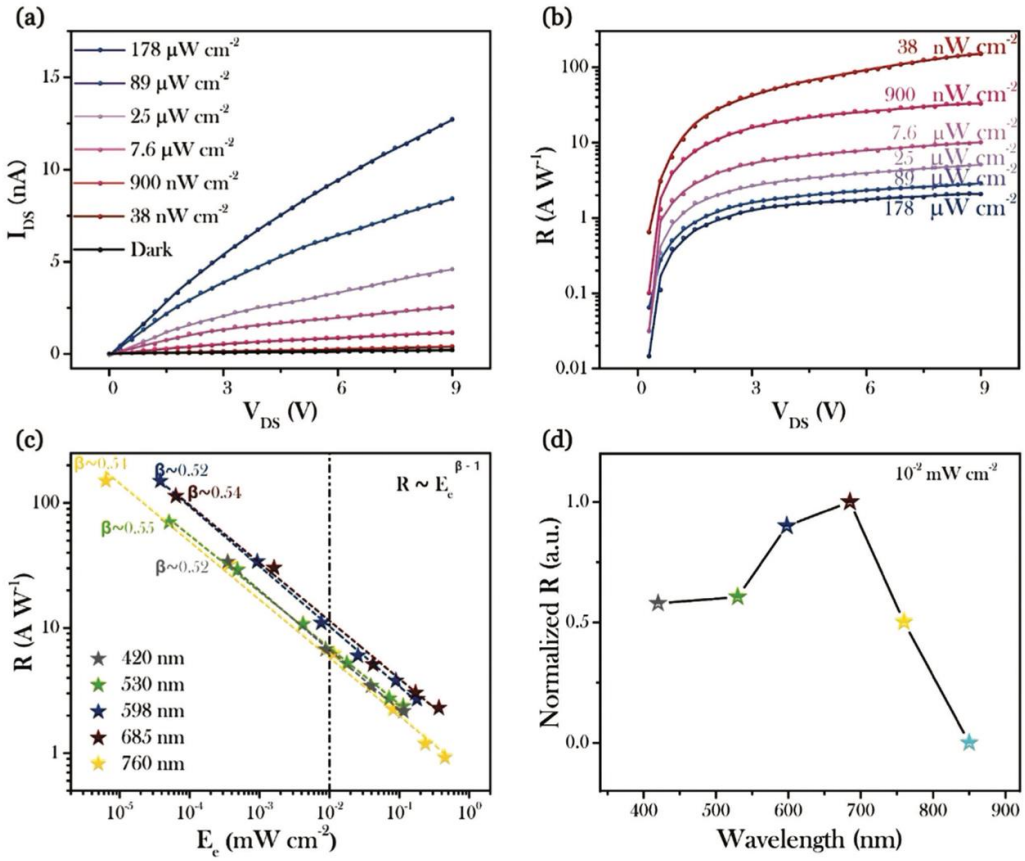

Figure 3.13 Photoresponse properties of device based on the special stoichiometric ratio (predefined n = 3). Plot of **a)** drain-source current and **b)** responsivity of the device as functions of V_{DS} under different illumination power of light with 598 nm wavelength. Plot of responsivity as functions of **c)** the light intensity under different visible wavelengths and **d)** the wavelength under illumination intensity of 10^{-2} mW cm^{-2}. The dotted lines in $R - E_e$ curves are fitting curves with a formula of $R \propto E_e^{\beta-1}$.

Table 3.1 Detailed comparison of performance parameters for 2D perovskite -based photodetectors.

Active Layer	Configurations	R [A/W]	D^* [Jones]	τ_r/τ_d [ms]	On-off Ratio	Wavelength [nm]	Voltage [V]	Ref.
$(BA)_2MA_{n-1}Pb_nI_{3n+1}$/$MAPbI_3$	Vertical	0.184	8×10^{10}	–	1×10^2	White light	–	[102]
$(PEA)_2MA_3Pb_4I_{13}$	Vertical	0.46	6×10^{11}	5.8/4.6	2×10^4	600	–	[67]
$(BA)_2MA_2Pb_3I_{10}$	Lateral	0.013	–	10/7.5	1×10^3	White light	30	[129]
$(iBA)_2MA_3Pb_4I_{13}$	Lateral	0.117	–	16/15	4×10^2	532	1.5	[130]
$(BA)_2MA_{n-1}Pb_nBr_{3n+1}$	Lateral	0.19	–	210/240	2×10^3	500	1	[66]
$(BA)_2MAPb_2I_7$ /$(BA)_2PbI_4$	Lateral	8.12	1.5×10^{12}	–	4×10^2	460	30	[100]
$(OA)_2FA_{n-1}Pb_nBr_{3n+1}$	Lateral	32	–	0.25/1.45	–	442	9	[26]
$(PEA)_2MA_{n-1}Pb_nI_{3n+1}$	Lateral	0.25	8.6×10^{12}	–	–	500	5	[135]
$(PEA)_2SnI_4$	Lateral	16	1.9×10^{11}	630/3600	–	470	5	[57]
$(PEA)_2PbI_4$ single crystal	Lateral	98	1.6×10^{15}	0.06/0.05	–	460	4	[58]
$(PEA)_2MA_{n-1}Pb_nI_{3n+1}$ /$MAPbI_3$	Lateral	**149**	2×10^{12}	69/103	1×10^2	598	9	**This work**

Figure 3.13a shows the drain current vs. voltage ($I_{DS} - V_{DS}$) curves of the device with predefined *n*-value of 3 under illumination of different intensity at the wavelength of 598 nm, demonstrating a good ohmic contact between the perovskite film and the Au electrodes. **Figure 3.13b** presents the responsivity of the device as a function of applied voltage for different light intensity. The maximum R of 149 AW^{-1} can be obtained at the lowest illumination intensity of 38 nW cm^{-2} under a bias of 9 V, which is higher than most of the perovskite photodetectors shown in **Table 3.1**. In this case, the gain G of the device is estimated to be 270, according to the following equation [63, 87]

$$G = \frac{Rhc}{e\lambda} \tag{3.4}$$

where h is the Planck's constant, c is the speed of light, e is the elementary charge and λ is the wavelength of the incident light. The high gain can be attributed to the separation of electrons and holes by the cascade band structure in the gradient 2D/3D perovskite film, where photocarriers can circulate lots of times (equal to the gain) in the channel before recombining with opposite charges.

The device was also characterized under light with different wavelengths, including 420, 530, 685 and 760 nm. The responsivity as a function of light intensity for different wavelengths is summarized in **Figure 3.13c**, which can be fitted with the relationship $R \propto {E_e}^{\beta-1}$ (β is between 0.52 and 0.55) for all wavelengths. However, the device shows a little response to the infrared light at the wavelength of 860 nm beyond the absorption edge of the perovskite film. **Figure 3.13d** shows the responsivity of the device as a function of wavelength under the same illumination intensity of 10^{-2} mW cm^{-2}. Broadband photo response of the device can be observed and the maximum responsivity is obtained at around 685 nm.

3.4 Summary

In summary, 2D/3D perovskite films with phase separation are successfully prepared by a convenient hot-casting method. Vertical heterojunctions are formed in a single perovskite film from the bottom to the top. Highly sensitive photodetectors based on the 2D/3D perovskite films are realized for the first time. Due to the efficient charge separation in the heterojunctions, the devices show high sensitivity and fast response speed. Under optimum conditions, the device shows a high responsivity up to 10^2 AW^{-1}, a gain up to 10^2, a specific detectivity of 2×10^{12} Jones, and a response time of about 0.1 s. This work paves a way of realizing a type of highly sensitive photodetectors based on perovskite vertical heterojunctions in a single film.

Chapter 4 Highly Sensitive Near-Infrared Phototransistors Based on Low Bandgap Mixed Tin-Lead Iodide Perovskites

In this chapter, the high-performance phototransistors based on a single layer of mixed tin (Sn)-lead (Pb) perovskites were reported. Environment-friendly Sn-based perovskites with narrow energy bandgaps have attracted wide attention recently and been used as alternatives to their Pb-based counterparts. Here, the mixed Sn/Pb-based perovskite phototransistors have been presented, which exhibit ultrahigh responsivity of ~ 10^6 AW^{-1} and specific detectivity of ~ 10^{14} Jones in near-infrared (NIR) region. The high sensitivity of the devices might be mainly due to the long carrier lifetimes and strong light absorption in the perovskite alloys.

4.1 Introduction

NIR photodetectors are highly desirable for a multitude of industrial and scientific applications, such as optical tomography,[29] process monitoring,[30] and night vision.[31] Benefitting from merits including low photodamage, deep penetration and weak autofluorescence in living biosystems, NIR detection is also indispensable for medical instruments.[149-152] Notably, the distinct NIR-II (1000–1700 nm) detection is a proven method used in powerful real-time medical diagnosis, exhibiting the higher signal-to-background ratio (SBR) and deeper penetration depth compared to the visible and NIR-I (400–900 nm) fluorescence imaging systems.[32-37] The commercialized NIR photodetectors are mainly made from inorganic narrow-bandgap materials such as GaAs, PbSe, and InGaAs.[151, 153-156] However, these detectors usually rely on a thick material usage to achieve considerable photoresponse, which causes the obstacle

in achieving low-cost and flexible optoelectronic devices.[63] Organic–inorganic halide perovskite is currently considered one of the most promising candidates for next-generation light sensing due to their excellent optoelectronic properties and solution processability. [2-9, 157-159]

Perovskites have the general chemical formula of ABX_3, where A is an organic or inorganic cation, such as methylammonium (MA), formamidinium (FA), or cesium (Cs), B is typical lead (Pb), and X is a monovalent halide anion, such as chlorine (Cl), bromine (Br), iodine (I), or their mixtures. While high-performance photodetectors with perovskites as the semiconductors have been realized in many published works,[11, 21, 55, 160, 161] the response of typical perovskite-based devices is generally below than 800 nm. In contrast to those Pb-based perovskites, tin (Sn)-based perovskites present the low-energy absorption edge because of their small bandgaps (e.g., 1.4 eV for $FASnI_3$). With the help of high hole carrier mobility and photocarrier density of the p-doping $FASnI_3$, our previously reported photodetector has shown a high responsivity of 10^5 AW^{-1} at a low operating voltage of 0.5 V.[162] Nevertheless, the commercialization of Sn-based perovskites photodetectors remains hindered by the long recovery time of 1 minute and the lack of NIR-II photoresponse. Synthesis of a Sn/Pb-based perovskite alloy with a bandgap (e.g., $MA(Pb_{0.5}Sn_{0.5})I_3$ (1.17 eV)) lower than those of both end compounds (e.g., $MAPbI_3$ and MASnI3 (1.55 and 1.3 eV)) is potentially suitable for the high-performance NIR-II photodetectors. [163] In light of this, some works have been done on Sn-Pb perovskite photodetectors, yet satisfactory sensitivity and simple device structures are still lacking. For instance, based on $Cs(Pb_xSn_{1-x})(Br_yI_{1-y})_3$ nanowire synthesized with 0.5 mg mL^{-1} SnI_2 additive, Tang *et al.* demonstrated a broadband photodetector with the responsivity of only 0.085 AW^{-1}.[164] Cao *et al.* prepared another full inorganic PEDOT:PSS/$Cs(Pb_{0.5}Sn_{0.5})I_3$/PCBM

photodetector by adopting 5% $(PEA)_2Pb_{0.5}Sn_{0.5}I_4$, exhibiting the relatively high responsivity of 0.27 AW^{-1}.[165] Zhao *et al.* have further developed a double-sided passivation method dealing with the growth of the PEA-based 2D capping layers, whereas the responsivity of 0.53 AW^{-1} and specific detectivity of 2×10^{11} Jones were achieved in a photodetector composed of PTAA/PEAI/$Cs_{0.05}MA_{0.45}FA_{0.5}(Pb_{0.5}Sn_{0.5})I_3$ /PEAI/C_{60}/BCP.[166] Meanwhile, since Sn component of the mixed perovskites could be easily oxidized by O_2 and H_2O, the long-term stability is still a problem for these devices exposed in ambient conditions without protection.

Here, an ultrasensitive broadband phototransistors based on a single layer of low-bandgap $MA_{0.5}FA_{0.5}(Pb_{1-x}Sn_x)I_3$ will be reported. By introducing 4-hydrazinobenzoic acid (HBA) additive to suppress the oxidation of Sn^{2+} and assist the growth of perovskite grains, a series of air-stable Sn/Pb-based photodetectors with a simple device structure has been successfully prepared, which exhibits different recovery times from ~ 1 min to below 1 s (*x*-number is adjusted from 0.7 to 0.5). Although Sn/Pb-based perovskite alloys have been successful applied in solar cells [167-169] and even in photoconductors and photodiodes as mentioned above, they have never been used in phototransistors until now. The phototransistors based on $MA_{0.5}FA_{0.5}(Pb_{0.5}Sn_{0.5})I_3$ have exhibited responsivity up to 10^6 AW^{-1} and a specific detectivity of 2×10^{14} Jones in NIR-II region at a working voltage of 1 V. This work paves a way of realizing a type of highly sensitive broadband phototransistors based on low-bandgap Sn-containing perovskite alloys.

4.2 Experimental Section

4.2.1 Materials Synthesis

Different $FA_{0.5}MA_{0.5}$ $(Pb_{1-x}Sn_x)I_3$ precursor solutions were prepared by mixing methylammonium iodide (MAI), formamidinium iodide (FAI, Great cell Solar Ltd), lead iodide (PbI_2, Sigma-Aldrich), tin iodide (SnI_2) and tin fluorine (SnF_2, Alpha Aesar) (0.5 : 0.5 : 1-*x* : *x* : 0.1 *x*, molar ratio) in a dimethyl sulfoxide (DMSO, Sigma-Aldrich)/N,N-Dimethylformamide (DMF, Alfa Aesar) (1 : 4, volume ratio) mixture. 4-hydrazinobenzoic acid (HBA) was added as antioxidant, and the molar ratio of HBA and SnI_2 was 3%.

4.2.2 Device Fabrication

The Si/SiO_2 (300 nm) substrate was ultrasonically cleaned sequentially in deionized water, acetone, and isopropyl alcohol (IPA) and dried under a stream of nitrogen gas. Cr (10 nm)/Au (100 nm) electrodes with the channel width (W) and length (L) of 800 and 4 μm, respectively, were patterned via photolithography and magnetron sputtering on the Si/SiO_2 substrate. In the case of employing anti-solvent method during the perovskite thin film fabrication, prior to the spin-coating, the substrate was exposed to O_2 plasma for 5 min. After that, precursor solution was dropped on to the substrate followed by one-step spin-coating process at 5000 r.p.m. for 30 s, and diethyl ether was dropped on the film at 10^{th} s after starting the spin-coating process. Then, the devices were annealed at 60℃ for 1 min and 100 ℃ for 5 min. The thickness of the perovskite films can be controlled by adjusting the total Pb^{2+} molar concentration (from 1 to 1.5 $_M$) and the speed of spin coater (from 5000 to 3000 r.p.m.).

4.2.3 Materials Characterization

The composition and orientation of $FA_{0.5}MA_{0.5}$ $(Pb_{1-x}Sn_x)I_3$ perovskite layer was confirmed by X-ray Diffractometer (XRD) (Rigaku SmartLab). The Photoluminescence (PL) spectra of perovskite films were acquired by

photoluminescence spectrometer (Edinburgh: FLS920) with excitation wavelength of 488 nm. The absorption spectra of perovskite films were recorded by Perkin Elmer UV-vis-NIR spectrometer.

4.2.4 Electrical, Optoelectronic Measurements for the Devices

The photoresponse performance was reported using a semiconductor parameter analyzer (Keithley 4200-SCS, Solon, Ohio, USA) under light illumination at various intensity in the nitrogen-filled glovebox. The light sources were light-emitting diodes with wavelengths of 370, 420, 530, 598, 685, 860, 980, 1200, and 1450 nm.

4.3 Results and Discussion

4.3.1 Surface Morphology

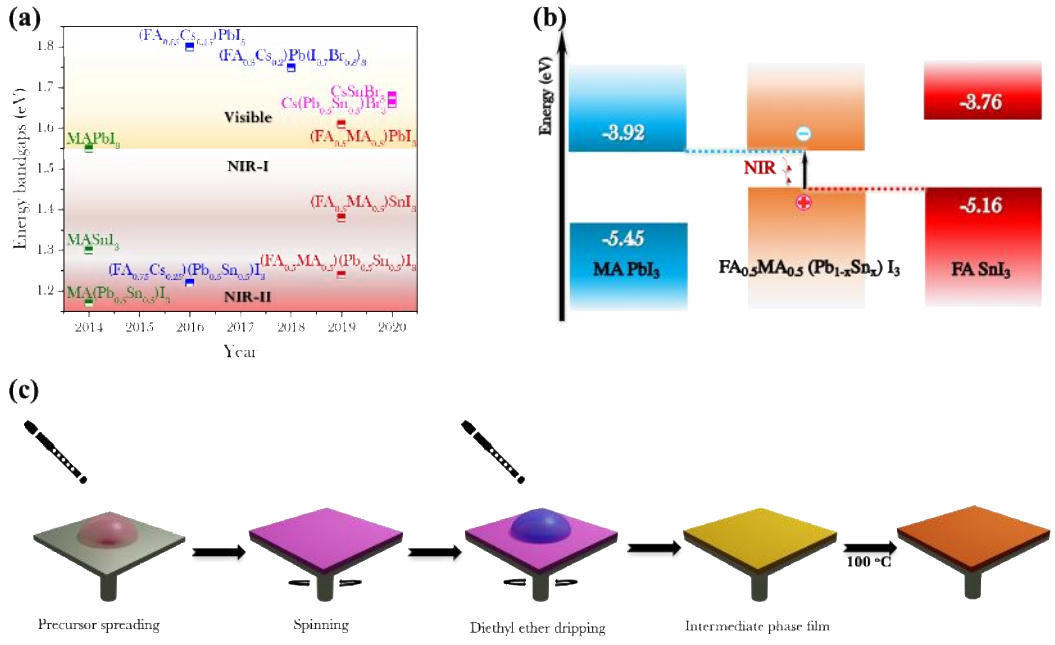

Figure 4.1 a) Relative bandgaps of organic, inorganic, and mixed perovskite alloys. **b)** Energy band diagram and c) anti-solvent crystallization strategy of $MA_{0.5}FA_{0.5}(Pb_{0.5}Sn_{0.5})I_3$ perovskite.

Recently, the introduction of Sn has been employed in several perovskite alloys to narrow their bandgaps below both end compounds (**Figure 4.1a**). [163, 170-173] This decline phenomenon of the bandgap was depicted in **Figure 4.1b**, which can be mainly due to the energy mismatch between Pb and Sn atomic orbitals in the perovskite layers. [74] To realize the uniform mixed Sn/Pb hybrid perovskite alloy $MA_{0.5}FA_{0.5}(Pb_{1-x}Sn_x)I_3$ films, an anti-solvent dropping process was developed as depicted in **Figure 4.1c**. For the initial step, 60 μL of $MA_{0.5}FA_{0.5}(Pb_{1-x}Sn_x)I_3$ precursor solution with HBA additive was dripped onto the center of the substrates followed by spin-coating. Before the perovskite layers dried (~ 10 s), 200 μL of diethyl ether was dripped on the spinning substrates to remove redundant solvent for assisting crystallization. Finally, compact and pinhole free perovskite films were obtained after annealing at 100 ℃ for 5 min.

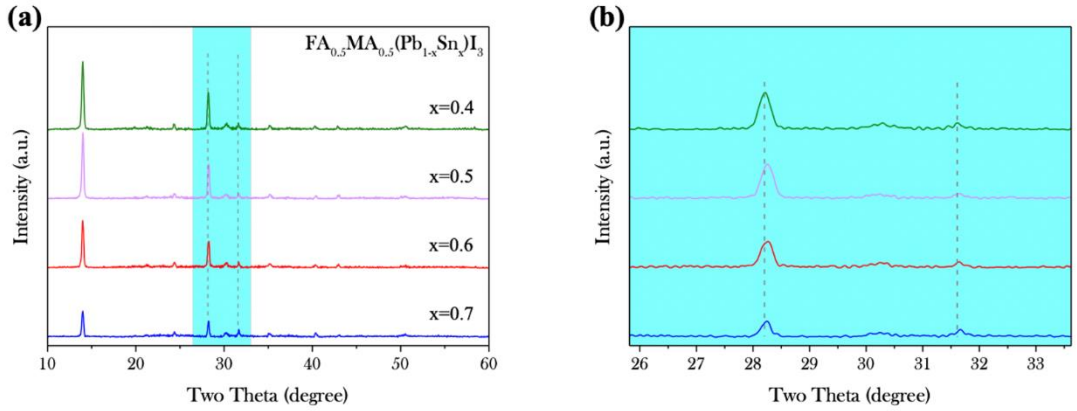

Figure 4.2 Characterization of the surface morphology based on varying stoichiometric ratios for $MA_{0.5}FA_{0.5}(Pb_{1-x}Sn_x)I_3$ perovskites, where x = 0.4, 0.5, 0.6, and 0.7. **a)** XRD spectra and **b)** the diagrams extracted from previous results.

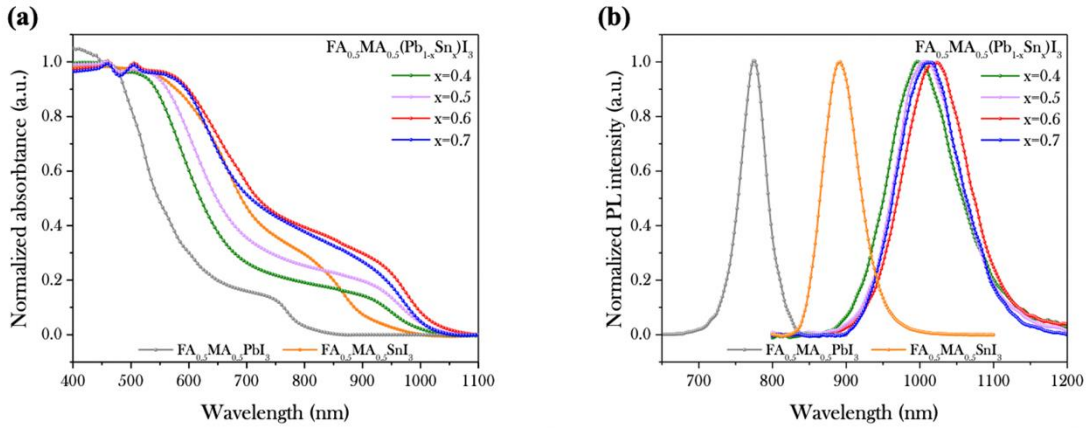

Figure 4.3 Characterization of the surface morphology based on varying stoichiometric ratios for $MA_{0.5}FA_{0.5}(Pb_{1-x}Sn_x)I_3$ perovskites, where x = 0, 0.4, 0.5, 0.6, 0.7 and 1. **a)** Normalized photoluminescence (PL) and **b)** absorption spectra.

To evaluate the crystal structure of the $MA_{0.5}FA_{0.5}(Pb_{1-x}Sn_x)I_3$ perovskite films, the X-ray diffraction (XRD) measurements were carried out on. The single peak of (113) plane located within the 2θ range between 22° and 25° suggests an orthorhombic crystal structure for Sn/Pb-based perovskite alloys (**Figure 4.2a**). [172] In addition, the intensity of diffraction peaks slightly decreases when *x*-number increases, indicating that film crystallinity could be reduced by the Sn incorporation in Sn/Pb-based perovskite alloys (**Figure 4.2b**).

The optical absorption spectra are shown in **Figure 4.3a**, which demonstrate the absorption tuning for the synthesized $MA_{0.5}FA_{0.5}(Pb_{1-x}Sn_x)I_3$ serial compounds. In contrast to the electronic absorption spectrum edges of 750 and 810 nm for pure Pb- and Sn-perovskites, the band edge positions of alloyed $MA_{0.5}FA_{0.5}(Pb_{1-x}Sn_x)I_3$ perovskites with *x*-numbers of 0.4, 0.5, 0.6, and 0.7 are close to 1000 nm. The result is mainly because of the decreased E_g by using Sn-derived VBM and Pb-derived CBM as mentioned above, indicating significant absorption of NIR photons for Sn/Pb-based perovskite alloys.

As the absorption spectra of $MA_{0.5}FA_{0.5}(Pb_{1-x}Sn_x)I_3$ show the softened band edge due to the existence of sub-bandgap states and increased scattering in the perovskite films, [174] steady photoluminescence (PL) spectroscopy is characterized to accurately reveal the E_g of the $MA_{0.5}FA_{0.5}(Pb_{1-x}Sn_x)I_3$ as shown in **Figure 4.3b**. The estimated E_g decreases from 1.60 to 1.21 eV (775 to 1022 nm) when the Sn content increases from 0% to 60% and shifts back to 1.39 eV (891 nm) for the pure $MA_{0.5}FA_{0.5}SnI_3$, which is in agreement with the absorption spectroscopy and even the results of $MA_xFA_{1-x}(Pb_xSn_{1-x})I_3$. [175]

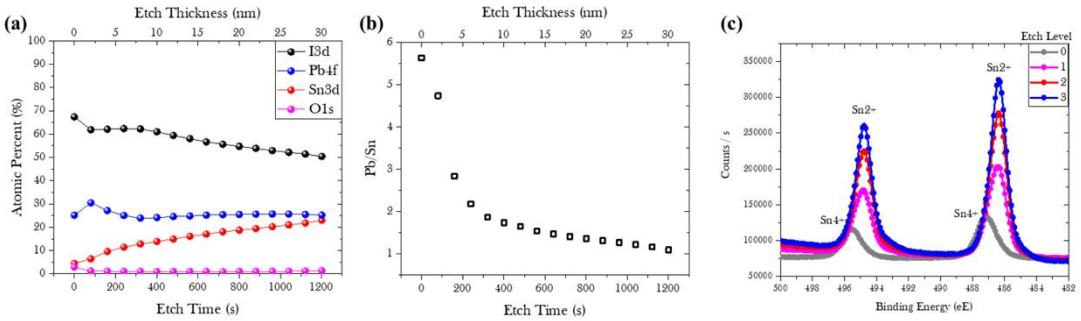

Figure 4.4. X-ray photoelectron spectroscopy (XPS) depth profile of $MA_{0.5}FA_{0.5}(Pb_{0.5}Sn_{0.5})I_3$ film. **a)** Atomic percent and **b)** Pb/Sn ratio from the XPS spectra as a function of depth from the top surface of Sn/Pb-based perovskite film. **c)** Band bending positions of Sn *3d* XPS peaks measured at the initial four XPS acquisitions.

To investigate the element distribution of Sn/Pb-based perovskite film, the depth-profiling X-ray photoelectron spectroscopy (XPS) was proceeded for the perovskite thin film on the indium tin oxide (ITO) substrate. By using argon (Ar) beam sputtering between successive XPS acquisitions, the profile clearly shows that $MA_{0.5}FA_{0.5}(Pb_{0.5}Sn_{0.5})I_3$ alloy has a Pb-rich perovskite capping layer (**Figure 4.4a**), which is consistent with other reports.[176, 177] Taking the evidence revealed by elemental XPS measurement of the surface of perovskite alloy (~30 nm) (**Figure 4.4b**),

it indicates that the vertical heterostructure of mixed Sn-Pb perovskite has been developed after an anti-solvent dropping process. Surprisingly, the reduction effect of Sn^{4+} content in the perovskite alloy has been also revealed through core level binding energy (Sn $3d_{5/2}$ and Sn $3d_{3/2}$ regions, respectively) measured by depth profiling. As **Figure 4.4c** presents, the peaks from Sn^{4+} oxidation state are clearly disappeared after sputtering. This phenomenon is consistent with the diminishing amounts of oxygen element measured in the top-surface XPS spectrum, suggesting additive of HBA and Pb-rich perovskite capping layer can effectively reduce the formed Sn^{4+} ions to enhance the film quality against oxidation. [169]

4.3.2 Mixed Sn/Pb-based Perovskite Phototransistors

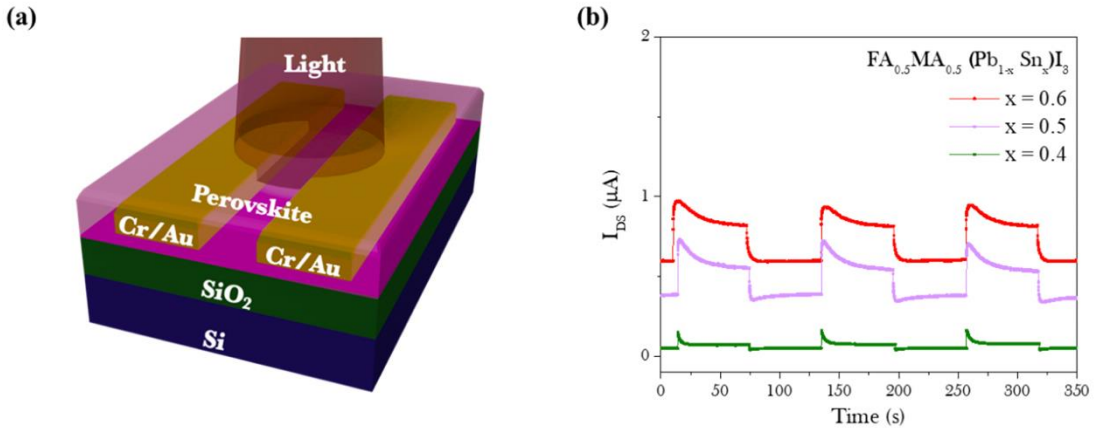

Figure 4.5 Design and performance of the devices based on varying stoichiometric ratios for $MA_{0.5}FA_{0.5}(Pb_{1-x}Sn_x)I_3$ perovskites, where x = 0.4, 0.5, and 0.6. **a)** The schematic illustration of perovskite photodetectors. **b)** Drain–source current versus time (I_{DS}–t) curves at the near-infrared wavelength of 980 nm (16.6 μW cm^{-2}). d) Temporal photocurrent responses highlighting for decay times.

Figure 4.5a presents a schematic diagram of photodetectors consisting of $MA_{0.5}FA_{0.5}(Pb_{1-x}Sn_x)I_3$ perovskite films with x-number varying from 0.4 to 0.7. Cr/Au

electrodes were deposited by magnetron sputtering on a Si/SiO_2 substrate and patterned by photolithography, followed by the anti-solvent dropping method of the perovskite channels. The drain current − time (I_{DS} – t) curves between the two Au electrodes of fabricated photodetectors were measured at the drain voltage (V_{DS}) of 1 V in the dark. Then, the perovskite photodetectors were characterized under near-infrared light (980 nm) with intensity of 16.6 μW cm^{-2}. The photocurrent (I_{Photo}) is defined by the following equation

$$I_{Photo} = I_{Light} - I_{Dark} \tag{4.1}$$

Figure 4.5b depicts that I_{Photo} of $MA_{0.5}FA_{0.5}(Pb_{1-x}Sn_x)I_3$ perovskite photodetector is enhanced by almost one order of magnitude from 0.05 to 0.3 μA with increasing *x*-number from 0.4 to 0.5. When *x*-number further increases from 0.5 to 0.6, the device exhibits the similar I_{Photo} (~ 0.3 μA) together with both increased I_{Light} and I_{Dark}.

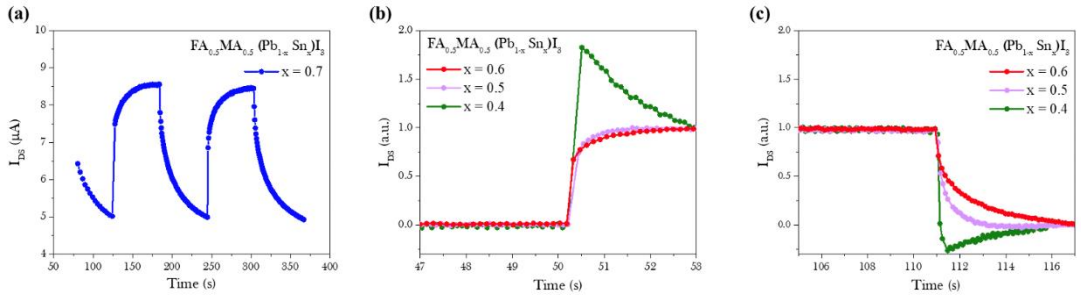

Figure 4.6 a) Drain–source current versus time (I_{DS}–t) curves at the near-infrared wavelength of 980 nm (16.6 μW cm^{-2}) for $MA_{0.5}FA_{0.5}(Pb_{1-x}Sn_x)I_3$ perovskites, where *x* = 0.7. Temporal photocurrent responses highlighting for **b)** rise and **c)** decay times for $MA_{0.5}FA_{0.5}(Pb_{1-x}Sn_x)I_3$ perovskites, where *x* = 0.4, 0.5, and 0.6.

The response time of a photodetector is a critical issue for its commercial application. Notably, the rise (τ_r) and decay (τ_d) times are generally defined in literature as the times for the current to rise from 10% to 90% of the peak value and vice versa, accordingly. The τ_r/τ_d of the perovskite photodetector based on $MA_{0.5}FA_{0.5}(Pb_{0.3}Sn_{0.7})I_3$ is determined to be larger than 30000/60000 ms (**Figure 4.6a**), which is similar to those of the Sn-based photodetectors and perovskite/organic-semiconductor phototransistors. [69, 148, 178]. The prolonged period of response time could greatly hinder its optoelectronic applications. A further decrease of τ_r/τ_d from 800/4000 to 500/1000 ms, together with almost the same I_{Photo}, were observed with decreasing *x*-number from 0.6 to 0.5 (**Figure 4.6b-c**), which suggests that $MA_{0.5}FA_{0.5}(Pb_{0.5}Sn_{0.5})I_3$ can be regarded as a promising candidate for photodetectors.

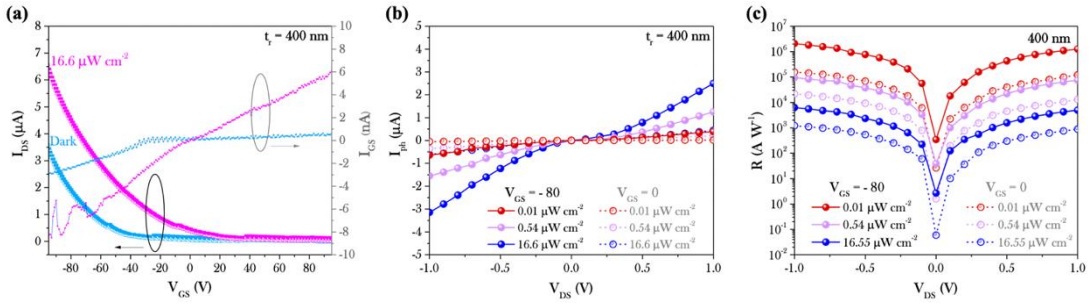

Figure 4.7 Photoresponse properties of the perovskite phototransistors based on $MA_{0.5}FA_{0.5}(Pb_{0.5}Sn_{0.5})I_3$. **a)** Plots of drain and gate currents through the perovskite film with thickness (t_r) of ~400 nm against gate bias at drain voltage of 1 V and at the near-infrared wavelength of 980 nm (16.6 μW cm^{-2}). Plots of **b)** photocurrent and **c)** responsivity of above device as functions of drain voltage under different illumination power of light with 980 nm wavelength.

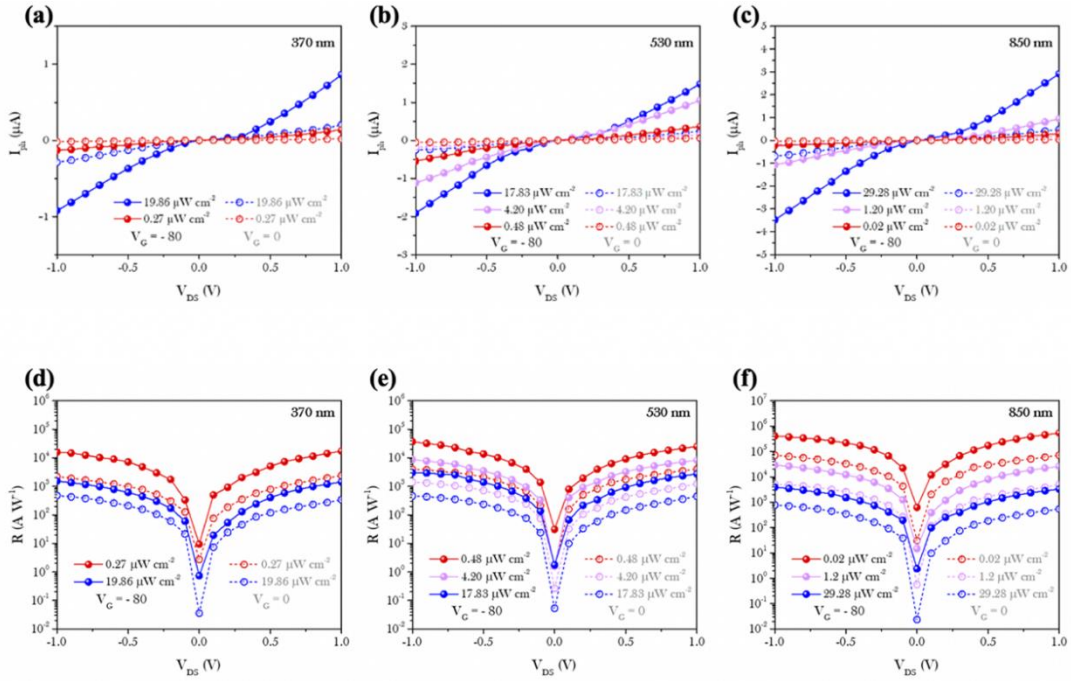

Figure 4.8 Plots of **a-c)** photocurrent and **d-f)** responsivity of above device as functions of drain voltage under different illumination power of light with 370, 530, and 850 nm wavelengths, respectively.

The effects of perovskite thickness (t_r) and gate voltage (V_{GS}) on device performance were then investigated. In addition to the above discussed 250 nm thick $MA_{0.5}FA_{0.5}(Pb_{0.5}Sn_{0.5})I_3$ perovskite photodetector, phototransistors with perovskite thickness of 400 and 550 nm were further prepared and characterized. **Figure 4.7a** shows the drain and gate currents versus gate voltage (I_{DS}–V_{GS} and I_{GS}–V_{GS}) curves of the 400 nm thick $MA_{0.5}FA_{0.5}(Pb_{0.5}Sn_{0.5})I_3$ perovskite phototransistor. The device was measured both in the dark and under near-infrared illumination with a wavelength of 980 nm (power density: 16.6 μW cm^{-2}) at the drain voltages (V_{DS}) of 1 V. Then, the phototransistor exhibited a negligible I_{GS} response to light illumination, which was three orders of magnitude lower than the I_{DS}. Therefore, the modulation of the channel current in a field effect transistor under a gate voltage is mainly due to the change of carrier concentration close to the gate dielectric (i.e., SiO_2). I_{Light} and I_{Dark} both increase

with the decrease of V_{GS}, suggesting that the perovskite layer close to the substrate is p channel under light illumination. Meanwhile, the threshold voltage shifted from –69 to –48 V with field effect mobility of ~ 0.04 $cm^2\ V^{-1}s^{-1}$. Notably, when the dark current decreased with increasing V_{GS} from -80 into 0 V, the light current also decreased to cause the lower responsivity.

Figure 4.7b presents the I_{Photo} of the device as a function of the operating voltage between the two Au electrodes for various light intensities (NIR wavelength: 980 nm) under V_{GS} of 0 and - 80 V, respectively. Moreover, the linear I_{Photo}–V_{DS} curves of the same device under UV (370 nm), visible (530 nm) and NIR-I (850 nm) light are shown in **Figure 4.8a-c,** demonstrating a good ohmic contact between the $MA_{0.5}FA_{0.5}(Pb_{0.5}Sn_{0.5})I_3$ perovskite film and the Au electrodes.

The responsivity (R) of a photodetector is given by [75]

$$R(AW^{-1}) = \frac{I_{ph}}{E_e WL} \tag{4.2}$$

Thus, the R is shown as a function of the operating voltage for various light intensities in **Figure 4.7c** and **Figure 4.8d-f**. The device exhibits a maximum R of ~ $2 \times 10^6\ AW^{-1}$ under V_{GS} of –80 V at the NIR wavelength, which is several orders of magnitude higher than those of reported Sn/Pb-based perovskite photodetectors. [164-166]

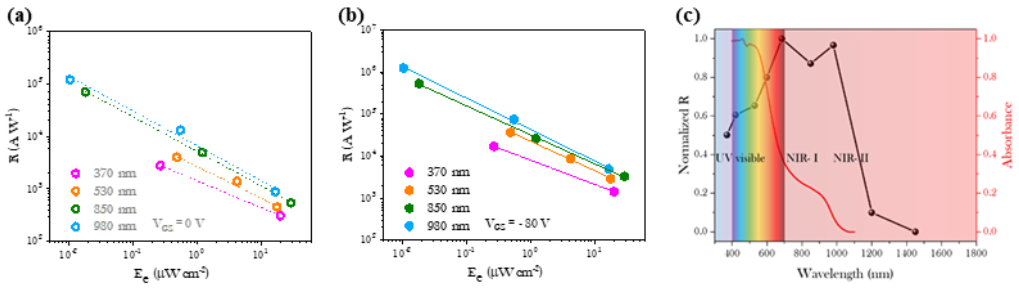

Figure 4.9 Plot of the responsivity as function of the light intensity with different wavelengths at V_{DG} of **a)** –80 and **b)** 0 V, respectively. **c)** Plot of responsivity as function of the wavelength under illumination.

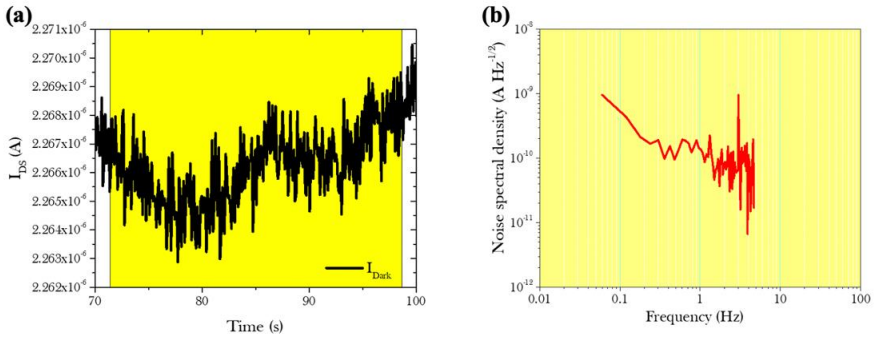

Figure 4.10 a) The noise of the dark current of the device. The operating voltage is 1 V. **b)** Analysis of noise spectral density of this perovskite phototransistor by the Fast Fourier Transform (FFT) from corresponding dark current noise.

The *R* of the devices increases with the decrease of light intensity, which follows a relationship given by $R \propto {E_e}^{\beta-1}$ and demonstrates an ultrahigh sensitivity for NIR response (**Figure 4.9a-b**). A spectral photoresponse from the UV to the NIR-II region of the perovskite phototransistor under V_{GS} of –80 V is further summarized in **Figure 4.9c**, suggesting that the device is preferably employed by both NIR-I and NIR-II detections. In this case, the gain (*G)* of this devices is estimated to be 2.5×10^6 under illumination with 980 nm, according to the following equation [87]

$$G = \frac{Rhc}{e\lambda} \tag{4.3}$$

In addition, *D** is the key parameter of a photodetector and given by [75, 87-89]

$$D^* = \frac{(AB)^{1/2}}{NEP} \tag{4.4}$$

$$NEP = \frac{\bar{i_n^2}^{1/2}}{R} \tag{4.5}$$

The noise level per unit bandwidth (1 Hz) of the device, which exhibited both the largest I_{ph} and R among all the devices, was measured to be ~ 10^{10} A $Hz^{-1/2}$ (**Figure 4.10)**. Therefore, D^* of the device at the wavelengths of 980 nm is calculated to be above 10^{14} Jones (cm $Hz^{1/2}$ W^{-1}).

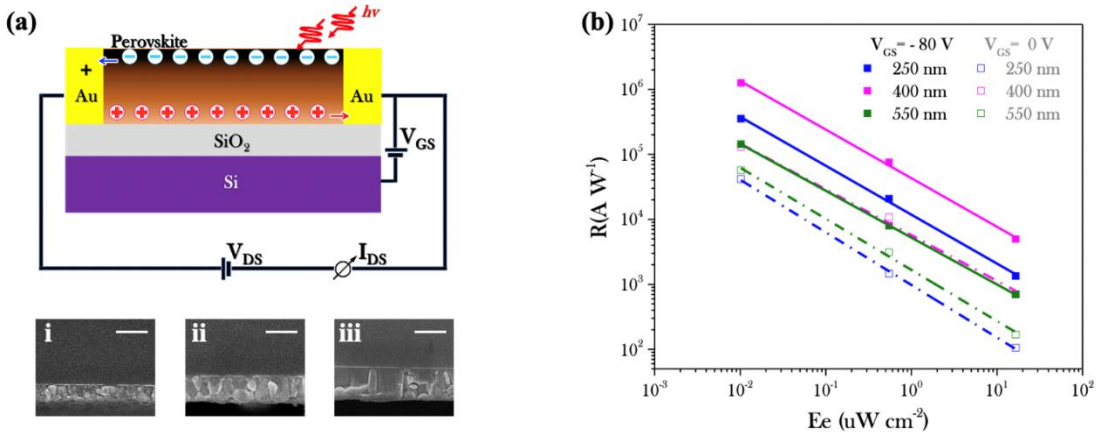

Figure 4.11 a) The device configuration of the perovskite phototransistors. The SEM images of the perovskite films with thickness of i) 250, ii) 400, and iii) 550 nm, where the scale bars are 500 nm. **b)** Plot of the responsivity as function of the light intensity under different wavelengths. The dotted lines in R-E_e curves are fitting curves with a formula of $R \propto E_e^{\beta-1}$.

In addition to above discussed 400 nm thick perovskite phototransistor, other devices with t_r of 250 and 550 nm have been further prepared and characterized (**Figure 4.11a**). As shown in **Figure 4.11b**, the responsivities as a function of light intensity can be fitted with the relationship $R \propto E_e^{\beta-1}$ at 980 nm wavelength and at V_{GS} = 0 and –80 V, respectively. It is noteworthy that carrier recombination might take place at the surface of the thickest perovskite film (550 nm) throughout negligible photogating effect, leading to the lowest I_{Photo} and R under V_{GS} of –80. In contrast, the enhanced performance of the device with t_r increasing from 250 to 400 nm is obtained, which can be attributed to the pronounced photogating effect and satisfactory light absorption.

4.4 Summary

In summary, this is the first time to realize highly sensitive broadband phototransistors based on mixed tin-lead perovskites. Under negative gate bias, a high density of photo-generated holes can accumulate in the bottom perovskite layer and induce a pronounced photogating effect on the channel. Based on the $MA_{0.5}FA_{0.5}(Pb_{0.5}Sn_{0.5})I_3$ perovskite film, the optimal device exhibits responsivity of 2×10^6 AW^{-1} and specific detectivity of up to 10^{14} Jones under NIR-II light at an operating voltage of only 1 V. This work reveals the feasibility of fabricating perovskite alloys in ultrasensitive phototransistors for broadband detection.

Chapter 5 **Conclusions and Future Prospect**

5.1 Conclusions

In recent years, the structural and compositional tunability of perovskite materials leads to the better understanding of foundational concept in optoelectronic applications. Furthermore, various types of halide perovskite materials have been developed, including the all-inorganic perovskites, the layered Ruddlesden-Popper perovskites, and the lead-free perovskites. As the results, the outstanding optoelectronic properties of these novel perovskite materials give us the chance to fabricate stable, broadband and low-cost devices. However, it is still challenging to attain high photosensitivity in pure perovskite-based photodetectors.

In this thesis, I have presented a convenient approach for fabrication of gradient 2D/3D perovskite heterojunctions through an enhanced hot-casting technique, which leads to a continuously change of the 2D perovskite compositions from $n = 1$ to ∞ along the vertical bottom-to-top direction of the films and forms vertical heterojunctions inside them. A series of perovskite thin films has been fabricated with varying predefined *n*-values of $(PEA)_2(MA)_{n-1}Pb_nI_{3n+1}$ precursor solution. At the optimal conditions, suitable 2D/3D perovskite vertical heterojunction can be created. By realizing the heterostructure-assisted charge separation in the photoactive layer, the device has showed a responsivity up to 10^2 AW-1, a gain up to 10^2 and a specific detectivity of 2×10^{12} Jones with the dynamic range from 0.01 to 100 μWcm^{-2}, which are higher than those of most 2D perovskite-based photodetectors.

Furthermore, Sn/Pb-based perovskite alloys have not been used as photo-absorbing layer in phototransistors until now. By introducing HBA additive in

precursor solutions to suppress the oxidation of Sn^{2+} and assist the growth of perovskite grains, a series of air-stable Sn/Pb-based PPDs with a simple device structure has been successfully prepared. They exhibit different recovery times from ~ 1 min to below 1 s (x-number is adjusted from $x = 0.7$ to 0.5 in $FA_{0.5}MA_{0.5}(Pb_{1-x}Sn_x)I_3$ precursor solutions), while the commercialization of Sn-based PPDs remain hindered by their long recovery time and the lack of NIR photoresponse. As a result, high responsivity of ~ 10^6 AW^{-1} and specific detectivity of ~ 10^{14} Jones have been further demonstrated in the NIR-II phototransistor based on $MA_{0.5}FA_{0.5}(Pb_{0.5}Sn_{0.5})I_3$, which are several orders of magnitude higher than those of reported Sn/Pb-based perovskite photodetectors.

5.2 Future Prospect

The photodetectors in this thesis were operated mainly based on either 2D layered perovskite or Sn/Pb-based perovskite alloy. Highly sensitive photodetectors have broad potential applications in the world, including environmental monitoring, imaging, optical communication, and biomedical sensing. As mention before, heterostructure-assisted charge separation can be obtained by introducing the gradient 2D/3D perovskite films with cascaded band structure in the devices, which paves a way for enhancing the performance of perovskite-based optoelectronic devices. Moreover, the Sn-based perovskite photodetectors generally have the relatively high responsivity but inferior response speed compared with the Pb-based perovskite devices. To alleviate the environmental problem caused by toxic Pb in the devices, compositional engineering of the perovskite active layers by completely or partially replacing Pb with Sn should be also further studied.

Together with ultrasensitive photodetection, I have studied the role of hot-casting method and the stoichiometric ratio control for developing perovskite thin films, which helps expedite the investigation of Pb-Sn-alloyed product with vertical heterojunctions. Next, I will systematically design and fabricate the high-performance phototransistors based on novel 2D/3D perovskite alloys. Considering the high carrier mobility of other 1D and 2D materials (e.g., carbon-nanotube and graphene), significant enhancement of the performance for perovskite phototransistors might be further achieved with an adequate synergetic effect. Thus, I will also try to prepare PPDs by using other materials as special conductive channels of the devices.

References

[1] A. Kojima, K. Teshima, Y. Shirai, and T. Miyasaka, "Organometal halide perovskites as visible-light sensitizers for photovoltaic cells," *J. Am. Chem. Soc.*, vol. 131, no. 17, pp. 6050-6051, 2009.

[2] V. Adinolfi, O. Ouellette, M. I. Saidaminov, G. Walters, A. L. Abdelhady, O. M. Bakr, and E. H. Sargent, "Fast and Sensitive Solution-Processed Visible-Blind Perovskite UV Photodetectors," *Adv. Mater.*, vol. 28, no. 33, pp. 7264-7268, 2016.

[3] S. Shrestha, R. Fischer, G. J. Matt, P. Feldner, T. Michel, A. Osvet, I. Levchuk, B. Merle, S. Golkar, H. W. Chen, S. F. Tedde, O. Schmidt, R. Hock, M. Ruhrig, M. Goken, W. Heiss, G. Anton, and C. J. Brabec, "High-performance direct conversion X-ray detectors based on sintered hybrid lead triiodide perovskite wafers," *Nat. Photonics*, vol. 11, no. 7, pp. 436-440, 2017.

[4] L. Shen, Y. J. Fang, D. Wang, Y. Bai, Y. H. Deng, M. M. Wang, Y. F. Lu, and J. S. Huang, "A Self-Powered, Sub-nanosecond-Response Solution-Processed Hybrid Perovskite Photodetector for Time-Resolved Photoluminescence-Lifetime Detection," *Adv. Mater.*, vol. 28, no. 48, pp. 10794-10800, 2016.

[5] I. Ka, L. F. Gerlein, R. Nechache, and S. G. Cloutier, "High-performance nanotube-enhanced perovskite photodetectors," *Sci. Rep.*, vol. 7, p. 45543, 2017.

[6] X. H. Wu, B. L. Zhou, J. C. Zhou, Y. T. Chen, Y. L. Chu, and J. Huang, "Distinguishable Detection of Ultraviolet, Visible, and Infrared Spectrum with High-Responsivity Perovskite-Based Flexible Photosensors," *Small*, vol. 14, no. 19, p. 1800527, 2018.

[7] Y. C. Kim, K. H. Kim, D. Y. Son, D. N. Jeong, J. Y. Seo, Y. S. Choi, I. T. Han, S. Y. Lee, and N. G. Park, "Printable organometallic perovskite enables large-area, low-dose X-ray imaging," *Nat.*, vol. 550, no. 7674, pp. 87-91, 2017.

[8] C.-K. Liu, Q. Tai, N. Wang, G. Tang, H.-L. Loi, and F. Yan, "Sn-Based Perovskite for Highly Sensitive Photodetectors," *Adv. Sci.*, p. 1900751, 2019.

[9] S. D. Stranks, G. E. Eperon, G. Grancini, C. Menelaou, M. J. P. Alcocer, T. Leijtens, L. M. Herz, A. Petrozza, and H. J. Snaith, "Electron-Hole Diffusion

Lengths Exceeding 1 Micrometer in an Organometal Trihalide Perovskite Absorber," *Sci.*, vol. 342, no. 6156, pp. 341-344, 2013.

[10] J. Burschka, N. Pellet, S. J. Moon, R. Humphry-Baker, P. Gao, M. K. Nazeeruddin, and M. Gratzel, "Sequential deposition as a route to high-performance perovskite-sensitized solar cells," *Nat.*, vol. 499, no. 7458, pp. 316-319, 2013.

[11] Y. Dong, Y. Zou, J. Song, X. Song, and H. Zeng, "Recent progress of metal halide perovskite photodetectors," *J. Mater. Chem. C*, vol. 5, no. 44, pp. 11369-11394, 2017.

[12] "Best Research-Cell Efficiency Chart." NREL. https://www.nrel.gov/pv/cell-efficiency.html (accessed August 2020).

[13] X. Hu, X. D. Zhang, L. Liang, J. Bao, S. Li, W. L. Yang, and Y. Xie, "High-Performance Flexible Broadband Photodetector Based on Organolead Halide Perovskite," *Adv. Funct. Mater.*, vol. 24, no. 46, pp. 7373-7380, 2014.

[14] Y. M. Sabri, A. E. Kandjani, S. J. Ippolito, and S. K. Bhargava, "Ordered Monolayer Gold Nano-urchin Structures and Their Size Induced Control for High Gas Sensing Performance," *Sci. Rep.*, vol. 6, p. 24625, 2016.

[15] T. Mueller, F. Xia, and P. Avouris, "Graphene photodetectors for high-speed optical communications," *Nat. Photonics*, vol. 4, p. 297, 2010.

[16] N. J. Huo, S. X. Yang, Z. M. Wei, S. S. Li, J. B. Xia, and J. B. Li, "Photoresponsive and Gas Sensing Field-Effect Transistors based on Multilayer WS2 Nanoflakes," *Sci. Rep.*, vol. 4, p. 5209, 2014.

[17] T. Rauch, M. Boberl, S. F. Tedde, J. Furst, M. V. Kovalenko, G. N. Hesser, U. Lemmer, W. Heiss, and O. Hayden, "Near-infrared imaging with quantum-dot-sensitized organic photodiodes," *Nat. Photonics*, vol. 3, no. 6, pp. 332-336, 2009.

[18] A. Rogalski, J. Antoszewski, and L. Faraone, "Third-generation infrared photodetector arrays," *J. Appl. Phys.*, vol. 105, no. 9, p. 091101, 2009.

[19] X. Gao, Y. Cui, R. M. Levenson, L. W. K. Chung, and S. Nie, "In vivo cancer targeting and imaging with semiconductor quantum dots," *Nat. Biotechnology*, vol. 22, p. 969, 2004.

[20] M. Buscema, J. O. Island, D. J. Groenendijk, S. I. Blanter, G. A. Steele, H. S. J. van der Zant, and A. Castellanos-Gomez, "Photocurrent generation with

two-dimensional van der Waals semiconductors," *Chem. Soc. Rev.*, vol. 44, no. 11, pp. 3691-3718, 2015.

[21] F. P. G. de Arquer, A. Armin, P. Meredith, and E. H. Sargent, "Solution-processed semiconductors for next-generation photodetectors," *Nature Reviews Materials*, vol. 2, no. 3, pp. 1-17, 2017.

[22] Y. L. Guo, C. Liu, H. Tanaka, and E. Nakamura, "Air-Stable and Solution-Processable Perovskite Photodetectors for Solar-Blind UV and Visible Light," *J. Phys. Chem. Lett.*, vol. 6, no. 3, pp. 535-539, 2015.

[23] T. Leijtens, G. E. Eperon, N. K. Noel, S. N. Habisreutinger, A. Petrozza, and H. J. Snaith, "Stability of Metal Halide Perovskite Solar Cells," *Adv. Energy Mater.*, vol. 5, no. 20, p. 1500963, 2015.

[24] Z. Wang, Z. J. Shi, T. T. Li, Y. H. Chen, and W. Huang, "Stability of Perovskite Solar Cells: A Prospective on the Substitution of the ACation and XAnion," *Angew. Chem. -Int. Ed.*, vol. 56, no. 5, pp. 1190-1212, 2017.

[25] R. K. Misra, B.-E. Cohen, L. Iagher, and L. Etgar, "Low-Dimensional Organic–Inorganic Halide Perovskite: Structure, Properties, and Applications," *ChemSusChem*, vol. 10, no. 19, pp. 3712-3721, 2017.

[26] D. J. Yu, F. Cao, Y. L. Shen, X. H. Liu, Y. Zhu, and H. B. Zeng, "Dimensionality and Interface Engineering of 2D Homologous Perovskites for Boosted Charge-Carrier Transport and Photodetection Performances," *J. Phys. Chem. Lett.*, vol. 8, no. 12, pp. 2565-2572, 2017.

[27] Z. Yuan, Y. Shu, Y. Xin, and B. W. Ma, "Highly luminescent nanoscale quasi-2D layered lead bromide perovskites with tunable emissions," *ChemComm*, vol. 52, no. 20, pp. 3887-3890, 2016.

[28] J. A. Sichert, Y. Tong, N. Mutz, M. Vollmer, S. Fischer, K. Z. Milowska, R. García Cortadella, B. Nickel, C. Cardenas-Daw, J. K. Stolarczyk, A. S. Urban, and J. Feldmann, "Quantum Size Effect in Organometal Halide Perovskite Nanoplatelets," *Nano Lett.*, vol. 15, no. 10, pp. 6521-6527, 2015.

[29] J. Schmitt, S. Xiang, and K. Yung, "Differential absorption imaging with optical coherence tomography," *JOSA A*, vol. 15, no. 9, pp. 2288-2296, 1998.

[30] J. B. Barton, R. F. Cannata, and S. M. Petronio, "InGaAs NIR focal plane arrays for imaging and DWDM applications," *Proc. SPIE* vol. 4721, pp. 37-47, 2002.

[31] J. Kallhammer, "The road ahead for car night-vision," *Nat. Photonics*, vol. 5, pp. 12-13, 2006.

[32] B. del Rosal, I. Villa, D. Jaque, and F. Sanz-Rodríguez, "In vivo autofluorescence in the biological windows: the role of pigmentation," *J. biophotonics*, vol. 9, no. 10, pp. 1059-1067, 2016.

[33] A. Zebibula, N. Alifu, L. Xia, C. Sun, X. Yu, D. Xue, L. Liu, G. Li, and J. Qian, "Ultrastable and biocompatible NIR-II quantum dots for functional bioimaging," *Adv. Funct. Mater.*, vol. 28, no. 9, p. 1703451, 2018.

[34] J. A. Carr, D. Franke, J. R. Caram, C. F. Perkinson, M. Saif, V. Askoxylakis, M. Datta, D. Fukumura, R. K. Jain, and M. G. Bawendi, "Shortwave infrared fluorescence imaging with the clinically approved near-infrared dye indocyanine green," *Proc. Natl. Acad. Sci. U.S.A.*, vol. 115, no. 17, pp. 4465-4470, 2018.

[35] F. Ding, Y. Zhan, X. Lu, and Y. Sun, "Recent advances in near-infrared II fluorophores for multifunctional biomedical imaging," *Chem. Sci.*, vol. 9, no. 19, pp. 4370-4380, 2018.

[36] S. Zhu, Z. Hu, R. Tian, B. C. Yung, Q. Yang, S. Zhao, D. O. Kiesewetter, G. Niu, H. Sun, and A. L. Antaris, "Repurposing cyanine NIR-I dyes accelerates clinical translation of near-infrared-II (NIR-II) bioimaging," *Adv. Mater.*, vol. 30, no. 34, p. 1802546, 2018.

[37] G. Hong, A. L. Antaris, and H. Dai, "Near-infrared fluorophores for biomedical imaging," *Nature Biomedical Engineering*, vol. 1, no. 1, pp. 1-22, 2017.

[38] Z. K. Tan, R. S. Moghaddam, M. L. Lai, P. Docampo, R. Higler, F. Deschler, M. Price, A. Sadhanala, L. M. Pazos, D. Credgington, F. Hanusch, T. Bein, H. J. Snaith, and R. H. Friend, "Bright light-emitting diodes based on organometal halide perovskite," *Nat Nanotechnol*, vol. 9, no. 9, pp. 687-92, 2014.

[39] N. Wang, L. Cheng, R. Ge, S. Zhang, Y. Miao, W. Zou, C. Yi, Y. Sun, Y. Cao, R. Yang, Y. Wei, Q. Guo, Y. Ke, M. Yu, Y. Jin, Y. Liu, Q. Ding, D. Di, L. Yang, G. Xing, H. Tian, C. Jin, F. Gao, R. H. Friend, J. Wang, and W. Huang, "Perovskite light-emitting diodes based on solution-processed self-organized multiple quantum wells," *Nat. Photonics*, vol. 10, no. 11, pp. 699-704, 2016.

[40] C. Xie and F. Yan, "Perovskite/Poly(3-hexylthiophene)/Graphene Multiheterojunction Phototransistors with Ultrahigh Gain in Broadband Wavelength Region," *ACS Appl. Mater. Interfaces*, vol. 9, no. 2, pp. 1569-1576, 2017.

[41] K. Hong, Q. Van Le, S. Y. Kim, and H. W. Jang, "Low-dimensional halide perovskites: review and issues," *J. Mater. Chem. C*, vol. 6, no. 9, pp. 2189-2209, 2018.

[42] B. Saparov and D. B. Mitzi, "Organic-Inorganic Perovskites: Structural Versatility for Functional Materials Design," *Chem Rev*, vol. 116, no. 7, pp. 4558-96, 2016.

[43] Z.-K. Tang, Z.-F. Xu, D.-Y. Zhang, S.-X. Hu, W.-M. Lau, and L.-M. Liu, "Enhanced optical absorption via cation doping hybrid lead iodine perovskites," *Scientific Reports*, vol. 7, no. 1, pp. 1-7, 2017.

[44] C. Zhou, Y. Tian, M. Wang, A. Rose, T. Besara, N. K. Doyle, Z. Yuan, J. C. Wang, R. Clark, and Y. Hu, "Low-dimensional organic tin bromide perovskites and their photoinduced structural transformation," *Angew. Chem. - Int. Ed.*, vol. 56, no. 31, pp. 9018-9022, 2017.

[45] J. Qian, Q. Guo, L. Liu, B. Xu, and W. Tian, "A theoretical study of hybrid lead iodide perovskite homologous semiconductors with 0D, 1D, 2D and 3D structures," *J. Mater. Chem. A*, vol. 5, no. 32, pp. 16786-16795, 2017.

[46] D. Cortecchia, H. A. Dewi, J. Yin, A. Bruno, S. Chen, T. Baikie, P. P. Boix, M. Gratzel, S. Mhaisalkar, C. Soci, and N. Mathews, "Lead-Free MA2CuCl(x)Br(4-x) Hybrid Perovskites," *Inorg Chem*, vol. 55, no. 3, pp. 1044-52, 2016.

[47] K. Zheng and T. Pullerits, "Two Dimensions Are Better for Perovskites," *J Phys Chem Lett*, vol. 10, no. 19, pp. 5881-5885, 2019.

[48] C. Tan, X. Cao, X. J. Wu, Q. He, J. Yang, X. Zhang, J. Chen, W. Zhao, S. Han, G. H. Nam, M. Sindoro, and H. Zhang, "Recent Advances in Ultrathin Two-Dimensional Nanomaterials," *Chem Rev*, vol. 117, no. 9, pp. 6225-6331, 2017.

[49] I. C. Smith, E. T. Hoke, D. Solis-Ibarra, M. D. McGehee, and H. I. Karunadasa, "A layered hybrid perovskite solar-cell absorber with enhanced moisture stability," *Angew. Chem. -Int. Ed.*, vol. 53, no. 42, pp. 11232-5, 2014.

[50] G. Niu, X. Guo, and L. Wang, "Review of recent progress in chemical stability of perovskite solar cells," *J. Mater. Chem. A*, vol. 3, no. 17, pp. 8970-8980, 2015.

[51] S. Ruddlesden and P. Popper, "New compounds of the K2NiF4 type," *Acta Crystallographica*, vol. 10, no. 8, pp. 538-539, 1957.

[52] X. Zhang, G. Wu, S. Yang, W. Fu, Z. Zhang, C. Chen, W. Liu, J. Yan, W. Yang, and H. Chen, "Vertically Oriented 2D Layered Perovskite Solar Cells with Enhanced Efficiency and Good Stability," *Small*, vol. 13, no. 33, p. 1700611, 2017.

[53] Z. Cheng and J. Lin, "Layered organic–inorganic hybrid perovskites: structure, optical properties, film preparation, patterning and templating engineering," *CrystEngComm*, vol. 12, no. 10, pp. 2646-2662, 2010.

[54] C. R. Kagan, D. B. Mitzi, and C. D. Dimitrakopoulos, "Organic-Inorganic Hybrid Materials as Semiconducting Channels in Thin-Film Field-Effect Transistors," *Sci.*, vol. 286, no. 5441, pp. 945-947, 1999.

[55] S. Chen and G. Shi, "Two-Dimensional Materials for Halide Perovskite-Based Optoelectronic Devices," *Adv. Mater.*, vol. 29, no. 24, p. 1605448, 2017.

[56] X. Hong, T. Ishihara, and A. V. Nurmikko, "Dielectric confinement effect on excitons in PbI4-based layered semiconductors," *Phys. Rev. B*, vol. 45, no. 12, pp. 6961-6964, 1992.

[57] L. Qian, Y. Sun, M. Wu, C. Li, D. Xie, L. Ding, and G. Shi, "A lead-free two-dimensional perovskite for a high-performance flexible photoconductor and a light-stimulated synaptic device," *Nanoscale*, vol. 10, no. 15, pp. 6837-6843, 2018.

[58] Y. Liu, Y. Zhang, Z. Yang, H. Ye, J. Feng, Z. Xu, X. Zhang, R. Munir, J. Liu, P. Zuo, Q. Li, M. Hu, L. Meng, K. Wang, D. M. Smilgies, G. Zhao, H. Xu, Z. Yang, A. Amassian, J. Li, K. Zhao, and S. F. Liu, "Multi-inch single-crystalline perovskite membrane for high-detectivity flexible photosensors," *Nat. Commun.*, vol. 9, no. 1, p. 5302, 2018.

[59] F. Li, C. Ma, H. Wang, W. Hu, W. Yu, A. D. Sheikh, and T. Wu, "Ambipolar solution-processed hybrid perovskite phototransistors," *Nat. Commun.*, vol. 6, p. 8238, 2015.

[60] M. Cao, Y. Zhang, Y. Yu, L. Jin, Y. Li, Z. Chen, Y. Che, H. Dai, G. Zhang, and J. Yao, "Enhanced perovskite phototransistor by multi-step slow annealing strategy," *Opt. Mater.*, vol. 84, pp. 498-503, 2018.

[61] N. Cho, F. Li, B. Turedi, L. Sinatra, S. P. Sarmah, M. R. Parida, M. I. Saidaminov, B. Murali, V. M. Burlakov, A. Goriely, O. F. Mohammed, T. Wu, and O. M. Bakr, "Pure crystal orientation and anisotropic charge transport in large-area hybrid perovskite films," *Nat. Commun.*, vol. 7, p. 13407, 2016.

[62] Y. Sun, C. Teng, D. Xie, L. Qian, and M. Sun, "Photomodulated Hysteresis Behaviors in Perovskite Phototransistors with Ultra-Low Operating Voltage," *J. Phys. Chem. C*, vol. 121, no. 21, pp. 11665-11671, 2017.

[63] C. Xie, C. K. Liu, H. L. Loi, and F. Yan, "Perovskite-Based Phototransistors and Hybrid Photodetectors," *Adv. Funct. Mater.*, vol. 30, no. 20, 2019.

[64] R. Quintero-Bermudez, A. Gold-Parker, A. H. Proppe, R. Munir, Z. Yang, S. O. Kelley, A. Amassian, M. F. Toney, and E. H. Sargent, "Compositional and orientational control in metal halide perovskites of reduced dimensionality," *Nat. Mater.*, vol. 17, no. 10, pp. 900-907, 2018.

[65] L. Pedesseau, D. Sapori, B. Traore, R. Robles, H.-H. Fang, M. A. Loi, H. Tsai, W. Nie, J.-C. Blancon, and A. Neukirch, "Advances and promises of layered halide hybrid perovskite semiconductors," *ACS Nano*, vol. 10, no. 11, pp. 9776-9786, 2016.

[66] J. Chen, Y. Wang, L. Gan, Y. He, H. Li, and T. Zhai, "Generalized Self-Doping Engineering towards Ultrathin and Large-Sized Two-Dimensional Homologous Perovskites," *Angew. Chem. -Int. Ed.*, vol. 56, no. 47, pp. 14893-14897, 2017.

[67] Y. Yan, Q. Wu, Y. Zhao, S. Chen, S. Hu, J. Zhu, J. Huang, and Z. Liang, "Air-Stable and Self-Driven Perovskite Photodiodes with High On/Off Ratio and Swift Photoresponse," *Small*, vol. 14, no. 41, p. e1802764, 2018.

[68] Y. Shao, Y. Liu, X. Chen, C. Chen, I. Sarpkaya, Z. Chen, Y. Fang, J. Kong, K. Watanabe, T. Taniguchi, A. Taylor, J. Huang, and F. Xia, "Stable Graphene-Two-Dimensional Multiphase Perovskite Heterostructure Phototransistors with High Gain," *Nano Lett.*, vol. 17, no. 12, pp. 7330-7338, 2017.

[69] C. Xie, P. You, Z. Liu, L. Li, and F. Yan, "Ultrasensitive broadband phototransistors based on perovskite/organic-semiconductor vertical heterojunctions," *Light Sci. Appl.*, Original Article vol. 6, p. e17023, 2017.

[70] J. Liang, P. Zhao, C. Wang, Y. Wang, Y. Hu, G. Zhu, L. Ma, J. Liu, and Z. Jin, "CsPb0.9Sn0.1IBr2 Based All-Inorganic Perovskite Solar Cells with Exceptional Efficiency and Stability," *J. Am. Chem. Soc.*, vol. 139, no. 40, pp. 14009-14012, 2017.

[71] Z. Xiao, Z. Song, and Y. Yan, "From Lead Halide Perovskites to Lead-Free Metal Halide Perovskites and Perovskite Derivatives," *Adv. Mater.*, vol. 31, no. 47, p. e1803792, 2019.

[72] P. Xu, S. Chen, H.-J. Xiang, X.-G. Gong, and S.-H. Wei, "Influence of defects and synthesis conditions on the photovoltaic performance of perovskite semiconductor CsSnI3," *Chem. Mater.*, vol. 26, no. 20, pp. 6068-6072, 2014.

[73] X. Xu, C.-C. Chueh, P. Jing, Z. Yang, X. Shi, T. Zhao, L. Y. Lin, and A. K. Y. Jen, "High-Performance Near-IR Photodetector Using Low-Bandgap MA0.5FA0.5Pb0.5Sn0.5I3 Perovskite," *Adv. Funct. Mater.*, vol. 27, no. 28, 2017.

[74] A. Goyal, S. McKechnie, D. Pashov, W. Tumas, M. van Schilfgaarde, and V. Stevanović, "Origin of Pronounced Nonlinear Band Gap Behavior in Lead–Tin Hybrid Perovskite Alloys," *Chem. Mater.*, vol. 30, no. 11, pp. 3920-3928, 2018.

[75] S. M. Sze and K. K. Ng, *Physics of semiconductor devices*. New York, US: John Wiley & Sons, 2006.

[76] C. Xie, C. Mak, X. Tao, and F. Yan, "Photodetectors Based on Two-Dimensional Layered Materials Beyond Graphene," *Adv. Funct. Mater.*, vol. 27, no. 19, 2017.

[77] G. Konstantatos and E. H. Sargent, "Nanostructured materials for photon detection," *Nat. Nanotechnol.*, Review Article vol. 5, p. 391, 2010.

[78] H. Fang and W. Hu, "Photogating in low dimensional photodetectors," *Adv. Sci.*, vol. 4, no. 12, p. 1700323, 2017.

[79] D. Kufer and G. Konstantatos, "Photo-FETs: phototransistors enabled by 2D and 0D nanomaterials," *ACS Photonics*, vol. 3, no. 12, pp. 2197-2210, 2016.

[80] R. Bistritzer and A. H. MacDonald, "Electronic cooling in graphene," *Phys. Rev. Lett.* , vol. 102, no. 20, p. 206410, 2009.

[81] X. Xu, N. M. Gabor, J. S. Alden, A. M. van der Zande, and P. L. McEuen, "Photo-thermoelectric effect at a graphene interface junction," *Nano lett.*, vol. 10, no. 2, pp. 562-566, 2010.

[82] J. C. Song, M. S. Rudner, C. M. Marcus, and L. S. Levitov, "Hot carrier transport and photocurrent response in graphene," *Nano lett.*, vol. 11, no. 11, pp. 4688-4692, 2011.

[83] X. Wang and X. Gan, "Graphene integrated photodetectors and opto-electronic devices—A review," *Chin. Phys. B*, vol. 26, no. 3, p. 034203, 2017.

[84] J. Yan, M. H. Kim, J. A. Elle, A. B. Sushkov, G. S. Jenkins, H. w. M. Milchberg, M. S. Fuhrer, and H. Drew, "Dual-gated bilayer graphene hot-electron bolometer," *Nat. Nanotechnol.*, vol. 7, no. 7, pp. 472-478, 2012.

[85] M. Dyakonov and M. Shur, "Shallow water analogy for a ballistic field effect transistor: New mechanism of plasma wave generation by dc current," *Phys. Rev. Lett.*, vol. 71, no. 15, p. 2465, 1993.

[86] Y. Liu, R. Cheng, L. Liao, H. Zhou, J. Bai, G. Liu, L. Liu, Y. Huang, and X. Duan, "Plasmon resonance enhanced multicolour photodetection by graphene," *Nat. Commun.*, vol. 2, no. 1, pp. 1-7, 2011.

[87] D. L. Shao, J. Gao, P. Chow, H. T. Sun, G. Q. Xin, P. Sharma, J. Lian, N. A. Koratkar, and S. Sawyer, "Organic-Inorganic Heterointerfaces for Ultrasensitive Detection of Ultraviolet Light," *Nano Lett.*, vol. 15, no. 6, pp. 3787-3792, 2015.

[88] X. Liu, L. L. Gu, Q. P. Zhang, J. Y. Wu, Y. Z. Long, and Z. Y. Fan, "All-printable band-edge modulated ZnO nanowire photodetectors with ultra-high detectivity," *Nat. Commun.*, vol. 5, p. 4007, 2014.

[89] C. O. Kim, S. Kim, D. H. Shin, S. S. Kang, J. M. Kim, C. W. Jang, S. S. Joo, J. S. Lee, J. H. Kim, and S.-H. Choi, "High photoresponsivity in an all-graphene p–n vertical junction photodetector," *Nat. Commun.*, vol. 5, p. 3249, 2014.

[90] F. Yan, Z. Wei, X. Wei, Q. Lv, W. Zhu, and K. Wang, "Toward High-Performance Photodetectors Based on 2D Materials: Strategy on Methods," *Small Methods*, vol. 2, no. 5, p. 1700349, 2018.

[91] J. E. Murphy, M. C. Beard, A. G. Norman, S. P. Ahrenkiel, J. C. Johnson, P. R. Yu, O. I. Micic, R. J. Ellingson, and A. J. Nozik, "PbTe colloidal nanocrystals: Synthesis, characterization, and multiple exciton generation," *J. Am. Chem. Soc.*, vol. 128, no. 10, pp. 3241-3247, 2006.

[92] R. X. Wang, L. C. Yang, Y. M. Zhang, S. J. Xu, K. Fu, B. S. Zhang, J. F. Wang, K. Xu, and H. Yang, "The effect of Ga-doped nanocrystalline ZnO

electrode on deep-ultraviolet enhanced GaN photodetector," *Appl. Phys. Lett.*, vol. 102, no. 21, p. 212104, 2013.

[93] W. E. Tennant, D. J. Gulbransen, A. Roll, M. Carmody, D. Edwall, A. Julius, P. Dreiske, A. Chen, W. McLevige, S. Freeman, D. Lee, D. E. Cooper, and E. Piquette, "Small-Pitch HgCdTe Photodetectors," *J. Electron. Mater.*, vol. 43, no. 8, pp. 3041-3046, 2014.

[94] P. R. A. Binetti, X. J. M. Leijtens, T. de Vries, Y. S. Oei, L. Di Cioccio, J. M. Fedeli, C. Lagahe, J. Van Campenhout, D. Van Thourhout, P. J. van Veldhoven, R. Notzel, and M. K. Smit, "InP/InGaAs Photodetector on SOI Photonic Circuitry," *IEEE Photonics J.*, vol. 2, no. 3, pp. 299-305, 2010.

[95] M. Grätzel, "The light and shade of perovskite solar cells," *Nat. Mater.*, vol. 13, no. 9, pp. 838-842, 2014.

[96] M. A. Green, A. Ho-Baillie, and H. J. Snaith, "The emergence of perovskite solar cells," *Nat. Photonics*, vol. 8, no. 7, pp. 506-514, 2014.

[97] S. Kazim, M. K. Nazeeruddin, M. Grätzel, and S. Ahmad, "Perovskite as light harvester: a game changer in photovoltaics," *Angew. Chem. -Int. Ed.*, vol. 53, no. 11, pp. 2812-2824, 2014.

[98] N.-G. Park, "Perovskite solar cells: an emerging photovoltaic technology," *Mater. Today*, vol. 18, no. 2, pp. 65-72, 2015.

[99] H. J. Snaith, "Perovskites: the emergence of a new era for low-cost, high-efficiency solar cells," *J. Phys. Chem. Lett.*, vol. 4, no. 21, pp. 3623-3630, 2013.

[100] B. Hwang and J. S. Lee, "2D Perovskite-Based Self-Aligned Lateral Heterostructure Photodetectors Utilizing Vapor Deposition," *Adv. Opt. Mater.*, vol. 7, no. 3, p. 1801356, 2018.

[101] J. Liu, J. Leng, K. Wu, J. Zhang, and S. Jin, "Observation of internal photoinduced electron and hole separation in hybrid two-dimentional perovskite films," *J. Am. Chem. Soc.*, vol. 139, no. 4, pp. 1432-1435, 2017.

[102] L. Li, N. Zhou, Q. Chen, Q. Shang, Q. Zhang, X. Wang, and H. Zhou, "Unraveling the Growth of Hierarchical Quasi-2D/3D Perovskite and Carrier Dynamics," *J. Phys. Chem. Lett.*, vol. 9, no. 5, pp. 1124-1132, 2018.

[103] G. Wang, D. Li, H.-C. Cheng, Y. Li, C.-Y. Chen, A. Yin, Z. Zhao, Z. Lin, H. Wu, and Q. He, "Wafer-scale growth of large arrays of perovskite microplate

crystals for functional electronics and optoelectronics," *Sci. Adv.*, vol. 1, no. 9, p. e1500613, 2015.

[104] J. Aizenberg, A. J. Black, and G. M. Whitesides, "Controlling local disorder in self-assembled monolayers by patterning the topography of their metallic supports," *Nat.*, vol. 394, no. 6696, pp. 868-871, 1998.

[105] J. Aizenberg, A. J. Black, and G. M. Whitesides, "Control of crystal nucleation by patterned self-assembled monolayers," *Nat.*, vol. 398, no. 6727, pp. 495-498, 1999.

[106] A. L. Briseno, S. C. Mannsfeld, M. M. Ling, S. Liu, R. J. Tseng, C. Reese, M. E. Roberts, Y. Yang, F. Wudl, and Z. Bao, "Patterning organic single-crystal transistor arrays," *Nat.*, vol. 444, no. 7121, pp. 913-917, 2006.

[107] B. He, W. Li, Q. Wang, L. Liang, H. Wang, J. Xu, S. Yang, Y. Jiang, Y. Tang, and B. Zou, "Ultrasensitive all-solution-processed field-effect transistor based perovskite photodetectors with sol-gel SiO2 as the dielectric layer," *J. Alloys Compd.*, vol. 717, pp. 150-155, 2017.

[108] M. Xiao, F. Huang, W. Huang, Y. Dkhissi, Y. Zhu, J. Etheridge, A. Gray-Weale, U. Bach, Y. B. Cheng, and L. Spiccia, "A fast deposition-crystallization procedure for highly efficient lead iodide perovskite thin-film solar cells," *Angew. Chem. -Int. Ed.*, vol. 53, no. 37, pp. 9898-9903, 2014.

[109] H.-B. Kim, H. Choi, J. Jeong, S. Kim, B. Walker, S. Song, and J. Y. Kim, "Mixed solvents for the optimization of morphology in solution-processed, inverted-type perovskite/fullerene hybrid solar cells," *Nanoscale*, vol. 6, no. 12, pp. 6679-6683, 2014.

[110] A. Mei, X. Li, L. Liu, Z. Ku, T. Liu, Y. Rong, M. Xu, M. Hu, J. Chen, and Y. Yang, "A hole-conductor–free, fully printable mesoscopic perovskite solar cell with high stability," *Sci.*, vol. 345, no. 6194, pp. 295-298, 2014.

[111] Q. Wang, Y. Shao, Q. Dong, Z. Xiao, Y. Yuan, and J. Huang, "Large fill-factor bilayer iodine perovskite solar cells fabricated by a low-temperature solution-process," *Energy & Environ. Sci.* , vol. 7, no. 7, pp. 2359-2365, 2014.

[112] F. X. Xie, D. Zhang, H. Su, X. Ren, K. S. Wong, M. Grätzel, and W. C. Choy, "Vacuum-assisted thermal annealing of CH3NH3PbI3 for highly stable and efficient perovskite solar cells," *ACS nano*, vol. 9, no. 1, pp. 639-646, 2015.

[113] A. Dualeh, N. Tétreault, T. Moehl, P. Gao, M. K. Nazeeruddin, and M. Grätzel, "Effect of annealing temperature on film morphology of organic–

inorganic hybrid pervoskite solid-state solar cells," *Adv. Funct. Mater.*, vol. 24, no. 21, pp. 3250-3258, 2014.

[114] H. Yu, F. Wang, F. Xie, W. Li, J. Chen, and N. Zhao, "The role of chlorine in the formation process of "CH3NH3PbI3-xClx" perovskite," *Adv. Funct. Mater.*, vol. 24, no. 45, pp. 7102-7108, 2014.

[115] S. P. Senanayak, B. Yang, T. H. Thomas, N. Giesbrecht, W. Huang, E. Gann, B. Nair, K. Goedel, S. Guha, and X. Moya, "Understanding charge transport in lead iodide perovskite thin-film field-effect transistors," *Sci. Adv.*, vol. 3, no. 1, p. e1601935, 2017.

[116] D. B. Mitzi, C. D. Dimitrakopoulos, J. Rosner, D. R. Medeiros, Z. Xu, and C. Noyan, "Hybrid Field-Effect Transistor Based on a Low-Temperature Melt-Processed Channel Layer," *Adv. Mater.*, vol. 14, no. 23, pp. 1772-1776, 2002.

[117] C. Chen, X. Zhang, G. Wu, H. Li, and H. Chen, "Visible-Light Ultrasensitive Solution-Prepared Layered Organic-Inorganic Hybrid Perovskite Field-Effect Transistor," *Adv. Opt. Mater.*, vol. 5, no. 2, 2017.

[118] H. Wang, Y. Chen, E. Lim, X. Wang, S. Yuan, X. Zhang, H. Lu, J. Wang, G. Wu, and T. Lin, "High-performance lead-free two-dimensional perovskite photo transistors assisted by ferroelectric dielectrics," *J. Mater. Chem. C*, vol. 6, no. 46, pp. 12714-12720, 2018.

[119] S. Dutta and K. Narayan, "Gate-Voltage Control of Optically-Induced Charges and Memory Effects in Polymer Field-Effect Transistors," *Adv. Mater.*, vol. 16, no. 23-24, pp. 2151-2155, 2004.

[120] K. H. Kim, S. Y. Bae, Y. S. Kim, J. A. Hur, M. H. Hoang, T. W. Lee, M. J. Cho, Y. Kim, M. Kim, and J. I. Jin, "Highly photosensitive J-aggregated single-crystalline organic transistors," *Adv. Mater.*, vol. 23, no. 27, pp. 3095-3099, 2011.

[121] C.-W. Tseng, D.-C. Huang, and Y.-T. Tao, "Electric bistability induced by incorporating self-assembled monolayers/aggregated clusters of azobenzene derivatives in pentacene-based thin-film transistors," *ACS Appl. Mater. Interfaces*, vol. 4, no. 10, pp. 5483-5491, 2012.

[122] C. S. Smithson, Y. Wu, T. Wigglesworth, and S. Zhu, "A More Than Six Orders of Magnitude UV-Responsive Organic Field-Effect Transistor Utilizing a Benzothiophene Semiconductor and Disperse Red 1 for Enhanced Charge Separation," *Adv. Mater.*, vol. 27, no. 2, pp. 228-233, 2015.

[123] F. Cao, W. Tian, M. Wang, and L. Li, "Polarized ferroelectric field-enhanced self-powered perovskite photodetector," *ACS Photonics*, vol. 5, no. 9, pp. 3731-3738, 2018.

[124] H. Huang, X. Wang, P. Wang, G. Wu, Y. Chen, C. Meng, L. Liao, J. Wang, W. Hu, and H. Shen, "Ferroelectric polymer tuned two dimensional layered MoTe 2 photodetector," *RSC Adv.*, vol. 6, no. 90, pp. 87416-87421, 2016.

[125] X. Wang, P. Wang, J. Wang, W. Hu, X. Zhou, N. Guo, H. Huang, S. Sun, H. Shen, T. Lin, M. Tang, L. Liao, A. Jiang, J. Sun, X. Meng, X. Chen, W. Lu, and J. Chu, "Ultrasensitive and Broadband MoS(2) Photodetector Driven by Ferroelectrics," *Adv. Mater.*, vol. 27, no. 42, pp. 6575-81, 2015.

[126] J. Van Hove, R. Hickman, J. Klaassen, P. Chow, and P. Ruden, "Ultraviolet-sensitive, visible-blind GaN photodiodes fabricated by molecular beam epitaxy," *Appl. Phys. Lett.*, vol. 70, no. 17, pp. 2282-2284, 1997.

[127] A. M. Streltsov, K. Moll, A. L. Gaeta, P. Kung, D. Walker, and M. Razeghi, "Pulse autocorrelation measurements based on two-and three-photon conductivity in a GaN photodiode," *Appl. Phys. Lett.*, vol. 75, no. 24, pp. 3778-3780, 1999.

[128] Y. Chen, Y. Sun, J. Peng, J. Tang, K. Zheng, and Z. Liang, "2D Ruddlesden-Popper Perovskites for Optoelectronics," *Adv. Mater.*, vol. 30, no. 2, p. 1703487, 2018.

[129] J. Zhou, Y. Chu, and J. Huang, "Photodetectors Based on Two-Dimensional Layer-Structured Hybrid Lead Iodide Perovskite Semiconductors," *ACS Appl. Mater. Interfaces*, vol. 8, no. 39, pp. 25660-25666, 2016.

[130] R. Dong, C. Lan, X. Xu, X. Liang, X. Hu, D. Li, Z. Zhou, L. Shu, S. Yip, C. Li, S. W. Tsang, and J. C. Ho, "Novel Series of Quasi-2D Ruddlesden-Popper Perovskites Based on Short-Chained Spacer Cation for Enhanced Photodetection," *ACS Appl. Mater. Interfaces*, vol. 10, no. 22, pp. 19019-19026, 2018.

[131] H.-L. Loi, J. Cao, X. Guo, C.-K. Liu, N. Wang, J. Song, G. Tang, Y. Zhu, and F. Yan, "Gradient 2D/3D Perovskite Films Prepared by Hot-Casting for Sensitive Photodetectors," *Adv. Sci.*, vol. 7, no. 14, p. 2000776, 2020.

[132] S. Wei, F. Wang, X. Zou, L. Wang, C. Liu, X. Liu, W. Hu, Z. Fan, J. C. Ho, and L. Liao, "Flexible Quasi-2D Perovskite/IGZO Phototransistors for

Ultrasensitive and Broadband Photodetection," *Adv. Mater.*, vol. 32, no. 6, p. e1907527, 2020.

[133] Z. Song, S. C. Watthage, A. B. Phillips, B. L. Tompkins, R. J. Ellingson, and M. J. Heben, "Impact of Processing Temperature and Composition on the Formation of Methylammonium Lead Iodide Perovskites," *Chem. Mater.*, vol. 27, no. 13, pp. 4612-4619, 2015.

[134] M. Yuan, L. N. Quan, R. Comin, G. Walters, R. Sabatini, O. Voznyy, S. Hoogland, Y. Zhao, E. M. Beauregard, P. Kanjanaboos, Z. Lu, D. H. Kim, and E. H. Sargent, "Perovskite energy funnels for efficient light-emitting diodes," *Nat. Nanotechnol.*, vol. 11, no. 10, pp. 872-877, 2016.

[135] W. Peng, J. Yin, K. T. Ho, O. Ouellette, M. De Bastiani, B. Murali, O. El Tall, C. Shen, X. Miao, J. Pan, E. Alarousu, J. H. He, B. S. Ooi, O. F. Mohammed, E. Sargent, and O. M. Bakr, "Ultralow Self-Doping in Two-dimensional Hybrid Perovskite Single Crystals," *Nano Lett.*, vol. 17, no. 8, pp. 4759-4767, 2017.

[136] D. H. Cao, C. C. Stoumpos, O. K. Farha, J. T. Hupp, and M. G. Kanatzidis, "2D Homologous Perovskites as Light-Absorbing Materials for Solar Cell Applications," *J. Am. Chem. Soc.*, vol. 137, no. 24, pp. 7843-50, 2015.

[137] Q. Shang, Y. Wang, Y. Zhong, Y. Mi, L. Qin, Y. Zhao, X. Qiu, X. Liu, and Q. Zhang, "Unveiling Structurally Engineered Carrier Dynamics in Hybrid Quasi-Two-Dimensional Perovskite Thin Films toward Controllable Emission," *J. Phys. Chem. Lett.*, vol. 8, no. 18, pp. 4431-4438, 2017.

[138] J. Qing, X.-K. Liu, M. Li, F. Liu, Z. Yuan, E. Tiukalova, Z. Yan, M. Duchamp, S. Chen, Y. Wang, S. Bai, J.-M. Liu, H. J. Snaith, C.-S. Lee, T. C. Sum, and F. Gao, "Aligned and Graded Type-II Ruddlesden-Popper Perovskite Films for Efficient Solar Cells," *Adv. Energy Mater.*, vol. 8, no. 21, p. 1800185, 2018.

[139] Y. Lin, Y. Fang, J. Zhao, Y. Shao, S. J. Stuard, M. M. Nahid, H. Ade, Q. Wang, J. E. Shield, N. Zhou, A. M. Moran, and J. Huang, "Unveiling the operation mechanism of layered perovskite solar cells," *Nat. Commun.*, vol. 10, no. 1, p. 1008, 2019.

[140] S. Chen, X. Zhang, J. Zhao, Y. Zhang, G. Kong, Q. Li, N. Li, Y. Yu, N. Xu, J. Zhang, K. Liu, Q. Zhao, J. Cao, J. Feng, X. Li, J. Qi, D. Yu, J. Li, and P. Gao, "Atomic scale insights into structure instability and decomposition pathway of

methylammonium lead iodide perovskite," *Nat. Commun.*, vol. 9, no. 1, p. 4807, 2018.

[141] M. U. Rothmann, W. Li, Y. Zhu, A. Liu, Z. Ku, U. Bach, J. Etheridge, and Y. B. Cheng, "Structural and Chemical Changes to CH3 NH3 PbI3 Induced by Electron and Gallium Ion Beams," *Adv. Mater.*, vol. 30, no. 25, p. e1800629, 2018.

[142] M. Nastasi, N. Michael, J. Mayer, J. K. Hirvonen, and M. James, *Ion-solid interactions: fundamentals and applications*. Cambridge, UK: Cambridge University Press, 1996.

[143] L. A. Giannuzzi, *Introduction to focused ion beams: instrumentation, theory, techniques and practice*. New York, US: Springer Science & Business Media, 2004.

[144] N. Klein-Kedem, D. Cahen, and G. Hodes, "Effects of light and electron beam irradiation on halide perovskites and their solar cells," *Acc. Chem. Res.*, vol. 49, no. 2, pp. 347-354, 2016.

[145] L. N. Quan, Y. Zhao, F. P. Garcia de Arquer, R. Sabatini, G. Walters, O. Voznyy, R. Comin, Y. Li, J. Z. Fan, H. Tan, J. Pan, M. Yuan, O. M. Bakr, Z. Lu, D. H. Kim, and E. H. Sargent, "Tailoring the Energy Landscape in Quasi-2D Halide Perovskites Enables Efficient Green-Light Emission," *Nano Lett.*, vol. 17, no. 6, pp. 3701-3709, 2017.

[146] T. Zhang, M. Long, M. Qin, X. Lu, S. Chen, F. Xie, L. Gong, J. Chen, M. Chu, and Q. Miao, "Stable and efficient 3D-2D perovskite-perovskite planar heterojunction solar cell without organic hole transport layer," *Joule*, vol. 2, no. 12, pp. 2706-2721, 2018.

[147] Z. Sun, Z. Liu, J. Li, G.-a. Tai, S.-P. Lau, and F. Yan, "Infrared Photodetectors Based on CVD-Grown Graphene and PbS Quantum Dots with Ultrahigh Responsivity," *Adv. Mater.*, vol. 24, no. 43, pp. 5878-5883, 2012.

[148] C. Xie and F. Yan, "Enhanced performance of perovskite/organic-semiconductor hybrid heterojunction photodetectors with the electron trapping effects," *J. Mater. Chem. C*, vol. 6, no. 6, pp. 1338-1342, 2018.

[149] W.-F. Cheong, S. A. Prahl, and A. J. Welch, "A review of the optical properties of biological tissues," *IEEE J. Quantum Electron.*, vol. 26, no. 12, pp. 2166-2185, 1990.

[150] K. Welsher, S. P. Sherlock, and H. Dai, "Deep-tissue anatomical imaging of mice using carbon nanotube fluorophores in the second near-infrared window," *Proc. Natl. Acad. Sci. U.S.A.*, vol. 108, no. 22, pp. 8943-8948, 2011.

[151] M. Garcia, C. Edmiston, T. York, R. Marinov, S. Mondal, N. Zhu, G. P. Sudlow, W. J. Akers, J. Margenthaler, and S. Achilefu, "Bio-inspired imager improves sensitivity in near-infrared fluorescence image-guided surgery," *Optica*, vol. 5, no. 4, pp. 413-422, 2018.

[152] H.-W. Liu, X.-X. Hu, K. Li, Y. Liu, Q. Rong, L. Zhu, L. Yuan, F.-L. Qu, X.-B. Zhang, and W. Tan, "A mitochondrial-targeted prodrug for NIR imaging guided and synergetic NIR photodynamic-chemo cancer therapy," *Chem. Sci.*, vol. 8, no. 11, pp. 7689-7695, 2017.

[153] R. Yousefi, M. Mahmoudian, A. Sa´aedic, M. Cheraghizaded, F. Jamali-Sheinie, and M. Azarangf, "Effect of annealing temperature and graphene concentrations on photovoltaic and NIR-detector applications of PbS/rGO nanocomposites," *Ceram. Int.*, vol. 42, p. 15209, 2016.

[154] G. Wu, R. Fu, J. Chen, W. Yang, J. Ren, X. Guo, Z. Ni, X. Pi, C. Z. Li, and H. Li, "Perovskite/Organic Bulk-Heterojunction Integrated Ultrasensitive Broadband Photodetectors with High Near-Infrared External Quantum Efficiency over 70%," *Small*, vol. 14, no. 39, p. 1802349, 2018.

[155] K. H. Hendriks, W. Li, M. M. Wienk, and R. A. Janssen, "Small-bandgap semiconducting polymers with high near-infrared photoresponse," *J. Am. Chem. Soc.*, vol. 136, no. 34, pp. 12130-12136, 2014.

[156] Z. Zheng, L. Gan, J. Zhang, F. Zhuge, and T. Zhai, "An enhanced UV–Vis–NIR an d flexible photodetector based on electrospun ZnO nanowire array/PbS quantum dots film heterostructure," *Adv. Sci.*, vol. 4, no. 3, p. 1600316, 2017.

[157] Y. Hu, J. Schlipf, M. Wussler, M. L. Petrus, W. Jaegermann, T. Bein, P. Muller-Buschbaum, and P. Docampo, "Hybrid Perovskite/Perovskite Heterojunction Solar Cells," *ACS Nano*, vol. 10, no. 6, pp. 5999-6007, 2016.

[158] Q. Dong, Y. Fang, Y. Shao, P. Mulligan, J. Qiu, L. Cao, and J. Huang, "Electron-hole diffusion lengths> 175 μm in solution-grown CH3NH3PbI3 single crystals," *Sci.*, vol. 347, no. 6225, pp. 967-970, 2015.

[159] C. Wehrenfennig, G. E. Eperon, M. B. Johnston, H. J. Snaith, and L. M. Herz, "High charge carrier mobilities and lifetimes in organolead trihalide perovskites," *Adv. Mater.*, vol. 26, no. 10, pp. 1584-1589, 2014.

[160] M. Ahmadi, T. Wu, and B. Hu, "A Review on Organic-Inorganic Halide Perovskite Photodetectors: Device Engineering and Fundamental Physics," *Adv. Mater.*, vol. 29, no. 41, 2017.

[161] W. Tian, H. Zhou, and L. Li, "Hybrid Organic-Inorganic Perovskite Photodetectors," *Small*, vol. 13, no. 41, 2017.

[162] C. K. Liu, Q. Tai, N. Wang, G. Tang, H. L. Loi, and F. Yan, "Sn-Based Perovskite for Highly Sensitive Photodetectors," *Adv. Sci.*, vol. 6, no. 17, p. 1900751, 2019.

[163] F. Hao, C. C. Stoumpos, R. P. Chang, and M. G. Kanatzidis, "Anomalous band gap behavior in mixed Sn and Pb perovskites enables broadening of absorption spectrum in solar cells," *J. Am. Chem. Soc.*, vol. 136, no. 22, pp. 8094-9, 2014.

[164] X. Tang, H. Zhou, X. Pan, R. Liu, D. Wu, and H. Wang, "All-Inorganic Halide Perovskite Alloy Nanowire Network Photodetectors with High Performance," *ACS Appl. Mater. Interfaces*, vol. 12, no. 4, pp. 4843-4848, 2020.

[165] F. Cao, J. Chen, D. Yu, S. Wang, X. Xu, J. Liu, Z. Han, B. Huang, Y. Gu, K. L. Choy, and H. Zeng, "Bionic Detectors Based on Low-Bandgap Inorganic Perovskite for Selective NIR-I Photon Detection and Imaging," *Adv. Mater.*, vol. 32, no. 6, p. e1905362, 2020.

[166] Y. Zhao, C. Li, J. Jiang, B. Wang, and L. Shen, "Sensitive and Stable Tin-Lead Hybrid Perovskite Photodetectors Enabled by Double-Sided Surface Passivation for Infrared Upconversion Detection," *Small*, p. e2001534, 2020.

[167] Z. Yang, A. Rajagopal, C. C. Chueh, S. B. Jo, B. Liu, T. Zhao, and A. K. Jen, "Stable Low-Bandgap Pb-Sn Binary Perovskites for Tandem Solar Cells," *Adv. Mater.*, vol. 28, no. 40, pp. 8990-8997, 2016.

[168] D. Zhao, Y. Yu, C. Wang, W. Liao, N. Shrestha, C. R. Grice, A. J. Cimaroli, L. Guan, R. J. Ellingson, K. Zhu, X. Zhao, R.-G. Xiong, and Y. Yan, "Low-bandgap mixed tin–lead iodide perovskite absorbers with long carrier lifetimes for all-perovskite tandem solar cells," *Nat. Energy*, vol. 2, no. 4, 2017.

[169] Z. Zhu, N. Li, D. Zhao, L. Wang, and A. K. Y. Jen, "Improved Efficiency and Stability of Pb/Sn Binary Perovskite Solar Cells Fabricated by Galvanic Displacement Reaction," *Adv. Energy Mater.*, vol. 9, no. 7, 2019.

[170] G. E. Eperon, T. Leijtens, K. A. Bush, R. Prasanna, T. Green, J. T.-W. Wang, D. P. McMeekin, G. Volonakis, R. L. Milot, and R. May, "Perovskite-perovskite tandem photovoltaics with optimized band gaps," *Sci.*, vol. 354, no. 6314, pp. 861-865, 2016.

[171] D. Zhao, C. Wang, Z. Song, Y. Yu, C. Chen, X. Zhao, K. Zhu, and Y. Yan, "Four-Terminal All-Perovskite Tandem Solar Cells Achieving Power Conversion Efficiencies Exceeding 23%," *ACS Energy Lett.*, vol. 3, no. 2, pp. 305-306, 2018.

[172] L. Zeng, Z. Chen, S. Qiu, J. Hu, C. Li, X. Liu, G. Liang, C. J. Brabec, Y. Mai, and F. Guo, "2D-3D heterostructure enables scalable coating of efficient low-bandgap Sn–Pb mixed perovskite solar cells," *Nano Energy*, vol. 66, 2019.

[173] Y. Xian, Y. Zhang, N. U. Rahman, H. Yin, Y. Long, P. Liu, W. Li, and J. Fan, "An Emerging All-Inorganic CsSnxPb1–xBr3 (0 ≤ x ≤ 1) Perovskite Single Crystal: Insight on Structural Phase Transition and Electronic Properties," *J. Phys. Chem. C*, vol. 124, no. 24, pp. 13434-13446, 2020.

[174] H.-J. Feng, T. R. Paudel, E. Y. Tsymbal, and X. C. Zeng, "Tunable Optical Properties and Charge Separation in CH3NH3Sn x Pb1–x I3/TiO2-Based Planar Perovskites Cells," *J. Am. Chem. Soc.*, vol. 137, no. 25, pp. 8227-8236, 2015.

[175] W. Liao, D. Zhao, Y. Yu, N. Shrestha, K. Ghimire, C. R. Grice, C. Wang, Y. Xiao, A. J. Cimaroli, R. J. Ellingson, N. J. Podraza, K. Zhu, R. G. Xiong, and Y. Yan, "Fabrication of Efficient Low-Bandgap Perovskite Solar Cells by Combining Formamidinium Tin Iodide with Methylammonium Lead Iodide," *J. Am. Chem. Soc.*, vol. 138, no. 38, pp. 12360-3, 2016.

[176] R. P. Frankenthal and D. J. Siconolfi, "AES study of tin–lead alloys: Effects of ion sputtering and oxidation on surface composition and structure," *J. Vac. Sci. Technol.*, vol. 17, no. 6, pp. 1315-1319, 1980.

[177] G. C. Nelson and J. A. Borders, "Surface composition of a tin–lead alloy," *J. Vac. Sci. Technol.*, vol. 20, no. 4, pp. 939-942, 1982.

[178] K. Liu, Y. Jiang, Y. Jiang, Y. Guo, Y. Liu, and E. Nakamura, "Chemical Formation and Multiple Applications of Organic-Inorganic Hybrid Perovskite Materials," *J. Am. Chem. Soc.*, vol. 141, no. 4, pp. 1406-1414, 2019.